Spectral fiber-photometry derives hemoglobin concentration changes for accurate measurement of fluorescent sensor activity

Wei-Ting Zhang[1-3+], Tzu-Hao Harry Chao[1-3+], Yue Yang[1-4], Tzu-Wen Wang[1,2], Sung-Ho Lee[1-3], Esteban A. Oyarzabal[1-3], Jingheng Zhou[5], Randy Nonneman[1-3], Nicolas C. Pegard[6,7], Hongtu Zhu[2,4,8], Guohong Cui[5*], Yen-Yu Ian Shih[1-3,7*]

[1]Center for Animal MRI, University of North Carolina at Chapel Hill

[2]Biomedical Research Imaging Center, University of North Carolina at Chapel Hill

[3]Department of Neurology, University of North Carolina at Chapel Hill

[4]Department of Biostatistics, University of North Carolina at Chapel Hill

[5]In vivo Neurobiology Group, Neurobiology Laboratory, National Institute of Environmental Health Sciences, National Institutes of Health

[6]Department of Applied Physical Sciences, UNC Neuroscience Center, University of North Carolina at Chapel Hill

[7]Department of Biomedical Engineering, University of North Carolina at Chapel Hill

[8]Department of Computer Science, University of North Carolina at Chapel Hill

[+]These authors contributed equally

[*]Correspondence to Yen-Yu Ian Shih, Ph.D. (shihy@unc.edu) or Guohong Cui, M.D., Ph.D. (cuig@mail.nih.gov)

Highlights

- Hemoglobin-absorption compromises fiber-photometry recording *in vivo*
- Spectral photometry allows quantification of hemoglobin concentration changes for correction
- The proposed platform allows measuring regional differences in neurovascular transfer function

Summary

Fiber-photometry is an emerging technique for recording fluorescent sensor activity in the brain. However, significant hemoglobin-absorption artifacts in fiber-photometry data may be misinterpreted as sensor activity changes. Because hemoglobin exists in nearly every location in the brain and its concentration varies over time, such artifacts could impede the accuracy of many photometry recording results. Here we present a novel use of spectral photometry technique and propose computational methods to quantify photon absorption effects by using activity-independent fluorescence signals, which can be used to derive oxy- and deoxy-hemoglobin concentration changes. Following time-locked neuronal activation *in vivo*, we observed that a 20% increase in CBV contributes to about a 4% decrease in green fluorescence signal and a 2% decrease in red fluorescence signal. While these hemoglobin concentration changes are often temporally delayed than the fast-responding fluorescence spikes, we found that erroneous interpretation may occur when examining pharmacology-induced sustained activity changes, and in some cases, hemoglobin-absorption could flip the GCaMP signal polarity. We provided hemoglobin-based correction methods to restore fluorescence signals across spectra and compare our results against the commonly used regression approach. We also demonstrated the utility of spectral fiber-photometry for delineating brain regional differences in hemodynamic response functions.

Keywords

Spectral fiber-photometry, fluorescence, hemoglobin-absorption, excitation, emission, photon traveling pathlengths, hemodynamic response function, genetically encoded calcium indicators, isosbestic, green fluorescent sensor, red-shifted fluorescent sensor, post-stimulus undershoot

Introduction

Fiber-photometry relies on an implanted optical fiber to excite and detect fluorescence signals, and is best known for its ability to measure ensemble neuronal or neurochemical activity in small volumes of brain tissue in animal models. The simplicity and cost-effectiveness of the optical system make the technique highly accessible (Meng et al., 2018), and lightweight, miniature fiber optics make photometry compatible with a wide variety of experimental settings, such as freely moving behavioral assessment (Kim et al., 2016; Meng et al., 2018) or head-fixed brain-wide imaging (Chen et al., 2019; Pais-Roldán et al., 2020) (**Figure 1A**). Several genetically encoded fluorescent sensors of cellular activity and neurotransmitters have recently become widely available (Chen et al., 2013; Dana et al., 2016; Marvin et al., 2019, 2013; Patriarchi et al., 2018; Sun et al., 2018; Tian et al., 2009; H. Wang et al., 2018), expanding the range of applications for fiber-photometry. The tunable spectral specificity has further enabled new parallel sensing capabilities with wavelength multiplexing. Given its rapidly increasing usage in neuroscience (Cui et al., 2013; Luchsinger et al., 2021; Pisano et al., 2019; Sych et al., 2019), understanding the inherent confounding factors in fiber-photometry data is of paramount significance.

One of the most notable confounders affecting fluorescence measurements is light absorption by hemoglobin (Hb) within blood vessels (Ma et al., 2016; Prahl, 1999). The Hb-absorption artifact has been studied and addressed extensively in wide-field imaging with reflective or backscattered lights (Ma et al., 2016; Valley et al., 2020) and recently in two-photon lifetime microscopy (2PLM) measuring the partial pressure of O_2 (Mächler et al., 2021). The Hb-absorption artifact should be present in most photometry data because the intervascular distance of capillaries is known to be < 60 μm in nearly every location in the brain (Smith et al., 2019) and commonly used photometry targeted volumes is 10^5–10^6 μm^3 (Pisanello et al., 2019). This absorption occurs in two phases: along the excitation path, by

absorbing photons that travel from the fiber tip to the targeted fluorescent proteins; and along the emission path, by absorbing photons emitted by the fluorescent proteins as they travel back towards the optical fiber (**Figure 1B**). Both absorption effects add up and result in a substantial photon count reduction. Importantly, Hb-absorption is non-linear, wavelength-dependent, and varies as a function of dynamic oxy- and deoxy-hemoglobin (HbO and HbR) concentration changes *in vivo* (ΔC_{HbO} and ΔC_{HbR}) (Meng and Alayash, 2017; Prahl, 1999) (**Figure S1**, derived from(Prahl, 1999)), causing erroneous photometry reading. Further, because the power spectra of hemodynamic signals overlap significantly with most commonly used fluorescent sensors (**Figure S2**), hemoglobin related artifacts cannot be removed from fiber-photometry data by notch filtering or regressing either cerebral blood flow or cerebral blood volume (CBV) signals. To the best of our knowledge, the influence of Hb-absorption on fiber-photometry-derived fluorescent sensor activity has never been studied. The ability to quantify Hb concentration fluctuations in photometry data would not only enable more accurate fluorescent sensor activity measurements, but would also provide concurrent hemodynamic metrics, which is the foundation of several brain-mapping techniques including functional magnetic resonance imaging (fMRI) (Schulz et al., 2012), intrinsic optics (Hillman, 2007), and functional ultrasound (Rungta et al., 2017).

<Insert Figure 1, Figure S1, S2 here>

In this study, we propose a novel use of spectrally resolved fiber-photometry platform and computational methods that can independently derive HbO and HbR concentration changes from activity-independent fluorescent reporter signals. We present the use of this technique to remove the Hb-absorption artifacts from calcium activity recording and demonstrate the added benefit to compute transfer function between neuronal and vascular activity which is crucial for interpreting hemodynamic-based neuroimaging data such as fMRI, functional ultrasound, and intrinsic optics.

Results

Theoretical Hb-absorption effect on photometry recordings

We solved the following equation using the generalized method of moments (GMM) (Hansen, 1982) with spectrometer outputs, which provides quantifiable photon counts across spectra:

$$\frac{F(t,\lambda_{Em})}{F(t_0,\lambda_{Em})} = e^{-[\Delta\mu_a(t,\lambda_{Ex})X(\lambda_{Ex})+\Delta\mu_a(t,\lambda_{Em})X(\lambda_{Em})]} \cdot \frac{C(t)}{C(t_0)} \quad (1)$$

where $\Delta\mu_a(t,\lambda_{Ex})$ and $\Delta\mu_a(t,\lambda_{Em})$ represent the absorption coefficient changes at excitation wavelength λ_{Ex} and emission wavelength λ_{Em}, respectively, at time point t as compared to a reference time point t_0. Both $\Delta\mu_a(t,\lambda_{Ex})$ and $\Delta\mu_a(t,\lambda_{Em})$ are affected by ΔC_{HbO} and ΔC_{HbR} (see Method Equation 16). $X(\lambda_{Ex})$ and $X(\lambda_{Em})$ represent the photon traveling pathlengths (see Methods for details) at the excitation and emission wavelengths, respectively. To solve equation (1), we first performed a Monte Carlo simulation using the pipeline shown in **Figure S3** to obtain $X(\lambda_{Ex})$ and $X(\lambda_{Em})$. We determined the average photon traveling pathlengths for emission wavelengths from 488 nm to 700 nm in the simulated brain tissue from a total of 29 simulations (2-2.5 $\times 10^4$ photons each) in **Figure 1C**, with detailed numbers tabulated in **Table S1**. These results are expected to be generalizable and can be used across labs. As an example, we illustrated spatial probability and luminance-distance profiles for the commonly used 488 nm excitation, 515 nm emission and 580 nm emission in **Figure S4A-C** (see also **Supplementary Video 1**). These results allowed calculating the simulated effects of Hb-absorption on fluorescence signal measurement, for which we observed significant nonlinear, wavelength-dependent effects (**Figure 1D**).

<Insert Figure S3, S4 here>

Ex vivo quantification of Hb-absorption effects on photometry recordings

We first performed *ex vivo* measurements and showed that adding 1 mL of fresh, venous mouse blood into a 10 mL mixture of Alexa 488 and 568 fluorescent dye solution significantly reduced both fluorescence signals measured by fiber-photometry. Compared to adding the blood, adding 1 mL vehicle (0.9% saline) induced significantly less reduction in both Alexa 488 and 568 signals (**Figure S5A, C**). Subsequently, we saturated the mixture with 100% oxygen to increase the HbO-HbR ratio and observed

marked increases in the Alexa 568 signals but decreases in Alexa 488 signals. We did not observe significant signal changes when infusing the oxygen into the solution added with 1 mL saline (**Figure S5B, D**).

<Insert Figure 1, Figure S5 here>

In vivo quantification of Hb-absorption effects on photometry recordings

We performed an *in vivo* experiment to measure the Hb-absorption of activity-independent fluorescence signals in fiber-photometry. We selected a commonly used fluorophore, enhanced yellow fluorescent protein (EYFP), whose fluorescence signal is activity-independent and has an emission spectrum peaking at 526 nm. We virally expressed EYFP using adeno-associated virus (AAV) in the primary somatosensory cortex (S1) of the forelimb region (S1FL) under the calmodulin kinase IIα (CaMKIIα) promoter and then implanted an optical fiber into this target area (**Figure 2A, B**). On the day of photometry recording, we intravenously administered Rhodamine B, a long-circulating red fluorescent dye, to enable steady-state CBV measurements (Unekawa et al., 2015) (**Figure 2C**) and cross validate our proposed method in calculating total Hb concentration changes. Of note, the resulting EYFP and Rhodamine B spectra overlapped significantly with the Hb-absorption spectra (see **Figure S2**), suggesting a significant impact of Hb-absorption on the data from these fluorescence signals. Upon electrical stimulation of the contralateral forepaw (9 Hz, 3 mA, 0.5 ms pulse width for 10 s), we observed robust positive Rhodamine-derived CBV (rhoCBV) changes as expected (**Figure 2D**). Intriguingly, the EYFP signal concurrently recorded from the same fiber showed robust negative changes (**Figure 2E**), which indicated significant Hb-absorption of the EYFP signal *in vivo*. Although the pH-dependent effect on the EYFP signal cannot be completely excluded, a previous study showed that in pH 6.5-9, where typical pH homeostasis of a hippocampal neuron (~7.03-7.46) is located (Ruffin et al., 2014), EYFP excited by 470 nm was not significantly affected by the pH changes (Nakabayashi et al., 2012). Using well-documented molar extinction coefficients (**Figure S1**), photon-traveling pathlengths derived from a Monte Carlo

simulation (**Figure 1C**), and spectral fiber-photometry datapoints across 502 – 544 nm wavelengths over time (see equation (17-21) in **Methods**), we derived $\Delta C_{HbO}(t)$ and $\Delta C_{HbR}(t)$ using GMM. Notably, this is feasible and robust because we have access to a range of spectral datapoints for every single time point and therefore could use numerous empirical data to solve two unknowns (ΔC_{HbO} and ΔC_{HbR}, see also **Figure S6** for the effect of input spectral datapoints). The derived concentration changes (**Figure 2F, G**) were within physiological ranges and comparable to those reported in the literature (Ma et al., 2016), and the summation of the two (i.e., total Hb concentration changes, termed as $\Delta C_{HbT}(t)$) informs CBV changes (Ma et al., 2016) (**Figure 2J**). The calculated $\Delta C_{HbT}(t)$ highly resembled the rhoCBV changes measured from a distinct and less-affected red spectrum (**Figure S7**). With $\Delta C_{HbO}(t)$ and $\Delta C_{HbR}(t)$ obtained, we then calculated $\Delta\mu_a(t,\lambda_{Ex})$ and $\Delta\mu_a(t,\lambda_{Em})$, and input these parameters into equation (1) to correct the rhoCBV changes (**Figure 2H**) and EYFP signals (**Figure 2I**). Indeed, **Figure 2I** shows a flattened EYFP trace following the proposed correction, demonstrating the validity of our approach. Although the influence of Hb-absorption on EYFP signal varied by trials, our proposed method accurately corrected EYFP signals in all trials (**Figure 2K**). Notably, despite the smaller influence on the rhoCBV signal measured from the red spectrum, the absorption effect remained statistically significant (**Figure 2L**). In addition to the fluorescence signal changes induced by forepaw sensory stimulations, we also replicated these findings using a 5% CO_2 hypercapnic challenge paradigm and successfully restored the contaminated EYFP signal changes (**Figure S8**).

<Insert Figure 2, Figure S6, S7, S8 here>

Impact of Hb-absorption on acute GCaMP signal measurement using fiber-photometry.

We virally expressed the GCaMP6f (hereafter as GCaMP), one of the most widely used genetically encoded calcium indicators (Chen et al., 2013), using AAV under the CaMKIIα promoter in the S1FL. We also expressed tandem dimer tomato (tdTomato), an activity-independent red fluorescent protein, under the CAG promoter (**Figure 3A, B**) and then implanted an optical fiber into this target area.

Our rationale for choosing tdTomato was similar to that for EYFP in **Figure 2**, as it does not encode activity changes and thus its photon counts can be used to derive ΔC_{HbO} and ΔC_{HbR} for GCaMP signal correction. Using different promoters for GCaMP and tdTomato doesn't affect the application of our method in that tdTomato serves as "background light" which is irrelevant to the neuronal changes but is generally affected by the vascular changes no matter which promoter was chosen. Unlike in the experiment described in **Figure 2**, Rhodamine B could no longer be used for CBV cross-validation because the red spectrum was occupied by tdTomato (**Figure 3C**). Instead, we performed this GCaMP-tdTomato experiment inside a magnetic resonance imaging (MRI) scanner where CBV changes could be measured by intravenously administering an iron oxide contrast agent, Feraheme[23] (**Figure 3D**). This allowed CBV to be validated using an established and completely independent modality. After a short, 1 s electrical stimulation of the contralateral forepaw (9 Hz, 3 mA, 0.5 ms pulse width), we observed a rapid increase in GCaMP signal followed by an undershoot (**Figure 3E, Q**). Such undershoot is absent in cultured neurons where Hb is not present and rarely observed in two-photon imaging data where neurons and blood vessels are mostly segregated in space (Chen et al., 2013; Mittmann et al., 2011). The tdTomato signal decreased significantly upon forepaw stimulation and showed a much longer delay in its kinetics, but has its peak temporally matched to that of the GCaMP undershoot (**Figure 3F**). Using the methods similar to that described in **Figure 2**, but with spectral photometry datapoints across 575-699 nm wavelengths over time, we derived $\Delta C_{HbO}\ (t)$ and $\Delta C_{HbR}\ (t)$ (**Figure 3G, H**). Interestingly, the derived ΔC_{HbR} data exhibited a rapid initial increase (**Figure 3H**) before a more prolonged reduction – a phenomenon well-documented in the optical literature(Devor et al., 2003) and termed "initial dip" in blood-oxygenation-level-dependent fMRI(Hu and Yacoub, 2012). This initial increase in HbR was not detectable in the raw tdTomato data, indicating that our method is capable of deriving parameters with temporal kinetics distinct from the detected raw fluorescence activity. **Figure 3J** shows the corrected GCaMP signals, where the after-stimulus undershoot no longer exists. Accordingly, **Figure 3K** shows a flattened tdTomato trace following the correction. The derived $\Delta C_{HbT}(t)$ (**Figure 3I**) highly resembled the

CBV changes measured by fMRI (**Figure 3L**) and these two time-courses correlated significantly (**Figure 3M**). The derived ΔC_{HbT} showed higher sensitivity than MRI-CBV (**Figure 3N**). We observed no significant time-lag between the ΔC_{HbT} and CBV-fMRI time-courses (**Figure 3O, P**).

<Insert Figure 3 here>

Figure 3Q and 3R demonstrate the corrections of pseudo-undershoot artifacts in GCaMP time-courses of short (1 s) and long (10 s) stimulations, respectively. These artifacts following short bursts of activation were also apparent when optogenetic stimulation was applied in the brain (**Figure S9**). In addition, we also observed a significant correction effect on GCaMP response amplitudes (**Figure S10**). Without proper correction of Hb-absorption artifacts, the accuracy of quantified fluorescence signals is compromised, leading to misinterpretation of fiber-photometry data. This problem could become exacerbated in the absence of time-locked stimulations, as the desired activity could be superimposed on physiological hemodynamic signal changes.

<Insert Figure S9, S10 here>

Impact of Hb-absorption on sustained GCaMP signal measurement using fiber-photometry

To further demonstrate the impact of Hb-absorption on GCaMP signal over an extended period of time, we leverage an acute ethanol challenge protocol (Broadwater et al., 2018; Vaagenes et al., 2015) which has been shown to decrease neuronal activity (Lotfullina and Khazipov, 2018) as well as cerebral perfusion (Broadwater et al., 2018; Kelly et al., 1997; Sano et al., 1993). We virally expressed GCaMP using AAV under the CaMKIIα promoter and tdTomato under the CAG promoter in the prelimbic cortex (PrL) (**Figure 4A**) and then implanted an optical fiber into this target area. On the day of the experiment, ethanol (2 g/kg, 20% v/v, i.p.) was given 5 min after the onset of fiber-photometry recording. After ethanol administration, we observed robust increases in the raw, measured tdTomato (**Figure 4B**) and GCaMP (**Figure 4C**) signals. These changes were ethanol specific, as we did not observe any changes in a separate session where the same group of subjects received vehicle injection (an equal

volume of 0.9% saline, i.p.) (**Figure 4B, C**). Next, we derived $\Delta C_{HbO}\,(t)$, $\Delta C_{HbR}\,(t)$ and $\Delta C_{HbT}\,(t)$ (**Figure 4D**) from the ethanol data using the correction methods identical to that described in **Figure 3** and found robust decreases in $\Delta C_{HbO}\,(t)$ and $\Delta C_{HbT}\,(t)$, in agreement with studies showing reduced Hb affinity for oxygen (Van De Borne et al., 1997) and vasoconstriction (Kudo et al., 2015) following acute alcohol administration. Following our proposed correction, tdTomato trace was flattened as expected **(Figure 4B, E)**. Importantly, the trend of the GCaMP signal was flipped from the unexpected positive changes to the expected negative changes (Lotfullina and Khazipov, 2018) (**Figure 4C, F**). In another two proof-of-concept experiments, we also noted the influence of Hb-absorption on anesthetics- and pharmacology-induced fluorescence signal changes (**Figures S11 and S12**). These data highlight the importance to correct for Hb-absorption in fiber-photometry studies, as misinterpretation may otherwise occur.

<Insert Figure 4, Figure S11, S12 here>

Correction of Hb-absorption artifacts in other fiber-photometry settings

To expand the utility of our method, we modeled and compared the Hb-absorption correction techniques among the following three settings: **(1)** Using a spectrometer with a sequence that interleaves between 405 and 488 nm excitation. GCaMP isosbestic point is around 405 nm (Tian et al., 2009; Dana et al., 2019), where excitation light delivered at this range would evoke GCaMP emission photons irrelevant to the changes in calcium concentration. The GCaMP emission signals from the 405 nm excitation is abbreviated as the $GCaMP_{405}$, in contrast to the $GCaMP_{488}$ excited by the 488 nm laser. The fact that apparent Hb-absorption exists at $GCaMP_{405}$ emission spectrum (**Figure S1**) makes this an appealing alternative approach when another activity-independent fluorescent protein is not expressed. In essence, this provides the reference fluorescence signals similar to that of EYFP in **Figure 2** or tdTomato in **Figure 3**, and allows $\Delta C_{HbO}\,(t)$ and $\Delta C_{HbR}\,(t)$ to be calculated for Hb-absorption correction; **(2)** using $GCaMP_{405}$ data from a spectrometer but only selected three spectral datapoints to mimic the settings using band-pass filters with a limited number of photodetectors (i.e., without using the full

$GCaMP_{405}$ spectrum for correction); and **(3)** regressing out the activity-independent $GCaMP_{405}$ fluorescence signal intensity as seen in (Kim et al., 2016). To provide data for these evaluations, we virally expressed GCaMP6f using AAV under the CaMKIIα promoter and tdTomato under the CAG promoter in the primary motor cortex (M1) of the left hemisphere, and implanted a microelectrode into the M1 of the right hemisphere, allowing electrical stimulation to be delivered (60 Hz, 300 µA, 0.5 ms pulse width for 2 s) and thus time-locked GCaMP signal changes can be induced in the left M1 (**Figure 5A**). The interleaved excitation and acquisition sequences are shown in **Figure 5B**. The raw $GCaMP_{405}$ and $GCaMP_{488}$ responses to stimulation are shown in **Figure 5C**. Similar to that in **Figure 3Q & R**, we observed a rapid increase in the $GCaMP_{488}$ signal, followed by a pseudo-undershoot (Chen et al., 2013; Mittmann et al., 2011). We then compared the aforementioned three settings using this single set of *in vivo* data, thus avoiding a subject and trial-by-trial variability confounds. Respectively to the aforementioned three settings, we present: **(1)** corrected $GCaMP_{488}$ using $\Delta C_{HbO}\ (t)$ and $\Delta C_{HbR}\ (t)$ derived from the full $GCaMP_{405}$ spectrum in **Figure 5D**, **(2)** corrected $GCaMP_{488}$ using $\Delta C_{HbO}\ (t)$ and $\Delta C_{HbR}\ (t)$ derived from three spectral datapoints from the $GCaMP_{405}$ spectrum in **Figure 5E**, and **(3)** corrected $GCaMP_{488}$ by regressing out the $GCaMP_{405}$ signal intensity in **Figure 5F**. Comparisons of the post-stimulus pseudo-undershoot artifacts suggested successful restoration of the $GCaMP_{488}$ signals (i.e., signals rapidly return to zero) via both Hb-absorption-based correction methods, but not via the regression-based method (**Figure 5G**). As tdTomato signals are available from 488 nm excitation (**Figure 5B**), we carried out a similar set of analyses by using tdTomato instead of $GCaMP_{405}$ emission signals (**Figures 5H-K**) and observed successful restoration of the $GCaMP_{488}$ signals via both Hb-absorption-based correction methods, but sustained elevated signals by the regression-based method (**Figures 5H-K**). No significant difference was observed between the full spectrum vs. three-point correction methods (**Figures 5G & L**). Nevertheless, as expected, the HbT computed from either $GCaMP_{405}$ or tdTomato spectrum exhibited lower CNR when using only three spectral datapoints compared to the full spectrum (**Figure 5M**).

<Insert Figure 5 here>

Brain regional differences in hemodynamic response function

Because our proposed technique allows simultaneous measurements of neuronal activity (e.g., GCaMP) and vascular responses (e.g., ΔC_{HbT}) with minimized Hb-absorption artifacts, it offers a significant added benefit towards studying the relationship between the two. This relationship, often termed the hemodynamic response function (HRF), governs the data interpretation of many noninvasive neuroimaging technologies such as fMRI, intrinsic optics, or functional ultrasound (Taylor et al., 2018). While the use of one canonical HRF to model activity throughout the brain remains the most common practice in the field, accumulating evidence shows that HRF is region-dependent (Devonshire et al., 2012; Taylor et al., 2018) and that a thorough understanding of HRF affected by regional cell types, neurochemicals, and subject conditions is crucial to accurately interpret most neuroimaging data(Lecrux and Hamel, 2016). To demonstrate the utility of our proposed technique for computing region- and sensor-dependent HRFs (Chao et al., 2022), we first described the method to compute HRF (**Figure S13A**) similar to that in (Chao et al., 2022) and then validated the results on a dataset not used in HRF computation (**Figure S13B**). Next, we virally expressed GCaMP6f using AAV under the CaMKIIα promoter and tdTomato under the CAG promoter in the primary motor cortex (M1) of the left hemisphere and the caudate putamen (CPu, a.k.a. dorsal striatum) of the right hemisphere (**Figure 6A, B**). We implanted a microelectrode into the M1 of the right hemisphere (**Figure 6A**) such that transcallosal and corticostriatal stimulation could be achieved simultaneously. Upon electrical stimulation (60 Hz, 300 µA, 0.5 ms pulse width for 2 s), we observed robust GCaMP changes in the left M1 and right CPu (**Figure 6C, D**), which are both monosynaptically connected to the stimulation target. Following the calculation of Hb concentration changes, Hb-absorption correction, and computation of HRFs, we observed that M1 and CPu exhibited distinct HRF profiles (**Figure 6C, D**). Interestingly, we also observed distinct HbR polarities between these two regions.

<Insert Figure 6, Figure S13 here>

Discussion

Techniques measuring fluorescence signals in vivo, such as fiber-photometry (Liang et al., 2017; Schlegel et al., 2018; Chao et al., 2022), one-photon microscopy (Bollimunta et al., 2021), two-photon microscopy (Baraghis et al., 2011), or macroscopic imaging through a thinned-skull or implanted-window (Cramer et al., 2021), may all suffer from Hb-absorption. Unlike many imaging techniques that provide spatial information, fiber-photometry does not resolve fluorescence signals emitted from individual cells and its analysis cannot spatially circumvent around the blood vessels. Instead, fiber-photometry utilizes an optical fiber to collect all photons from the targeted volume (**Figure S4A-C**). With the conventional fiber-photometry setting, the targeted volume was reported to be $10^5 – 10^6$ μm^3 with a recording depth approximately at 200 μm from the fiber tip (Pisanello et al., 2019). Our simulated detection volume is well within this range (**Figure S14**). With the average blood volume fraction in the brain and Hb concentration documented in the literature (van Zijl et al., 1998), about 9860 μM Hb would appear within the photometry-detectable brain volume and affect the accuracy of fluorescent sensor measurement by absorbing both the excitation and emission photons. In a normal physiological condition, C_{HbO}, C_{HbR}, and C_{HbT} could change for up to 40 μM (Hillman, 2014) and CBV could change for up to ~20% (Uludağ and Blinder, 2018; Hua et al., 2019) in response to neuronal activity, making such correction to be a time-dependent problem. Our derived changes in ΔC_{HbO}, ΔC_{HbR} and ΔC_{HbT} (**Figure 2F, G, J, Figure 3G-I**), and measured rhoCBV (**Figure 2H**), MRI-CBV (**Figure 3L**) indeed support the amplitude of those changes are possible *in vivo*. Our data indicated that roughly 20% of CBV increase would contribute to 4.08% decrease of green fluorescence signal changes (**Figure S15A,** 95% CI 1.33 - 6.83%), and 2.20% decrease of red fluorescence signal changes (**Figure S15B,** 95% CI 0.57 - 3.84%). Such level of ΔF/F changes on both the green and red sensors are commonly reported in the photometry literature (Chen et al., 2013; Sun et al., 2018) and could be interpreted as the specific sensor activity changes when caution was not exercised. Conventionally, in the brain regions where CBV increases following

local neuronal activation, a pseudo-negative fluorescent sensor activity would be expected. However, in cases where CBV decreases with neuronal inhibition (e.g., **Figure 4**), or on occasion with activation (Shih et al., 2009, 2011, 2014; Schridde et al., 2008; Mishra et al., 2011), a pseudo-positive fluorescence signal would occur. Further, while several techniques are readily available to measure CBV (Kwong et al., 1992; Mintun et al., 1984; Sakai et al., 1985; Siegel et al., 2003) (**Figure 2D, H, Figure 3L**), the correction of Hb-absorption cannot be achieved by simply regressing the CBV signal measured concurrently (**Figure S16**). This is mainly because the absorption of HbO and HbR are wavelength dependent and their respective concentrations change over time (Meng and Alayash, 2017; Prahl, 1999) (**Figure S1**). Our simulation suggested that the accuracy of fluorescence signal could be compromised even without a net CBV change (see **Figure S4D** for plots without shaded background). This makes it crucial to quantify both ΔC_{HbO} and ΔC_{HbR}, so that the true fluorescence signal changes can be restored.

<Insert Figure S14, S15, S16 here>

At present, two major fluorescence-measurement strategies are used in fiber-photometry. One is non-spectrally resolved using a narrow bandpass filter paired with a photodetector (Gunaydin et al., 2014; Kim et al., 2016; Lazarjan et al., 2021). The other is spectrally resolved using a photomultiplier tube array (Cui et al., 2014, 2013) or a spectrometer (Meng et al., 2018; Sun et al., 2018; Chao et al., 2022). The non-spectrally resolved method has the advantage of recording fluorescence signals at a faster speed and can be used with modulated excitation lights and a lock-in amplifier (Gunaydin et al., 2014). In contrast, the spectrally resolved method provides wavelength-dependent information for the fluorescence where the detected photons can be matched with the specific spectral profile of the sensor to improve specificity, or perform spectral unmixing for multiplexing (Meng et al., 2018). If a single non-spectral photodetector is used and ΔC_{HbO} and ΔC_{HbR} cannot be obtained, the Hb-absorption spectra (**Figure S1**) and our simulation results (**Figure S4D**) indicated that far-red sensors are less prone to Hb-

absorption artifacts. This highlights the importance of continually developing fluorescent sensors in the further red-shifted and far-red range (Patriarchi et al., 2020; Shcherbakova, 2021).

While we did not obtain photodetector-based data in this work, we mimicked the photodetector-based setting by sampling data only from three specific spectral datapoints to enter our Hb-absorption correction pipeline. These modeling data support the utility of our proposed technique in the photodetector-setting (Figure 5E & J). Of note, the detector inside the spectrometer used in this study is a high-end back-thinned CCD array (90% quantum efficiency) with TE cooling (40-50 degrees below ambient) to reduce the dark current (Ocean Insight, 2022). For a rough comparison of the reported detector sensitivity, the most common commercial photodiode detectors used in the fiber-photometry have a sensitivity (reported as responsivity) of 0.38 A/W at 550 nm (Doric, 2021), which is similar to 0.40 A/W at 550 nm of the system used in this study (calculated based on 90% quantum efficiency). It should also be noted that we do not have access to ground-truth GCaMP signals (i.e., the "real" GCaMP signal) using fiber-photometry to make an unequivocal comparison. However, GCaMP measurements from cultured neurons without Hb or using two-photon imaging to circumvent blood vessels have collectively demonstrated the absence of post-stimulus undershoot (Chen et al., 2013; Mittmann et al., 2011). Leveraging these observations in the literature, together with the results we obtained in **Figures 2E and 3F**, we believe in the utility of our proposed Hb-absorption correction method. We recognize that the post-stimulus undershoot artifacts may not significantly compromise all fiber-photometry studies, especially for those studying brief time-locked stimulations/tasks. Nevertheless, we consider the post-stimulus undershoot artifact to be a useful marker to benchmark methods dealing with Hb-absorption and thus used it throughout our studies. We suggest caution be exercised when studying spontaneous ongoing neuronal/neurochemical activity dynamics or slower brain state changes using fiber-photometry because the HbO and HbR concentration changes may cause erroneous readings of the desired sensory activity (see **Figures 4, S11, and S12**). Our results also suggested that regression-based model may be suboptimal to restore the GCaMP signal changes in

fiber-photometry (**Figures 5F and K**), and highlighted the benefits in CNR when using a spectrometer system to derive HbO and HbR changes (**Figure 5M**).

The correction method utilizing GCaMP isosbestic excitation (**Figure 5**) is built on the fact that HbO and HbR both present significant absorption at the GCaMP isosbestic excitation wavelength as well as the corresponding emission wavelength. As a result, the fluorescence signal generated from GCaMP isosbestic excitation can be used as the activity-independent fluorescent reference signal in the analytical method proposed in this study and derive ΔC_{HbO} and ΔC_{HbR} to restore the functional GCaMP signals. The potential limitations with this approach are (1) trade-off in temporal resolution because interleaved excitation is required, (2) relatively low CNR (**Figure 5M**, note that about one-tenth of the emission signal was obtained as compared to the 488 nm excitation), (3) higher susceptibility to the pH-related confounds (Shaner et al., 2005; Barnett et al., 2017), and (4) though GCaMP has an isosbestic point at an amenable wavelength for this method, other functional fluorescent sensors may perform optimally at a different wavelength (Akerboom et al., 2012; Sun et al., 2020).

Meng et al. recently described the use of spectrally resolved fiber-photometry for simultaneous recording of calcium activities from direct and indirect medium spiny neurons in the CPu and found that both cell types coordinately control the dynamics of movement (Meng et al., 2018). The opportunity to examine the interactions between cell types and/or neurotransmitters has become increasingly popular in fiber-photometry. If both the green and red spectrum are utilized to encode fluorescent sensor activities, it may be possible to use the interleaved sequence as shown in **Figure 5**, or spectral signals from the unmixing residuals (i.e., remaining autofluorescence) to achieve hemodynamic correction (**Figure S17**). In our hands, the residual method suffers significantly from CNR issues due to very low residual photon counts. However, this approach may demonstrate its utility with the advent of more sensitive spectrometer system or improved unmixing algorithm. Considering the increasing need of multiplexing, a valuable next step should consider establishing an experimental pipeline to achieve motion and Hb-absorption artifact-free measurement of a green and a red fluorescent sensors (e.g.,

GCaMP and jRGECO) in freely-moving animals. This may be achieved by incorporating a far-red activity-independent fluorescent sensor for motion correction first (as Hb-absorption is negligible at this range, see **Figure S1**), followed by Hb-absorption correction using data from isosbestic GCaMP excitation as shown in **Figure 5**.

<Insert Figure S17 here>

Given the irreplaceable roles of noninvasive hemodynamic-based neuroimaging techniques (such as fMRI, near-infrared, intrinsic optics, functional ultrasound, positron emission tomography, etc.) in studying brain function, identifying brain region-dependent HRF is crucial towards an accurate interpretation of hemodynamic-based neuroimaging data. Notably, the current standard fMRI analysis uses one HRF shape across the entire brain. Accumulating literature has pointed to the potential problems with this analysis pipeline because HRF is brain region-dependent (Devonshire et al., 2012; Ekstrom, 2021; Jin et al., 2020; Sloan et al., 2010). The current study and other pioneering studies (Albers et al., 2017; He et al., 2018; Liang et al., 2017; Schlegel et al., 2018; Schmid et al., 2016; Schulz et al., 2012; Schwalm et al., 2017; M. Wang et al., 2018; Zhang et al., 2022; Chao et al., 2022) have together demonstrated that fiber-photometry could be seamlessly coupled with fMRI and provide ground-truth cellular activity to help unravel the relationship between neuronal and hemodynamic responses. These studies have bridged a crucial knowledge gap in interpreting fMRI data. The method proposed in this study further expands the scope of this research area, as it generates hemodynamic signals "free-of-charge", with sensitivity better than fMRI (**Figure 3N**), and the results can be readily compared with the concurrently recorded fluorescent sensor activity. With the spectral photometry recording becoming increasingly popular, the proposed method opens up a unique opportunity to compute HRF in a cell-type dependent, stimulation-circuit dependent, and neurotransmission-dependent manner. We expect that this information can be obtained by performing meta-analysis on fiber-photometry data shared through open-science platform and contribute significantly toward a more accurate interpretation of hemodynamic-based neuroimaging results.

In this study, we demonstrated that significant Hb-absorption artifacts in fiber-photometry data may cause inaccurate measurements and therefore erroneous interpretations. We proposed a method that addresses this issue by quantifying dynamic HbO and HbR absorption changes using activity-independent fluorescence spectra, and we demonstrated that these additional quantitative measurements were efficient in correcting the artifact and retrieve the desired, unperturbed fluorescence signals in fiber-photometry. This approach simultaneously measures HbO, HbR, and the activity of a selected fluorescent sensor, providing an additional experimental capability to investigate the influence of neuronal or neurochemical activity on cerebral hemodynamics. Through a proof-of-principle study, we provide direct evidence that HRF is brain-region dependent, suggesting that the analysis of hemodynamic-based neuroimaging data should not apply a single HRF across all brain regions.

Acknowledgements

We thank UNC CAMRI members and Dr. Elizabeth Hillman for their helpful discussions and critiques. We thank Drs. Lindsay Walton and Dom Cerri for editing the manuscript. This work is supported in part by NIH grants (RF1MH117053, RF1NS086085, R01MH126518, R01MH111429, R01NS091236, P60AA011605, U01AA020023, P50HD103573, S10MH124745, and S10OD026796 to Y.Y.I.S.), the Intramural Research Program of the NIH/NIEHS (1ZIAES103310 to G.C.), the Burroughs Wellcome Fund (CASI Award number 5113244 to N.C.P.), and the Arnold and Mabel Beckman Foundation (2021BYI to N.C.P.).

Author contributions

W.-T.Z., T.-H.H.C., G.C., and Y.-Y.I.S. conceived the project and designed the experiments. W.-T.Z., T.-H.H.C., T.-W. W., E.A.O., J.Z., and R.N. implemented the methods. W.-T.Z., T.-H.H.C, Y.Y., S.-H.L.,

and N.C.P. analyzed data. W.-T.Z., T.-H.H.C, and Y.-Y.I.S. wrote the manuscript with input from all authors. H.Z., G.C, and Y-Y.I.S. supervised the study and provided funding support.

Declaration of interests

The authors declare no competing interests.

References

Akerboom, J., Chen, T.-W., Wardill, T.J., Tian, L., Marvin, J.S., Mutlu, S., Calderón, N.C., Esposti, F., Borghuis, B.G., Sun, X.R., others, 2012. Optimization of a GCaMP calcium indicator for neural activity imaging. J. Neurosci. 32, 13819–13840.

Albers, F., Wachsmuth, L., van Alst, T.M., Faber, C., 2017. Multimodal Functional Neuroimaging by Simultaneous BOLD fMRI and Fiber-Optic Calcium Recordings and Optogenetic Control. Mol. Imaging Biol. https://doi.org/10.1007/s11307-017-1130-6

Baraghis, E., Devor, A., Fang, Q., Srinivasan, V.J., Wu, W., Lesage, F., Ayata, C., Kasischke, K.A., Boas, D.A., Sakadzic, S., 2011. Two-photon microscopy of cortical NADH fluorescence intensity changes: correcting contamination from the hemodynamic response. J. Biomed. Opt. 16, 106003. https://doi.org/10.1117/1.3633339

Barnett, L.M., Hughes, T.E., Drobizhev, M., 2017. Deciphering the molecular mechanism responsible for GCaMP6m's Ca2+-dependent change in fluorescence. PloS One 12, e0170934–e0170934. https://doi.org/10.1371/journal.pone.0170934

Bekar, L.K., Wei, H.S., Nedergaard, M., 2012. The Locus Coeruleus-Norepinephrine Network Optimizes Coupling of Cerebral Blood Volume with Oxygen Demand. J. Cereb. Blood Flow Metab. 32, 2135–2145. https://doi.org/10.1038/jcbfm.2012.115

Bollimunta, A., Santacruz, S.R., Eaton, R.W., Xu, P.S., Morrison, J.H., Moxon, K.A., Carmena, J.M., Nassi, J.J., 2021. Head-mounted microendoscopic calcium imaging in dorsal premotor cortex of behaving rhesus macaque. Cell Rep. 35, 109239.

Broadwater, M.A., Lee, S.-H., Yu, Y., Zhu, H., Crews, F.T., Robinson, D.L., Shih, Y.-Y.I., 2018. Adolescent alcohol exposure decreases frontostriatal resting-state functional connectivity in adulthood. Addict. Biol. 23, 810–823.

Chao, T.-H.H., Chen, J.-H., Yen, C.-T., 2018. Plasticity changes in forebrain activity and functional connectivity during neuropathic pain development in rats with sciatic spared nerve injury. Mol. Brain 11, 55. https://doi.org/10.1186/s13041-018-0398-z

Chao, T.-H.H., Zhang, W.-T., Hsu, L.-M., Cerri, D.H., Wang, T.-W., Shih, Y.-Y.I., 2022. Computing hemodynamic response functions from concurrent spectral fiber-photometry and fMRI data. Neurophotonics 9, 032205.

Chen, T.W., Wardill, T.J., Sun, Y., Pulver, S.R., Renninger, S.L., Baohan, A., Schreiter, E.R., Kerr, R.A., Orger, M.B., Jayaraman, V., Looger, L.L., Svoboda, K., Kim, D.S., 2013. Ultrasensitive fluorescent proteins for imaging neuronal activity. Nature 499, 295–300. https://doi.org/10.1038/nature12354

Chen, X., Sobczak, F., Chen, Y., Jiang, Y., Qian, C., Lu, Z., Ayata, C., Logothetis, N.K., Yu, X., 2019. Mapping optogenetically-driven single-vessel fMRI with concurrent neuronal calcium recordings in the rat hippocampus. Nat. Commun. 10, 5239. https://doi.org/10.1038/s41467-019-12850-x

Cox, R.W., 1996. AFNI: software for analysis and visualization of functional magnetic resonance neuroimages. Comput. Biomed. Res. Int. J. 29, 162–173. https://doi.org/10.1006/cbmr.1996.0014

Cramer, S.W., Carter, R.E., Aronson, J.D., Kodandaramaiah, S.B., Ebner, T.J., Chen, C.C., 2021. Through the looking glass: A review of cranial window technology for optical access to the brain. J. Neurosci. Methods 354, 109100.

Cui, G., Jun, S.B., Jin, X., Luo, G., Pham, M.D., Lovinger, D.M., Vogel, S.S., Costa, R.M., 2014. Deep brain optical measurements of cell type-specific neural activity in behaving mice. Nat Protoc 9, 1213–28. https://doi.org/10.1038/nprot.2014.080

Cui, G., Jun, S.B., Jin, X., Pham, M.D., Vogel, S.S., Lovinger, D.M., Costa, R.M., 2013. Concurrent Activation of Striatal Direct and Indirect Pathways During Action Initiation. Nature 494, 238–242. https://doi.org/10.1038/nature11846

Dana, H., Mohar, B., Sun, Y., Narayan, S., Gordus, A., Hasseman, J.P., Tsegaye, G., Holt, G.T., Hu, A., Walpita, D., Patel, R., Macklin, J.J., Bargmann, C.I., Ahrens, M.B., Schreiter, E.R., Jayaraman, V., Looger, L.L., Svoboda, K., Kim, D.S., 2016. Sensitive red protein calcium indicators for imaging neural activity. eLife 5, e12727. https://doi.org/10.7554/eLife.12727

Dana, H., Sun, Y., Mohar, B., Hulse, B.K., Kerlin, A.M., Hasseman, J.P., Tsegaye, G., Tsang, A., Wong, A., Patel, R., others, 2019. High-performance calcium sensors for imaging activity in neuronal populations and microcompartments. Nat. Methods 16, 649–657.

Decot, H.K., Namboodiri, V.M.K., Gao, W., McHenry, J.A., Jennings, J.H., Lee, S.-H., Kantak, P.A., Jill Kao, Y.-C., Das, M., Witten, I.B., Deisseroth, K., Shih, Y.-Y.I., Stuber, G.D., 2017. Coordination of Brain-Wide Activity Dynamics by Dopaminergic Neurons. Neuropsychopharmacol. Off. Publ. Am. Coll. Neuropsychopharmacol. 42, 615–627. https://doi.org/10.1038/npp.2016.151

Devonshire, I.M., Papadakis, N.G., Port, M., Berwick, J., Kennerley, A.J., Mayhew, J.E., Overton, P.G., 2012. Neurovascular coupling is brain region-dependent. Neuroimage 59, 1997–2006. https://doi.org/10.1016/j.neuroimage.2011.09.050

Devor, A., Dunn, A.K., Andermann, M.L., Ulbert, I., Boas, D.A., Dale, A.M., 2003. Coupling of total hemoglobin concentration, oxygenation, and neural activity in rat somatosensory cortex. Neuron 39, 353–359. https://doi.org/10.1016/s0896-6273(03)00403-3

Doric, 2021. Integrated Fluorescence Mini Cubes (Gen2) User Manual.

Ekstrom, A.D., 2021. Regional variation in neurovascular coupling and why we still lack a Rosetta Stone. Philos. Trans. R. Soc. Lond. B. Biol. Sci. 376, 20190634. https://doi.org/10.1098/rstb.2019.0634

Gunaydin, L.A., Grosenick, L., Finkelstein, J.C., Kauvar, I.V., Fenno, L.E., Adhikari, A., Lammel, S., Mirzabekov, J.J., Airan, R.D., Zalocusky, K.A., Tye, K.M., Anikeeva, P., Malenka, R.C., Deisseroth, K., 2014. Natural neural projection dynamics underlying social behavior. Cell 157, 1535–1551. https://doi.org/10.1016/j.cell.2014.05.017

Hansen, L.P., 1982. Large Sample Properties of Generalized Method of Moments Estimators. Econometrica 50, 1029–1054. https://doi.org/10.2307/1912775

He, Y., Wang, M., Chen, X., Pohmann, R., Polimeni, J.R., Scheffler, K., Rosen, B.R., Kleinfeld, D., Yu, X., 2018. Ultra-Slow Single-Vessel BOLD and CBV-Based fMRI Spatiotemporal Dynamics and Their Correlation with Neuronal Intracellular Calcium Signals. Neuron 97, 925-939.e5. https://doi.org/10.1016/j.neuron.2018.01.025

Henyey, L.G., Greenstein, J.L., 1941. Diffuse radiation in the galaxy. Astrophys J 93, 70–83.

Hillman, E.M., 2014. Coupling mechanism and significance of the BOLD signal: a status report. Annu Rev Neurosci 37, 161–81. https://doi.org/10.1146/annurev-neuro-071013-014111

Hillman, E.M.C., 2007. Optical brain imaging in vivo: techniques and applications from animal to man. J. Biomed. Opt. 12, 051402–051402. https://doi.org/10.1117/1.2789693

Hu, X., Yacoub, E., 2012. The story of the initial dip in fMRI. NeuroImage 62, 1103–1108. https://doi.org/10.1016/j.neuroimage.2012.03.005

Hua, J., Liu, P., Kim, T., Donahue, M., Rane, S., Chen, J.J., Qin, Q., Kim, S.-G., 2019. MRI techniques to measure arterial and venous cerebral blood volume. Neuroimage 187, 17–31.

Jin, M., Wang, L., Wang, H., Han, X., Diao, Z., Guo, W., Yang, Z., Ding, H., Wang, Zheng, Zhang, P., Zhao, P., Lv, H., Liu, W., Wang, Zhenchang, 2020. Disturbed neurovascular coupling in hemodialysis patients. PeerJ 8, e8989. https://doi.org/10.7717/peerj.8989

Jones-Tabah, J., Mohammad, H., Clarke, P.B., Hébert, T.E., 2021. In vivo detection of GPCR-dependent signaling using fiber photometry and FRET-based biosensors. Methods.

Kelly, D.F., Lee, S.M., Pinanong, P.A., Hovda, D.A., 1997. Paradoxical effects of acute ethanolism in experimental brain injury. J. Neurosurg. 86, 876–882.

Kim, C.K., Yang, S.J., Pichamoorthy, N., Young, N.P., Kauvar, I., Jennings, J.H., Lerner, T.N., Berndt, A., Lee, S.Y., Ramakrishnan, C., Davidson, T.J., Inoue, M., Bito, H., Deisseroth, K., 2016. Simultaneous fast measurement of circuit dynamics at multiple sites across the mammalian brain. Nat. Methods 13, 325–328. https://doi.org/10.1038/nmeth.3770

Kudo, R., Yuui, K., Kasuda, S., Hatake, K., 2015. [Effect of alcohol on vascular function]. Nihon Arukoru Yakubutsu Igakkai Zasshi 50, 123–134.

Kwong, K.K., Belliveau, J.W., Chesler, D.A., Goldberg, I.E., Weisskoff, R.M., Poncelet, B.P., Kennedy, D.N., Hoppel, B.E., Cohen, M.S., Turner, R., et al, 1992. Dynamic magnetic resonance imaging of human brain activity during primary sensory stimulation. Proc Natl Acad Sci U A 89, 5675–9.

Lazarjan, V.K., Gashti, A.B., Feshki, M., Garnier, A., Gosselin, B., 2021. Miniature Fiber-Spectrophotometer for Real-Time Biomarkers Detection. IEEE Sens. J. 21, 14822–14837. https://doi.org/10.1109/JSEN.2021.3072578

Lecrux, C., Hamel, E., 2016. Neuronal networks and mediators of cortical neurovascular coupling responses in normal and altered brain states. Philos Trans R Soc Lond B Biol Sci 371. https://doi.org/10.1098/rstb.2015.0350

Liang, Z., Ma, Y., Watson, G.D.R., Zhang, N., 2017. Simultaneous GCaMP6-based fiber photometry and fMRI in rats. J Neurosci Methods 289, 31–38. https://doi.org/10.1016/j.jneumeth.2017.07.002

Lotfullina, N., Khazipov, R., 2018. Ethanol and the developing brain: inhibition of neuronal activity and neuroapoptosis. The Neuroscientist 24, 130–141.

Luchsinger, J.R., Fetterly, T.L., Williford, K.M., Salimando, G.J., Doyle, M.A., Maldonado, J., Simerly, R.B., Winder, D.G., Centanni, S.W., 2021. Delineation of an insula-BNST circuit engaged by struggling behavior that regulates avoidance in mice. Nat. Commun. 12, 3561. https://doi.org/10.1038/s41467-021-23674-z

Ma, Y., Shaik, M.A., Kim, S.H., Kozberg, M.G., Thibodeaux, D.N., Zhao, H.T., Yu, H., Hillman, E.M.C., 2016. Wide-field optical mapping of neural activity and brain haemodynamics: considerations and novel approaches. Philos. Trans. R. Soc. Lond. B. Biol. Sci. 371. https://doi.org/10.1098/rstb.2015.0360

Mächler, P., Fomin-Thunemann, N., Thunemann, M., Sætra, M.J., Desjardins, M., Kılıç, K., Şencan, I., Li, B., Saisan, P., Cheng, Q., others, 2021. Microscopic Quantification of Oxygen Consumption across Cortical Layers. bioRxiv.

Marvin, J.S., Borghuis, B.G., Tian, L., Cichon, J., Harnett, M.T., Akerboom, J., Gordus, A., Renninger, S.L., Chen, T.-W., Bargmann, C.I., Orger, M.B., Schreiter, E.R., Demb, J.B., Gan, W.-B., Hires, S.A., Looger, L.L., 2013. An optimized fluorescent probe for visualizing glutamate neurotransmission. Nat. Methods 10, 162–170. https://doi.org/10.1038/nmeth.2333

Marvin, J.S., Shimoda, Y., Magloire, V., Leite, M., Kawashima, T., Jensen, T.P., Kolb, I., Knott, E.L., Novak, O., Podgorski, K., Leidenheimer, N.J., Rusakov, D.A., Ahrens, M.B., Kullmann, D.M., Looger, L.L., 2019. A genetically encoded fluorescent sensor for in vivo imaging of GABA. Nat. Methods 16, 763–770. https://doi.org/10.1038/s41592-019-0471-2

Meng, C., Zhou, J., Papaneri, A., Peddada, T., Xu, K., Cui, G., 2018. Spectrally Resolved Fiber Photometry for Multi-component Analysis of Brain Circuits. Neuron 98, 707-717 e4. https://doi.org/10.1016/j.neuron.2018.04.012

Meng, F., Alayash, A.I., 2017. Determination of extinction coefficients of human hemoglobin in various redox states. Anal. Biochem. 521, 11–19. https://doi.org/10.1016/j.ab.2017.01.002

Mintun, M.A., Raichle, M.E., Martin, W.R., Herscovitch, P., 1984. Brain oxygen utilization measured with O-15 radiotracers and positron emission tomography. J. Nucl. Med. Off. Publ. Soc. Nucl. Med. 25, 177–187.

Mishra, A.M., Ellens, D.J., Schridde, U., Motelow, J.E., Purcaro, M.J., DeSalvo, M.N., Enev, M., Sanganahalli, B.G., Hyder, F., Blumenfeld, H., 2011. Where fMRI and Electrophysiology Agree to Disagree: Corticothalamic and Striatal Activity Patterns in the WAG/Rij Rat. J. Neurosci. 31, 15053–15064. https://doi.org/10.1523/jneurosci.0101-11.2011

Mittmann, W., Wallace, D.J., Czubayko, U., Herb, J.T., Schaefer, A.T., Looger, L.L., Denk, W., Kerr, J.N.D., 2011. Two-photon calcium imaging of evoked activity from L5 somatosensory neurons in vivo. Nat. Neurosci. 14, 1089–1093. https://doi.org/10.1038/nn.2879

Nakabayashi, T., Oshita, S., Sumikawa, R., Sun, F., Kinjo, M., Ohta, N., 2012. pH dependence of the fluorescence lifetime of enhanced yellow fluorescent protein in solution and cells. J. Photochem. Photobiol. Chem. 235, 65–71.

Ocean Insight, 2022. QE Pro-FL Product Details.

Pais-Roldán, P., Takahashi, K., Sobczak, F., Chen, Y., Zhao, X., Zeng, H., Jiang, Y., Yu, X., 2020. Indexing brain state-dependent pupil dynamics with simultaneous fMRI and optical fiber calcium recording. Proc. Natl. Acad. Sci. U. S. A. 117, 6875–6882. https://doi.org/10.1073/pnas.1909937117

Patriarchi, T., Cho, J.R., Merten, K., Howe, M.W., Marley, A., Xiong, W.-H., Folk, R.W., Broussard, G.J., Liang, R., Jang, M.J., Zhong, H., Dombeck, D., von Zastrow, M., Nimmerjahn, A., Gradinaru, V., Williams, J.T., Tian, L., 2018. Ultrafast neuronal imaging of dopamine dynamics with designed genetically encoded sensors. Science 360. https://doi.org/10.1126/science.aat4422

Patriarchi, T., Mohebi, A., Sun, J., Marley, A., Liang, R., Dong, C., Puhger, K., Mizuno, G.O., Davis, C.M., Wiltgen, B., von Zastrow, M., Berke, J.D., Tian, L., 2020. An expanded palette of dopamine sensors for multiplex imaging in vivo. Nat. Methods 17, 1147–1155. https://doi.org/10.1038/s41592-020-0936-3

Pisanello, M., Pisano, F., Hyun, M., Maglie, E., Balena, A., De Vittorio, M., Sabatini, B.L., Pisanello, F., 2019. The Three-Dimensional Signal Collection Field for Fiber Photometry in Brain Tissue. Front. Neurosci. 13, 82. https://doi.org/10.3389/fnins.2019.00082

Pisano, F., Pisanello, M., Lee, S.J., Lee, J., Maglie, E., Balena, A., Sileo, L., Spagnolo, B., Bianco, M., Hyun, M., De Vittorio, M., Sabatini, B.L., Pisanello, F., 2019. Depth-resolved fiber photometry with a single tapered optical fiber implant. Nat. Methods 16, 1185–1192. https://doi.org/10.1038/s41592-019-0581-x

Prahl, S., 1999. Optical Absorption of Hemoglobin. URL http://omlc.org/spectra/hemoglobin

Ruffin, V., Salameh, A., Boron, W., Parker, M., 2014. Intracellular pH regulation by acid-base transporters in mammalian neurons. Front. Physiol. 5. https://doi.org/10.3389/fphys.2014.00043

Rungta, R.L., Osmanski, B.-F., Boido, D., Tanter, M., Charpak, S., 2017. Light controls cerebral blood flow in naive animals. Nat. Commun. 8, 14191. https://doi.org/10.1038/ncomms14191

Sakai, F., Nakazawa, K., Tazaki, Y., Ishii, K., Hino, H., Igarashi, H., Kanda, T., 1985. Regional cerebral blood volume and hematocrit measured in normal human volunteers by single-photon emission computed tomography. J. Cereb. Blood Flow Metab. Off. J. Int. Soc. Cereb. Blood Flow Metab. 5, 207–213. https://doi.org/10.1038/jcbfm.1985.27

Sano, M., Wendt, P.E., Wirsén, A., Stenberg, G., Risberg, J., Ingvar, D.H., 1993. Acute effects of alcohol on regional cerebral blood flow in man. J. Stud. Alcohol 54, 369–376.

Schlegel, F., Sych, Y., Schroeter, A., Stobart, J., Weber, B., Helmchen, F., Rudin, M., 2018. Fiber-optic implant for simultaneous fluorescence-based calcium recordings and BOLD fMRI in mice. Nat Protoc 13, 840–855. https://doi.org/10.1038/nprot.2018.003

Schmid, F., Wachsmuth, L., Schwalm, M., Prouvot, P.H., Jubal, E.R., Fois, C., Pramanik, G., Zimmer, C., Faber, C., Stroh, A., 2016. Assessing sensory versus optogenetic network activation by combining

(o)fMRI with optical Ca2+ recordings. J Cereb Blood Flow Metab 36, 1885–1900. https://doi.org/10.1177/0271678x15619428

Schridde, U., Khubchandani, M., Motelow, J.E., Sanganahalli, B.G., Hyder, F., Blumenfeld, H., 2008. Negative BOLD with large increases in neuronal activity. Cereb. Cortex N. Y. N 1991 18, 1814–1827. https://doi.org/10.1093/cercor/bhm208

Schulz, K., Sydekum, E., Krueppel, R., Engelbrecht, C.J., Schlegel, F., Schroter, A., Rudin, M., Helmchen, F., 2012. Simultaneous BOLD fMRI and fiber-optic calcium recording in rat neocortex. Nat Methods 9, 597–602. https://doi.org/10.1038/nmeth.2013

Schwalm, M., Schmid, F., Wachsmuth, L., Backhaus, H., Kronfeld, A., Aedo Jury, F., Prouvot, P.H., Fois, C., Albers, F., van Alst, T., Faber, C., Stroh, A., 2017. Cortex-wide BOLD fMRI activity reflects locally-recorded slow oscillation-associated calcium waves. Elife 6. https://doi.org/10.7554/eLife.27602

Shaner, N.C., Steinbach, P.A., Tsien, R.Y., 2005. A guide to choosing fluorescent proteins. Nat. Methods 2, 905–909.

Shcherbakova, D.M., 2021. Near-infrared and far-red genetically encoded indicators of neuronal activity. J. Neurosci. Methods 362, 109314.

Shih, Y.Y., Chen, C.C., Shyu, B.C., Lin, Z.J., Chiang, Y.C., Jaw, F.S., Chen, Y.Y., Chang, C., 2009. A new scenario for negative functional magnetic resonance imaging signals: endogenous neurotransmission. J Neurosci 29, 3036–44. https://doi.org/10.1523/JNEUROSCI.3447-08.2009

Shih, Y.Y., Li, G., Muir, E.R., De La Garza, B.H., Kiel, J.W., Duong, T.Q., 2012. Pharmacological MRI of the choroid and retina: blood flow and BOLD responses during nitroprusside infusion. Magn Reson Med 68, 1273–8. https://doi.org/10.1002/mrm.24112

Shih, Y.-Y.I., Huang, S., Chen, Y.-Y., Lai, H.-Y., Kao, Y.-C.J., Du, F., Hui, E.S., Duong, T.Q., 2014. Imaging neurovascular function and functional recovery after stroke in the rat striatum using forepaw stimulation. J. Cereb. Blood Flow Metab. Off. J. Int. Soc. Cereb. Blood Flow Metab. 34, 1483–1492. https://doi.org/10.1038/jcbfm.2014.103

Shih, Y.-Y.I., Wang, L., De La Garza, B.H., Li, G., Cull, G., Kiel, J.W., Duong, T.Q., 2013. Quantitative retinal and choroidal blood flow during light, dark adaptation and flicker light stimulation in rats using fluorescent microspheres. Curr. Eye Res. 38, 292–298. https://doi.org/10.3109/02713683.2012.756526

Shih, Y.-Y.I., Wey, H.-Y., De La Garza, B.H., Duong, T.Q., 2011. Striatal and cortical BOLD, blood flow, blood volume, oxygen consumption, and glucose consumption changes in noxious forepaw electrical stimulation. J. Cereb. Blood Flow Metab. Off. J. Int. Soc. Cereb. Blood Flow Metab. 31, 832–841. https://doi.org/10.1038/jcbfm.2010.173

Siegel, A.M., Culver, J.P., Mandeville, J.B., Boas, D.A., 2003. Temporal comparison of functional brain imaging with diffuse optical tomography and fMRI during rat forepaw stimulation. Phys. Med. Biol. 48, 1391–1403. https://doi.org/10.1088/0031-9155/48/10/311

Sloan, H.L., Austin, V.C., Blamire, A.M., Schnupp, J.W.H., Lowe, A.S., Allers, K.A., Matthews, P.M., Sibson, N.R., 2010. Regional differences in neurovascular coupling in rat brain as determined by fMRI and electrophysiology. NeuroImage 53, 399–411. https://doi.org/10.1016/j.neuroimage.2010.07.014

Smith, A.F., Doyeux, V., Berg, M., Peyrounette, M., Haft-Javaherian, M., Larue, A.-E., Slater, J.H., Lauwers, F., Blinder, P., Tsai, P., Kleinfeld, D., Schaffer, C.B., Nishimura, N., Davit, Y., Lorthois, S., 2019. Brain Capillary Networks Across Species: A few Simple Organizational Requirements Are Sufficient to Reproduce Both Structure and Function. Front. Physiol. 10, 233. https://doi.org/10.3389/fphys.2019.00233

Sun, F., Zeng, J., Jing, M., Zhou, J., Feng, J., Owen, S.F., Luo, Y., Li, F., Wang, H., Yamaguchi, T., Yong, Z., Gao, Y., Peng, W., Wang, L., Zhang, S., Du, J., Lin, D., Xu, M., Kreitzer, A.C., Cui, G., Li, Y., 2018. A Genetically Encoded Fluorescent Sensor Enables Rapid and Specific Detection of Dopamine in Flies, Fish, and Mice. Cell 174, 481-496.e19. https://doi.org/10.1016/j.cell.2018.06.042

Sun, F., Zhou, J., Dai, B., Qian, T., Zeng, J., Li, X., Zhuo, Y., Zhang, Y., Wang, Y., Qian, C., Tan, K., Feng, J., Dong, H., Lin, D., Cui, G., Li, Y., 2020. Next-generation GRAB sensors for monitoring dopaminergic activity in vivo. Nat. Methods 17, 1156–1166. https://doi.org/10.1038/s41592-020-00981-9

Sych, Y., Chernysheva, M., Sumanovski, L.T., Helmchen, F., 2019. High-density multi-fiber photometry for studying large-scale brain circuit dynamics. Nat. Methods 16, 553–560. https://doi.org/10.1038/s41592-019-0400-4

Taylor, A.J., Kim, J.H., Ress, D., 2018. Characterization of the hemodynamic response function across the majority of human cerebral cortex. NeuroImage 173, 322–331. https://doi.org/10.1016/j.neuroimage.2018.02.061

Tian, L., Hires, S.A., Mao, T., Huber, D., Chiappe, M.E., Chalasani, S.H., Petreanu, L., Akerboom, J., McKinney, S.A., Schreiter, E.R., others, 2009. Imaging neural activity in worms, flies and mice with improved GCaMP calcium indicators. Nat. Methods 6, 875–881.

Uludağ, K., Blinder, P., 2018. Linking brain vascular physiology to hemodynamic response in ultra-high field MRI. NeuroImage 168, 279–295. https://doi.org/10.1016/j.neuroimage.2017.02.063

Unekawa, M., Tomita, Y., Toriumi, H., Osada, T., Masamoto, K., Kawaguchi, H., Itoh, Y., Kanno, I., Suzuki, N., 2015. Hyperperfusion counteracted by transient rapid vasoconstriction followed by long-lasting oligemia induced by cortical spreading depression in anesthetized mice. J. Cereb. Blood Flow Metab. Off. J. Int. Soc. Cereb. Blood Flow Metab. 35, 689–698. https://doi.org/10.1038/jcbfm.2014.250

Vaagenes, I.C., Tsai, S.-Y., Ton, S.T., Husak, V.A., McGuire, S.O., O'Brien, T.E., Kartje, G.L., 2015. Binge ethanol prior to traumatic brain injury worsens sensorimotor functional recovery in rats. PLoS One 10, e0120356.

Valdés-Hernández, P.A., Sumiyoshi, A., Nonaka, H., Haga, R., Aubert-Vásquez, E., Ogawa, T., Iturria-Medina, Y., Riera, J.J., Kawashima, R., 2011. An in vivo MRI Template Set for Morphometry, Tissue Segmentation, and fMRI Localization in Rats. Front. Neuroinformatics 5, 26. https://doi.org/10.3389/fninf.2011.00026

Valley, M.T., Moore, M.G., Zhuang, J., Mesa, N., Castelli, D., Sullivan, D., Reimers, M., Waters, J., 2020. Separation of hemodynamic signals from GCaMP fluorescence measured with wide-field imaging. J. Neurophysiol. 123, 356–366.

Van De Borne, P., Mark, A.L., Montano, N., Mion, D., Somers, V.K., 1997. Effects of alcohol on sympathetic activity, hemodynamics, and chemoreflex sensitivity. Hypertension 29, 1278–1283.

van Zijl, P.C., Eleff, S.M., Ulatowski, J.A., Oja, J.M., Uluğ, A.M., Traystman, R.J., Kauppinen, R.A., 1998. Quantitative assessment of blood flow, blood volume and blood oxygenation effects in functional magnetic resonance imaging. Nat. Med. 4, 159–167. https://doi.org/10.1038/nm0298-159

Vasanawala, S.S., Nguyen, K.-L., Hope, M.D., Bridges, M.D., Hope, T.A., Reeder, S.B., Bashir, M.R., 2016. Safety and technique of ferumoxytol administration for MRI. Magn. Reson. Med. 75, 2107–2111. https://doi.org/10.1002/mrm.26151

Wang, H., Jing, M., Li, Y., 2018. Lighting up the brain: genetically encoded fluorescent sensors for imaging neurotransmitters and neuromodulators. Curr. Opin. Neurobiol. 50, 171–178. https://doi.org/10.1016/j.conb.2018.03.010

Wang, M., He, Y., Sejnowski, T.J., Yu, X., 2018. Brain-state dependent astrocytic Ca(2+) signals are coupled to both positive and negative BOLD-fMRI signals. Proc. Natl. Acad. Sci. U. S. A. 115, E1647–E1656. https://doi.org/10.1073/pnas.1711692115

Wei, H., Bruns, O.T., Kaul, M.G., Hansen, E.C., Barch, M., Wiśniowska, A., Chen, O., Chen, Y., Li, N., Okada, S., Cordero, J.M., Heine, M., Farrar, C.T., Montana, D.M., Adam, G., Ittrich, H., Jasanoff, A., Nielsen, P., Bawendi, M.G., 2017. Exceedingly small iron oxide nanoparticles as positive MRI contrast agents. Proc. Natl. Acad. Sci. U. S. A. 114, 2325–2330. https://doi.org/10.1073/pnas.1620145114

Worsley, K.J., Friston, K.J., 1995. Analysis of fMRI time-series revisited--again. NeuroImage 2, 173–181. https://doi.org/10.1006/nimg.1995.1023

Zhang, Q., Cramer, S.R., Ma, Z., Turner, K.L., Gheres, K.W., Liu, Y., Drew, P.J., Zhang, N., 2022. Brain-wide ongoing activity is responsible for significant cross-trial BOLD variability. Cereb. Cortex.

Zhang, Y.-F., Vargas Cifuentes, L., Wright, K.N., Bhattarai, J.P., Mohrhardt, J., Fleck, D., Janke, E., Jiang, C., Cranfill, S.L., Goldstein, N., others, 2021. Ventral striatal islands of Calleja neurons control grooming in mice. Nat. Neurosci. 24, 1699–1710.

Zhao, Y., Qiu, L., Sun, Y., Huang, C., Li, T., 2017. Optimal hemoglobin extinction coefficient data set for near-infrared spectroscopy. Biomed. Opt. Express 8, 5151–5159. https://doi.org/10.1364/BOE.8.005151

STAR★METHODS

KEY RESOURCES TABLE

REAGENT OR RESOURCE	SOURCE	IDENTIFIER
Recombinant DNA		
AAV5-CaMKIIα-EYFP	UNC Vector Core	N/A
AAV9-CaMKIIα-GCaMP6f-WPRE-SV40	U.Penn Vector Core	AV-9-PV3435
AAV9-CAG-tdTomato	UNC Vector Core	N/A
AAV9-CaMKIIα-ChR2-EYFP	UNC Vector Core	N/A
Software and Algorithms		
MATLAB	Mathworks	R2019b
RStudio	RStudio Inc.	Version 1.0.136
Other		
488 nm laser and remote	Coherent	OBIS 488 LS (60 mW)
561 nm laser and remote	Coherent	OBIS 561 LS (50 mW)
Spectrometer	Ocean Optics	QE-pro
Optic patch cable	Thorlabs	FT200EMT (200 mm, 0.39 NA)
Uncleaved fiber optic cannula	Thorlabs	CFMC12U-20 (200 mm, 0.39 NA)
Bipolar Tungsten electrode	P1 Technologies	MS303T/2C-B/SP ELEC .008/.2MM TW TUNGSTEN (MRI)

Monte Carlo simulation for photon transport in fiber-photometry recording

The Monte Carlo simulation of photon transport during fiber-photometry recording was achieved in two steps: 1) excitation light path simulation and 2) emission light path simulation. The goal was to first build a database composed of a large number of possible excitation light paths. After which, an emission starting point can be randomly selected from the excitation light path database for emission light path simulation.

For the excitation light path simulation, we built the database by repeatedly launching excitation photon packets that started with a unity weight = 1. The photon packets deposited weight due to absorption at each step of traveling through the simulated brain, and the photon packet's current locations and remaining weights were logged along the way. Each excitation photon packet repeatedly underwent the following steps (**Figure S3**, left panel), until it was either terminated or transmitted out of the brain.

Step 1: Launching a photon packet (**Figure S3**, left panel a and b):

In our model, we launched our photon packets from an optic fiber tip with a diameter of 200 μm; the range of possible launch directions, or so-called acceptance angles, would be limited by the fiber numerical aperture (NA) according to Snell's law. For applications, the NA is most commonly expressed as:

$$NA_{fiber} = n_i \sin \theta_a \tag{2}$$

where θ_a is the maximum 1/2 acceptance angle of the fiber, and n_i is the index of refraction of the material outside of the fiber. With this in mind, we simply set the initial launch position randomly within the surface of fiber tip, along with a random initial launch direction that was within the range of acceptance angles. This can be easily done by using three Cartesian coordinates (x, y, z) and three direction cosines (v_x, v_y, v_z) to determine the initial position and direction, respectively.

For initial position:

$$x = r_{fiber}\sqrt{\xi_1}\cos(2\pi\xi_2)$$

$$y = r_{fiber}\sqrt{\xi_1}\sin(2\pi\xi_2)$$

$$z = 0 \quad (3)$$

For initial direction:

$$v_x = \sin(\theta_a\xi_3)\cos(2\pi\xi_4)$$

$$v_y = \sin(\theta_a\xi_3)\sin(2\pi\xi_4)$$

$$v_z = \cos(\theta_a\xi_3) \quad (4)$$

where r_{fiber} is the radius of the optic fiber, and ξ_{1-4} are the independent random numbers between 0 and 1.

Step 2: Step size selection and photon packet movement (**Figure S3**, left panel 1-2 and right panel 5-6):

The step size s is the distance that the photon packet travels between interaction sites. In our study, we selected a step size using the following function derived from the inverse distribution method and the Beer–Lambert law:

$$s = -\frac{\ln\xi}{\mu_t} \quad (5)$$

where ξ is a random number between 0 and 1, and μ_t is the total interaction coefficient (the sum of the absorption coefficient (μ_a) and scattering coefficient (μ_s) of brain tissue). The μ_a and μ_s for distinct wavelengths of a traveling photon were derived from the optical absorption and scattering properties provided by an online database from Oregon Medical Laser Center, Oregon Health & Science University

(https://omlc.org/software/mc/mcxyz/index.html). We assumed 3% blood with 75% average oxygen saturation in our simulated brain.

Once the step size was selected, the photon packet traveled for distance s in the direction defined by direction cosines, and the coordinates were updated as follows:

$$x \leftarrow x + v_x s$$

$$y \leftarrow y + v_y s$$

$$z \leftarrow z + v_z s \tag{6}$$

Step 3: Absorption and scattering (**Figure S3**, left panel 3-4 and right panel 7-8):

At each interaction site, photon weight was partially absorbed by brain tissue, and the decreased fraction of the weight Δw can be defined as:

$$\Delta w = w(1 - e^{-\mu_a s}) \tag{7}$$

The weight of the photon packet was then updated as follows:

$$w \leftarrow w - \Delta w \tag{8}$$

Following absorption, the photon packet was scattered. The scattering direction was defined by both scattering angle θ and polar angle φ. The scattering angle was determined using the Henyey-Greenstein phase function(Henyey and Greenstein, 1941):

$$\cos\theta = \begin{cases} \frac{1}{2g}\left[1 + g^2 - \left(\frac{1 - g^2}{1 - g + 2g\xi}\right)^2\right] & if\ g \neq 0 \\ 1 - 2\xi & if\ g = 0 \end{cases} \tag{9}$$

where g refers to scattering anisotropy, which has a value between −1 and 1. When g is 0, it generally indicates that the scattering is isotropic. As g approaches 1 or -1, the scattering is confined to forwards and backwards, respectively.

The polar angle was assumed to be uniformly distributed between 0 and 2π, as below:

$$\varphi = 2\pi\xi \tag{10}$$

With these angles and the original direction cosines, we were able to calculate the new set of propagation direction cosines, which can be represented in the global coordinate system as follows:

$$v'_x = \begin{cases} \dfrac{\sin\theta\left(v_x v_z \cos\varphi - v_y \sin\varphi\right)}{\sqrt{1-v_z^2}} + \mu_x \cos\theta & if\ v_z \neq 1 \cap \mu_z \neq -1 \\ \sin\theta\cos\varphi & if\ v_z = 1 \cup \mu_z = -1 \end{cases}$$

$$v'_y = \begin{cases} \dfrac{\sin\theta\left(v_y v_z \cos\varphi - v_x \sin\varphi\right)}{\sqrt{1-v_z^2}} + \mu_y \cos\theta & if\ v_z \neq 1 \cap \mu_z \neq -1 \\ \sin\theta\sin\varphi & if\ v_z = 1 \\ -\sin\theta\sin\varphi & if\ v_z = -1 \end{cases}$$

$$v'_z = \begin{cases} -\sqrt{1-v_z^2}\sin\theta\cos\varphi + v_z\cos\theta & if\ v_z \neq 1 \cap \mu_z \neq -1 \\ \cos\theta & if\ v_z = 1 \\ -\cos\theta & if\ v_z = -1 \end{cases} \tag{11}$$

Step 4: Photon termination

Steps 2 and 3 were repeated until the weight of the photon packet reached 10^{-4} or less, then the simulation for this particular photon packet was terminated. The excitation light path and weight of each step were saved to the database, after which a new photon packet simulation was started from step 1.

The emission light path simulation was similar to the excitation light path simulation. Specifically, we need to first determine the initial position, the initial direction, and the initial weight

before launching an emission photon packet (**Figure S3**, right panel c-d). The initial coordinates of each emission photon packet were randomly selected from the excitation light path database. All coordinates in the database had an equal probability to be selected regardless of excitation light path. If the selected coordinates were within an area containing fluorophore, its initial coordinates were determined first, and then the corresponding excitation light path history (from the start to the point where the emission occurred) was recorded. In this study, we assumed the fluorophore existed equally within a 1 mm diameter sphere of viral expression area centered 0.3 mm below the fiber tip.

The initial direction of an emission photon was assumed to have isotropic probability in all directions; therefore, the direction cosines can be derived using the following:

$$v_x = \sin(\pi\xi_1)\cos(2\pi\xi_2)$$

$$v_y = \sin(\pi\xi_1)\sin(2\pi\xi_2)$$

$$v_z = \cos(\pi\xi_1) \quad (12)$$

Lastly, the initial weights were inherited from the remaining weights of the excitation photon packet at the initial coordinates.

Steps 2 and 3 were repeated until the weight of the photon packet reached 10^{-4} or less, and then the simulation of this photon packet was terminated (step 4). In emission step 4, only when the photon packet reached the fiber tip at smaller than 1/2 acceptance angle and a weight beyond 10^{-4}, the paired excitation/emission light path and the weight of each step were saved to the database. In order to improve signal-to-noise ratio, we collected 2-2.5 $\times$ 10^4 pairs of excitation and emission light paths.

The final weight (W_{final}) when the emission photon reaching the optical fiber tip represents the survival rate of the current combined excitation/emission light path. Therefore, the total average

pathlength of excitation and emission lights are then calculated by summing each survived photon's W_{final} multiplied by its paired excitation and emission pathlength respectively:

$$\bar{X}_{ex}(\lambda_{em}) = \sum_{n=1}^{N} X_{ex}(n) \cdot e^{-\mu_a(\lambda_{ex})\cdot X_{ex}(n)} \cdot e^{-\mu_a(\lambda_{em})\cdot X_{em}(n)} = \sum_{n=1}^{N} X_{ex}(n) \cdot W_{final}$$

$$\bar{X}_{em}(\lambda_{em}) = \sum_{n=1}^{N} X_{em}(n) \cdot e^{-\mu_a(\lambda_{ex})\cdot X_{ex}(n)} \cdot e^{-\mu_a(\lambda_{em})\cdot X_{em}(n)} = \sum_{n=1}^{N} X_{em}(n) \cdot W_{final} \quad (13)$$

Since the W_{final} is affected during both excitation and emission phase, the emission measured at different wavelengths have not only distinct average emission pathlength ($\bar{X}_{em}(\lambda_{em})$), but also distinct average excitation pathlength ($\bar{X}_{ex}(\lambda_{em})$) even when these emission wavelengths are excited by the same excitation wavelength. In this study, only the 488 nm excitation wavelength was used and simulated.

To plot the 488 nm excitation light illuminating distribution (Figure S 3a), all excitation light paths' coordinates generated from the excitation light path simulation, regardless to the emission light detection, were first compressed into 2D coordinates, and then used for the 2D histogram. To plot the 515 or 580 nm emission light receptive probability map (Figure S 3b-c), the initial emission 3D coordinate of each successfully detected 515 or 580 emission photons were compressed into 2D coordinates and shown in a 2D histogram.

Correction of Hb-absorption

Given the different absorption of HbO and HbR (**Figure S1**), their dynamic concentration changes must be quantified in order to properly correct fluorescent sensor signals. To address this, we proposed the following methods to derive HbO and HbR concentration (ΔC_{HbO} and ΔC_{HbR}) time-courses using spectral datapoints.

In a simple, non-absorbing and non-scattering medium, the measured fluorescence signal *F* at any time *t* is linearly related to the fluorescent protein concentration $C(t)$:

$$\frac{F(t)}{F(t_0)} = \frac{C(t)}{C(t_0)} \tag{14}$$

where $F(t_0)$ and $C(t_0)$ represent the fluorescence signal and the fluorescent protein concentration at the reference time point *0*, respectively. When the absorption of the medium is considered, and *F* is measured at multiple wavelengths λ_{Em}, equation (14) can be further modified according to an established model (Ma et al., 2016):

$$\frac{F(t,\lambda_{Em})}{F(t_0,\lambda_{Em})} = e^{-[\Delta\mu_a(t,\lambda_{Ex})X(\lambda_{Ex})+\Delta\mu_a(t,\lambda_{Em})X(\lambda_{Em})]} \cdot \frac{C(t)}{C(t_0)} \tag{1}$$

Then after natural logarithmic transformation:

$$\ln\left(\frac{F(t,\lambda_{Em})}{F(t_0,\lambda_{Em})}\right) = -[\Delta\mu_a(t,\lambda_{Ex})X(\lambda_{Ex}) + \Delta\mu_a(t,\lambda_{Em})X(\lambda_{Em})] + \ln\frac{C(t)}{C(t_0)} \tag{15}$$

where $\Delta\mu_a(t,\lambda_{Ex})$ represents the change of the absorption coefficient μ_a at excitation wavelength λ_{Ex} at the time point t compared to the time point *0*; $\Delta\mu_a(t,\lambda_{Em})$ represents the change of the absorption coefficient μ_a at emission wavelength λ_{Em} at the time point t compared to the time point *0*; $X(\lambda_{Ex})$ and $X(\lambda_{Em})$ represent the photon traveling pathlengths at the given wavelength, respectively. Next, HbO and HbR concentration changes (ΔC_{HbO} and ΔC_{HbR}) as a function of time need to be incorporated. When using 488 nm excitation, the absorption term in equation (15) that contains $\Delta\mu_a$ could be expressed as:

$$\begin{aligned}
&\Delta\mu_\alpha(t,\lambda_{Ex})X(\lambda_{Ex}) + \Delta\mu_\alpha(t,\lambda_{Em})X(\lambda_{Em}) \\
&= \Delta\mu_\alpha(t,488\,nm)X(488\,nm) + \Delta\mu_\alpha(t,\lambda_{Em})X(\lambda_{Em}) \\
&\approx [\xi_{HbO}(488\,nm)\,\Delta\,C_{HbO}(t) + \xi_{HbR}(488\,nm)\,\Delta\,C_{HbR}(t)]X(488\,nm) \\
&\quad + [\xi_{HbO}(\lambda_{Em})\,\Delta\,C_{HbO}(t) + \xi_{HbR}(\lambda_{Em})\,\Delta\,C_{HbR}(t)]X(\lambda_{Em}) \\
&= \Delta\,C_{HbO}(t)[\xi_{HbO}(488\,nm)X(488\,nm) + \xi_{HbO}(\lambda_{Em})X(\lambda_{Em})] + \\
&\quad \Delta\,C_{HbR}(t)[\xi_{HbR}(488\,nm)X(488\,nm) + \xi_{HbR}(\lambda_{Em})X(\lambda_{Em})]
\end{aligned} \tag{16}$$

where ξ_{HbO} and ξ_{HbR} are well-established molar extinction coefficients at different wavelengths of HbO and HbR, respectively (Prahl, 1999).

At the time point *t*, the measured fluorescence ratio after natural logarithmic transformation, ranged from λ_{Em_1} to λ_{Em_n} could be put together in a vector form $M(t)$:

$$\mathrm{M}(t) = \begin{bmatrix} ln\left(\frac{F(t,\lambda_{Em_1})}{F(0,\lambda_{Em_1})}\right) \\ \vdots \\ ln\left(\frac{F(t,\lambda_{Em_n})}{F(0,\lambda_{Em_n})}\right) \end{bmatrix} \tag{17}$$

Additionally, two vectors A and B could be used to represent the following:

$$A = \xi_{HbO}(488nm) \cdot X(488nm) + \begin{bmatrix} \xi_{HbO}(\lambda_{Em_1}) \cdot X(\lambda_{Em_1}) \\ \vdots \\ \xi_{HbO}(\lambda_{Em_n}) \cdot X(\lambda_{Em_n}) \end{bmatrix} \tag{18}$$

$$B = \xi_{HbR}(488nm) \cdot X(488nm) + \begin{bmatrix} \xi_{HbR}(\lambda_{Em_1}) \cdot X(\lambda_{Em_1}) \\ \vdots \\ \xi_{HbR}(\lambda_{Em_n}) \cdot X(\lambda_{Em_n}) \end{bmatrix} \tag{19}$$

With any activity-independent fluorescence signals, the last component $\ln\frac{C(t)}{C(t_0)}$ should be 0. Practically, we designate an error value σ. Taken together, equation (15) could then be simplified and reorganized as equation (20). To solve $\Delta C_{HbO}(t)$ and $\Delta C_{HbR}(t)$ at any time point t, we used generalized method of moment (GMM)(Hansen, 1982) to minimize L in equation (21). By performing the GMM computation for each time point, we can obtain time-courses of $\Delta C_{HbO}(t)$, $\Delta C_{HbR}(t)$ and σ.

$$M(t) + \Delta C_{HbO}(t) \cdot A + \Delta C_{HbR}(t) \cdot B - \sigma = 0 \tag{20}$$

$$\mathrm{L} = \sum_{i=1}^{n} (M(t)_i + \Delta C_{HbO}(t) \cdot A_i + \Delta C_{HbR}(t) \cdot B_i - \sigma)^2 \tag{21}$$

In this case, we have numerous spectral datapoints that can be used to resolve two unknowns that are of interest – $\Delta C_{HbO}(t)$and $\Delta C_{HbR}(t)$. After which, $\Delta\mu_\alpha(t,\lambda_{\mathrm{Ex}})$ and $\Delta\mu_\alpha(t,\lambda_{\mathrm{Em}})$ can be calculated using equation (16) and $F(t,\lambda_{Em})$ can be subsequently calculated using equation (15) to correct for HbO and HbR absorptions.

Subject

This study employed a total of 26 male Sprague Dawley (SD) rats weighing between 300-600g. All procedures were performed in accordance with the National Institutes of Health Guidelines for Animal Research (Guide for the Care and Use of Laboratory Animals) and approved by the University of North Carolina (UNC) Institutional Animal Care and Use Committee. These rats were separated into 6 cohorts. In the first cohort (n=3), EYFP was expressed in the bilateral S1FL using AAV5-CaMKIIα-EYFP (titer 4.2×10^{12} molecules/mL, UNC Vector Core) to demonstrate the impact of Hb concentration changes on activity-independent fluorescence signals and evaluate the proposed correction method. In the second cohort (n=4), GCaMP and tdTomato were co-expressed in the bilateral S1FL using a mixture of AAV9-CaMKIIα-GCaMP6f-WPRE-SV40 (titer $\geq 1 \times 10^{13}$ vg/mL, Penn Vector Core) and AAV9-CAG-tdTomato (titer 3.8×10^{12} molecules/mL, UNC Vector Core) at 5:1 ratio to demonstrate the impact of Hb concentration changes on a commonly used fluorescent sensor and evaluate the proposed correction method. In the third cohort (n=3), GCaMP and tdTomato were co-expressed in the left PrL using a viral mixture identical to the second cohort. The fourth cohort (n=4) received a twisted tungsten electrode implanted into the M1, and GCaMP and tdTomato were co-expressed in the contralateral M1 using a viral mixture identical to the second cohort. The fifth cohort (n=5) was used in a supplementary study of isoflurane challenge, and only had GCaMP expressed in the left M1. The sixth cohort (n=4) received a twisted tungsten electrode implanted into the M1, and GCaMP and tdTomato were co-expressed in the contralateral M1 and ipsilateral striatum using a viral mixture identical to the second cohort. The seventh cohort (n=3) was used in a supplementary study, and had channelrhodopsin2 (ChR_2) expressed in the ventroposterior thalamus (VP) using AAV9-CaMKIIα-ChR2-EYFP (titer 3.6×10^{12} molecules/mL, UNC Vector Core) and GCaMP expressed in the ipsilateral S1 using AAV9-CaMKII-GCaMP6f-WPRE-SV40 (titer $\geq 1 \times 10^{13}$ vg/mL, Penn Vector Core). All rats in this study were housed under environmentally-

controlled conditions (12 h normal light/dark cycles, lights on at 7am; 20–23 °C and 40–60% relative humidity), with ad libitum access to food and water.

Stereotactic surgery

For all surgical procedures, rats were anesthetized initially by 5% isoflurane, and maintained by a constant flow of 2-3% isoflurane mixed with medical air. Rectal temperature was continuously monitored and maintained within 37 ± 0.5 °C using a feedback-controlled heating pad (Harvard Apparatus, Model 557020, Holliston, MA). Rats were head-fixed to a stereotactic frame (Kopf Instruments, Model 962, Tujunga, CA). The skin was opened to expose the skull surface, and burr holes were prepared according to experimental coordinates. All coordinates used for microinjection are listed as follows. S1: AP = +0.5 mm and ML = +3.7 mm, DV = 1.3 mm, M1: AP = +1.8 mm and ML = -2.5 mm, DV = 2.0 mm, Striatum: AP = 0.5 mm and ML = 4.0 mm, DV = 5.2 mm, VP: AP = -2.8 mm and ML = +2.5 mm, DV = 6.5 mm, PrL: AP = 2.2 mm and ML = 0.9 mm, DV = 4.1 mm. Microinjections were performed at a flow rate of 0.1 µL/min for 1 µL, and an additional 10 min was given for virus diffusion prior to slow retraction of the microsyringe needle. The burr holes were then sealed with bone wax (Fisher Scientific, Pittsburgh, PA), and the wound was sutured. A month after the virus microinjection, the skin was reopened to expose the skull, then the bone wax was removed and optical fibers (200 µm in diameter; NA: 0.39) were chronically implanted to coordinates 0.2-0.5 mm above the virus injection sites. Four MR-compatible miniature brass screws (Item #94070A031, McMaster Carr, Atlanta, GA) were anchored to the skull, then the surface of the skull was covered with dental cement to seal implanted components and the wound was sutured to further protect the surgical site.

At the end of every surgical procedure, lidocaine jelly (#866096, Henry Schein Inc., Melville, NY) was applied around the surgical wound for pain relief, and to prevent the rat scratching the wound. Meloxicam (#6451720670, Henry Schein Inc., Melville, NY) was also given by oral administration for

further pain relief. Rats were allowed at least 1 week for recovery from surgical procedures before any further experiments.

Experimental setup

The spectrally resolved fiber-photometry system in this study replicates an established system described previously(Meng et al., 2018). Laser beams from a 488 nm 60 mW continuous wave (CW) laser (OBIS 488 LS-60, Coherent, Santa Clara, CA) and a 561 nm 50 mW CW laser (OBIS 561 LS-50, Coherent, Inc.) are aligned and combined by broadband dielectric mirrors (BB1-E02, Thorlabs, Newton, NJ) and a long-pass dichroic mirror (ZT488rdc, Chroma Technology Corp), then launched into a fluorescence cube (DFM1, Thorlabs, Newton, NJ). Extra neutral density filters (NEK01, Thorlabs, Newton, NJ) are placed between the combined laser beam and the fluorescence cube to adjust the final laser power. The fluorescence cube contains a dichroic mirror (ZT488/561rpc, Chroma Technology Corp) to reflect and launch the combined laser beam through an achromatic fiber port (PAFA-X-4-A, Thorlabs, Newton, NJ) into the core of a 105/125 mm core/cladding multi-mode optical fiber patch cable (FG105UCA, Thorlabs, Newton, NJ). The distal end of the patch cable is connected to an implantable optical fiber probe for both excitation laser delivery and emission fluorescence collection. The emission fluorescence collected from the fiber travels back along the patch cable into the fluorescence cube, passes through the dichroic mirror and an emission filter (ZET488/561 m, Chroma Technology Corp, Bellows Falls, VT), then launches through an aspheric fiber port (PAF-SMA-11-A, Thorlabs, Newton, NJ) into the core of an AR-coated 200/230 mm core/cladding multi-mode patch cable (M200L02S-A, Thorlabs, Newton, NJ). The AR-coated multi-mode patch cable is connected to a spectrometer (QE Pro-FL, Ocean Optics, Largo, FL) for spectral data acquisition, which can be operated by a UI software OceanView (Ocean Optics, Largo, FL). In order to achieve concurrent recording during fMRI, trigger mode is used in OceanView, where the photometry system is synchronized with MRI using an Arduino micro-controller board.

The stimulation system uses a DAQ board (1208Hs-2AO, Measurement Computing Corp., Norton, MA) to send out stimulus triggers according to the stimulus paradigm set in a homemade software program. During fMRI experiments, the DAQ synchronizes stimulation pulses via triggers from the MRI system. Stimulation pulses were driven by a constant current stimulus isolator (A385RC, World Precision Instruments, Sarasota, FL) for forepaw and microelectrical stimulation experiments; and by a 473 nm blue diode laser (Shang Laser and Optics Century, BL473T8-200FC + ADR-800A, Shanghai, China) for optogenetic experiments.

Animal subject preparation and physiology management

Rats were initially anesthetized with 4% isoflurane (Vaporizer #911103, VetEquip Inc., Livermore, CA, USA) mixed with medical air and endotracheally intubated using a 14G x 2"(>400 g) or 16G x 2"(<400 g) i.v. catheter (Surflash Polyurethane Catheter, TERUMO, Somerset, NJ, USA). Respiration was maintained by a ventilator (SAR-830 or MRI-1, CWE Inc, Ardmore, PA, USA) set at 60 breaths/min and an inspiration time ratio of 40%. A rectal probe was used to monitor core body temperature (OAKTON Temp9500, Cole-Parmer, Vernon Hills, IL, USA) and a capnometer was used to monitor heart rate, peripheral blood oxygen saturation, and end-tidal CO_2 (SURGIVET® V90041LF, Smith Medical, Dublin, OH, USA). Body temperature was maintained at 37 ± 0.5°C using a circulating water blanket connected to a temperature adjustable water bath (Haake S13, Thermo Fisher Scientific, Waltham, MA, USA). Ventilation tidal volume was adjusted to keep the heart rate at 300 ± 50 beats per minute, peripheral blood oxygen saturation above 90%, and end-tidal CO_2 between 2.8 - 3.2%. End-tidal CO_2 values from this capnometer system were previously calibrated against invasive sampling of arterial blood gas, reflecting a partial pressure of carbon dioxide (pCO_2) level of 30–40 mm Hg(Shih et al., 2012, 2013). For studies using Rhodamine B for CBV measurements, a bolus dose of 40 mg/kg (Sigma–Aldrich, St. Louis, MO) was injected via tail vein.

Concurrent functional MRI Scan with fiber-photometry recording

All fMRI data in this study were collected on a Bruker BioSpec 9.4-Tesla, 30 cm bore system with 6.0.1 on an AVANCE II console (Bruker BioSpin Corp., Billerica, MA). An RRI BFG 150/90 gradient insert (Resonance Research, Inc, Billerica, MA) paired with a Copley C700 gradient amplifier (Copley Controls Corp., Canton, MA) was used. A homemade single-loop surface coil with an internal diameter of 1.6 cm was used as a radio-frequency transceiver. Isoflurane concentrations were adjusted to 2% and animals were secured in to a custom-built, MR-compatible rat cradle. Animal physiology was monitored and maintained as described in the previous paragraph.

Upon stabilizing the animals, a pair of needle electrodes was inserted under the skin of forepaw for stimulation, or electrode/optical fiber patch cables were connected according to experimental design. Before connecting the fiber-photometry patch cable, all light in the room was turned off, the final output power of the 488 nm laser and 561 nm laser were 51.3 ± 18.6 μW (mean ± SD, n = 26), which were adjusted to balance spectral amplitudes (Meng et al., 2018). 100 μW power is the maximum we suggested when the virus expression is less robust. This power range is consistent with published fiber-photometry studies (Gunaydin et al., 2014; Jones-Tabah et al., 2021, p.; Liang et al., 2017; Zhang et al., 2021). A background spectrum was measured as a reference by pointing the fiber tip to a nonreflective background in the dark room. This background spectrum was then automatically subtracted by OceanView during photometry recording.

Following setup processes, the cradle was pushed into MRI bore, and a bolus of dexmedetomidine (0.025 mg/kg; Dexdormitor, Orion, Espoo, Finland) cocktailed with paralytic agent rocuronium bromide (4.5 mg/kg; Sigma–Aldrich, St. Louis, MO) was injected into the tail vein (Chao et al., 2018). Fifteen minutes after the bolus injection, continuous intravenous infusion of dexmedetomidine (0.05 mg/kg/h) and rocuronium bromide (9 mg/kg/h) cocktail was initiated and the isoflurane concentration was adjusted to 0.5–1% for the entire scanning period.

Magnetic field homogeneity was optimized first by global shim and followed by local first- and second-order shims according to B0 map. Anatomical images for referencing were acquired using a rapid acquisition with relaxation enhancement (RARE) sequence (12 coronal slices, thickness = 1 mm, repetition time (TR) = 2500 ms, echo time (TE) = 33 ms, matrix size = 256 × 256, field-of-view (FOV) = 25.6 × 25.6 mm^2, in plane resolution 0.1 x 0.1 mm, average = 8, RARE factor = 8). The center of the 5^{th} slice from the anterior direction was aligned with the anterior commissure. Cerebral blood volume (CBV) fMRI scans were acquired using a multi-slice single-shot gradient echo echo-planar imaging sequence (GE-EPI) (slice thickness = 1 mm, TR = 1000 ms, TE = 8.1 ms, matrix size = 80 × 80, FOV = 25.6 × 25.6 mm^2, in plane resolution 0.32 x 0.32 mm, bandwidth = 250 kHz), with the same image slice geometry imported from the previously acquired T2-weighted anatomical image. A session of GE-EPI scans with 300 repetitions was taken, and at about the 100^{th} scan, Feraheme (30 mg Fe/kg, i.v.) was administered for CBV percentage change calculations.

CBV fMRI Data Processing and Statistical Analyses

All fMRI data were analyzed using the Analysis of Functional Neuroimages (AFNI)(Cox, 1996) general linear model (GLM) framework(Worsley and Friston, 1995). All EPI images were skull-stripped, and slice-timing was corrected. Then automatic co-registration was applied to realign time-courses within subjects to correct subtle drift of EPI images. Finally all EPI images were aligned to a T2-weighted rat brain template(Valdés-Hernández et al., 2011) to generate normalized fMRI images to allow for group-level comparisons. Gaussian smooth (FWHM = 0.5 mm) was performed before feeding into the GLM fitting. To test the group-level significant consistency of the stimulus-evoked responses, we employed a parametric one-sample t-test implemented in AFNI. The false discovery rate correction was used to adjust for the multiple comparisons of fMRI maps ($p < 0.05$). A 3x3 voxel region of interest (ROI) was placed at the fiber tip in the S1 to extract fMRI time-course data. To account for Feraheme kinetics

over the course of experiments, the following equations were used to calculate the $\Delta R_2^*(baseline)$, $\Delta R_2^*(stim)$, and ΔCBV (Decot et al., 2017).

$$\Delta R_2^*(baseline) = -\frac{1}{TE}\ln\left(\frac{S_{prestim}}{S_0}\right) \quad (22)$$

$$\Delta R_2^*(stim) = -\frac{1}{TE}\ln\left(\frac{S_{stim}}{S_{prestim}}\right) \quad (23)$$

$$\Delta CBV = \frac{\Delta R_2^*(stim)}{\Delta R_2^*(baseline)} \quad (24)$$

where $S_{prestim}$ and S_0 represents MR signal intensity after and before Feraheme injection, respectively, and S_{stim} are the MR signal intensities during the stimulation.

Fiber-photometry Spectral unmixing

Mixed spectra acquired by fiber-photometry were analyzed using a spectral linear unmixing algorithm(Meng et al., 2018). Briefly, at any time point n, the mixed spectrum $Y(n)$ was modeled as:

$$Y(n) = Coff_1(n) \times S_1 + Coff_2(n) \times S_2 + C + \varepsilon(n) \quad (25)$$

where S_1 and S_2 are the normalized reference emission spectra of the two fluorescence signal sources. $Coff_1$ and $Coff_2$ are the unknown regression coefficients corresponding to the S_1 and S_2 respectively. C is the unknown constant, and $\varepsilon(n)$ is random error. $Coff_1(n)$, $Coff_2(n)$, and $\varepsilon(n)$ at each time point were estimated using the lm() function in the RStudio package (RStudio Inc. V1.0.136, Boston, MA).

Modeling the hemodynamic response function

The relationship between neuronal activity and hemodynamic response can be expressed as:

$$HbT(T) = N(T)Ä\, HRF(t) + c + d(T) \quad (26)$$

where the $HbT(T)$ represents hemoglobin fluctuation time-course, the $N(T)$ represents neuronal activity time-course, the $HRF(t)$ represents an impulse hemodynamic response function with t

sampling points, c is a constant for baseline offset and $d(T)$ is for linear drift over time. Assuming $T = \{0, 1, 2, \dots, m\}, t = \{0, 1, 2, \dots, n\}$,this equation can be expressed as:

$$\begin{bmatrix} HbT(0) \\ HbT(1) \\ HbT(2) \\ \vdots \\ HbT(m) \end{bmatrix} = \begin{bmatrix} N(0) & 0 & 0 & & 0 & 1 & 0 \\ N(1) & N(0) & 0 & \cdots & 0 & 1 & \frac{1}{m} \\ N(2) & N(1) & N(0) & & 0 & 1 & \frac{2}{m} \\ & \vdots & & \ddots & & \vdots & \\ N(m) & N(m-1) & N(m-2) & \cdots & N(m-n) & 1 & 1 \end{bmatrix} \times \begin{bmatrix} HRF(0) \\ HRF(1) \\ HRF(2) \\ \vdots \\ HRF(n) \\ c \\ D \end{bmatrix} \quad (27)$$

Therefore, the $HRF(t)$, c and D (slope of $d(T)$) can be solved using Ordinary Least Squares solution with known $HbT(T)$ and $N(T)$.

To avoid physiological noise contamination, $HbT(T)$ were low-pass filtered with a cutoff frequency at 0.5 Hz before the HRF estimation.

Histology

At the end of the experiments, rats were euthanized by a mixture of 1-2 ml of sodium pentobarbital and phenytoin sodium (Euthasol, Virbac AH, Inc., Westlake, TX), and transcardially perfused with saline followed by 10% formalin. The brains were removed and stored in 10% formalin overnight, then transferred into a 30% sucrose solution (in 0.1 M phosphate buffer) for 2–3 days, until brains sunk to bottom of storage bottles. These brains were cut into serial coronal sections (40 μm) using a cryotome (#HM450, Thermo Fisher Scientific, Waltham, MA) and mounted on glass slides. Fluoro-Gel II Mounting Medium (#17985-50, Electron Microscopy Sciences, Hatfield, PA) was covered on the brain slides to provide DAPI stain and for fluorescence imaging. Slides were imaged using a Zeiss LSM780 confocal microscope.

Table S1: Average pathlengths $X(\lambda_{Ex})$ and $X(\lambda_{Em})$ by Monte Carlo Simulation.

Emission wavelength (nm)	Average $X(\lambda_{Ex})$ (cm)	Average $X(\lambda_{Em})$ (cm)
488	0.045093573	0.044381928
489	0.046031195	0.045206893
490	0.045353095	0.044599308
491	0.045145851	0.043833332
492	0.044940114	0.044644849
493	0.045780127	0.044951492
494	0.044833187	0.044238425
495	0.045254011	0.044087712
496	0.044832712	0.04357339
497	0.045793623	0.04438636
498	0.044556411	0.043741701
499	0.046485322	0.045282627
500	0.044936862	0.045399841
501	0.044904189	0.043737664
502	0.044676525	0.044692953
503	0.046449058	0.045104426
504	0.04554069	0.045690015
505	0.044186305	0.042754367
506	0.044463103	0.043549104
507	0.045240076	0.04375625
508	0.045271499	0.043551134
509	0.045203535	0.044181218
510	0.04544563	0.04325581
511	0.045264121	0.043061521
512	0.044537346	0.042787669
513	0.044684362	0.042203088
514	0.044171835	0.041233961
515	0.044738093	0.04226692
516	0.044465855	0.041780618
517	0.044712008	0.041028167
518	0.043706904	0.039055061
519	0.045479041	0.040324911
520	0.04389417	0.039274782
521	0.043549373	0.038231377
522	0.043219292	0.037524461
523	0.043155712	0.037460255
524	0.042766927	0.03694169
525	0.043084675	0.035815527
526	0.043150433	0.034397857
527	0.043739313	0.034308684
528	0.04204147	0.033144384
529	0.042283369	0.033431559
530	0.041576273	0.03274051
531	0.041403969	0.032249133
532	0.042259357	0.03207917

533	0.042053695	0.03107138
534	0.041557514	0.03060531
535	0.041085208	0.030560256
536	0.040797064	0.03006389
537	0.041257322	0.030668237
538	0.040610296	0.030040682
539	0.041278057	0.029169312
540	0.040911226	0.029855726
541	0.040595945	0.02918373
542	0.042377485	0.029198135
543	0.039844855	0.028926177
544	0.040222405	0.029041564
545	0.040557664	0.02896974
546	0.040948557	0.029918984
547	0.041229136	0.02972593
548	0.042018793	0.029700507
549	0.040926872	0.029586768
550	0.040638456	0.030291714
551	0.041457873	0.030528575
552	0.042017	0.030977213
553	0.041651907	0.03110746
554	0.041411748	0.031308639
555	0.043001153	0.031844072
556	0.041683419	0.031503805
557	0.041847941	0.031712862
558	0.042180993	0.031085786
559	0.042966746	0.031697395
560	0.041901694	0.032766419
561	0.041052921	0.032209208
562	0.042547549	0.032859811
563	0.043019746	0.031171994
564	0.042869082	0.031870075
565	0.04259555	0.031539041
566	0.042495922	0.031772912
567	0.041849738	0.03096196
568	0.042757629	0.031304522
569	0.042385588	0.031173599
570	0.040329248	0.029757283
571	0.041741617	0.029138568
572	0.041959	0.02928782
573	0.040394795	0.028463193
574	0.042377246	0.028834891
575	0.042868462	0.029326084
576	0.041217724	0.028643115
577	0.040870023	0.028252116
578	0.04152183	0.028335837
579	0.042072267	0.028919726
580	0.041743821	0.029298395

581	0.041806895	0.029681861
582	0.040685735	0.030320858
583	0.043016536	0.030965203
584	0.042402937	0.031996206
585	0.04392674	0.032806366
586	0.044501271	0.035278456
587	0.04229412	0.035422192
588	0.044236652	0.037092348
589	0.04453953	0.039432637
590	0.045403689	0.042120811
591	0.045720725	0.043050508
592	0.046721386	0.044569175
593	0.04658936	0.046035872
594	0.046856197	0.046439476
595	0.046639376	0.050515218
596	0.047224996	0.050214893
597	0.047826425	0.051104707
598	0.047684723	0.055223016
599	0.048337422	0.058213776
600	0.048084498	0.05737416
601	0.048056722	0.055091687
602	0.04834153	0.058816123
603	0.047162448	0.060133037
604	0.048829402	0.059604177
605	0.048451209	0.06028036
606	0.049314163	0.062367752
607	0.04864508	0.064056712
608	0.047748293	0.064284482
609	0.049373015	0.062747999
610	0.049654837	0.062923108
611	0.04873937	0.059863284
612	0.048195016	0.067000662
613	0.049368953	0.06636147
614	0.049471526	0.066356177
615	0.0509815	0.065962632
616	0.048364103	0.067198216
617	0.049258066	0.068526301
618	0.047925207	0.066248105
619	0.047651389	0.064842825
620	0.049918572	0.069186304
621	0.048079999	0.06930868
622	0.049001919	0.067431619
623	0.047876525	0.068410691
624	0.048913258	0.066037747
625	0.049283261	0.069188854
626	0.049833981	0.06884971
627	0.048520845	0.068593605
628	0.050626431	0.072924701

629	0.049001529	0.069368645
630	0.049823194	0.065875529
631	0.049922336	0.070392798
632	0.049238223	0.064130262
633	0.049091246	0.068703876
634	0.049004327	0.069478775
635	0.050113703	0.069644791
636	0.04935265	0.071714894
637	0.048524722	0.065578319
638	0.049033574	0.068908878
639	0.049706978	0.07082453
640	0.048870373	0.067637064
641	0.049378341	0.070513241
642	0.047531488	0.065338289
643	0.049938511	0.067545633
644	0.048420131	0.070092771
645	0.048394814	0.066225652
646	0.049045058	0.067036677
647	0.0471389	0.063334021
648	0.048276563	0.064587084
649	0.049566595	0.067005786
650	0.048757214	0.066615875
651	0.048086512	0.064861617
652	0.049770716	0.071548828
653	0.048497445	0.065184075
654	0.051019438	0.064323894
655	0.047818361	0.069356187
656	0.047395308	0.06791304
657	0.048211057	0.064465262
658	0.04925706	0.068522353
659	0.049243152	0.067570369
660	0.049306566	0.068635881
661	0.048296998	0.064357191
662	0.04946561	0.069889086
663	0.048651964	0.066769534
664	0.049580237	0.061861251
665	0.047312599	0.061431122
666	0.048177763	0.066106882
667	0.049260615	0.06726634
668	0.050070504	0.065101662
669	0.049296071	0.060405176
670	0.049355936	0.066502011
671	0.048166386	0.06328206
672	0.048552887	0.063599076
673	0.047215508	0.0630013
674	0.050010272	0.065692928
675	0.048251383	0.059550299
676	0.049073229	0.064339078

677	0.049158252	0.066160593
678	0.048586706	0.063461555
679	0.049408432	0.066435927
680	0.048615398	0.063448449
681	0.048136575	0.06465852
682	0.049240503	0.065996535
683	0.048443426	0.068781814
684	0.049338138	0.064378941
685	0.048442599	0.067303664
686	0.047661626	0.060606162
687	0.048758079	0.06567617
688	0.048292359	0.062784951
689	0.048590671	0.064714098
690	0.049590564	0.062694093
691	0.047962726	0.063263871
692	0.050139198	0.061484326
693	0.048513909	0.063766816
694	0.048005757	0.062790064
695	0.048824793	0.06817339
696	0.048301867	0.062689082
697	0.048157362	0.065482695
698	0.047640732	0.059392198
699	0.048021823	0.062982676
700	0.049106955	0.063966326

Figure legends

Figure 1. Spectrally resolved fiber-photometry system and Hb-absorption effects.

(**A**) Schematic illustration of a spectrally resolved fiber-photometry system used for recording fluorescence signals.

(**B**) Hb in the red blood cells absorb light in two phases: the excitation light from the optical fiber (left) and the emission light to be recorded by the optical fiber (right). Color density of arrowheads delineates light intensity. Increase in Hb is expected to decrease the number of photons in both phases.

(**C**) Simulated average excitation and emission photon traveling pathlengths across 488 – 700 nm emission wavelengths from our database of paired excitation/emission light paths.

(**D**) Impact of HBO and HBR concentration on ΔF/F. Simulated effects of HbO and HbR concentration changes on fluorescence signal measurement. ΔC_{Hb0} and ΔC_{HbR} ranging from -90 to +90 μM were used to simulate fluorescence signal changes (ΔF/F) between 500 to 700 nm using the molar extinction coefficients of HbO and HbR in **Figure S1** and simulated light paths in **Figure 1C**. Graphs shaded in blue indicate an overall decrease in total Hb (HbT); whereas graphs shaded in red indicate an overall increase in HbT.

See additional details in Figure S1-S4, Supplementary Video 1, and Table S1.

Figure 2. In vivo quantification of HbO and HbR changes using EYFP emission in fiber-photometry and correction of EYFP signals for Hb-absorption.

(**A**) Preparation for fiber-photometry measurement of EYFP signals in the S1 of the forelimb region.

(**B**) Confocal image showing EYFP expression.

(**C**) Simultaneous dual-spectral photometry recording of EYFP signals and hemodynamic responses (CBV) was achieved by intravenously injecting a long-circulating red fluorescent dye, Rhodamine B.

(**D-J**) Peri-stimulus heatmaps showing repeated trials and average response time-courses of the changes in measured rhoCBV, measured EYFP, derived HbO, derived HbR, corrected rhoCBV, corrected EYFP, and

derived HbT, respectively. The gray-shaded segment indicates forepaw-stimulation period. Note that Hb-absorption induce a pseudo-negative changes in measured EYFP signals during stimulation.

(**K,L**) Correction of the contaminated EYFP and rhoCBV signals, respectively, across 5 subjects and 30 trials (***$p < 0.001$, paired *t*-test). Measured and corrected EYFP signals are compared. Measured rhoCBV was normalized to 0 to show the difference before and after the correction. All color bars use the same unit as the time-course Y axis. Error bars represent standard deviation.

See also Figure S6-S8.

Figure 3. In vivo quantification of HbO and HbR changes using tdTomato emission in fiber-photometry and correction of GCaMP signals for Hb-absorption.

(**A**) Preparation for fiber-photometry measurement of GCaMP and tdTomato signals in the S1 of the forelimb region.

(**B**) Confocal images showing GCaMP and tdTomato expression.

(**C**) GCaMP and tdTomato emission spectra from 488 nm excitation.

(**D**) Concurrent CBV measurement was achieved by MRI and intravenous injection of the long-circulating iron oxide nanoparticles, Feraheme. Insert shows a forepaw-induced group-level fMRI activation map (corrected $p < 0.05$, $n = 5$).

(**E-L**) Peri-stimulus heatmaps showing repeated trials and average response time-courses of the changes in measured GCaMP, measured tdTomato, derived HbO, derived HbR, derived HbT, corrected GCaMP, corrected tdTomato, and measured MRI-CBV, respectively. The gray-shaded segment indicates the forepaw-stimulation period.

(**M**) Two-dimensional histogram summarizing HbT and MRI-CBV changes across 5 subjects and 27 trials. The color bar indicates counts on the log scale.

(**N**) Photometry derived HbT exhibited higher sensitivity than MRI-CBV (***$p < 0.001$, paired *t*-test).

(**O**) Trial-level cross-correlation between the Z scores of the derived HbT and the Z scores of the MRI-CBV over the peri-stimulus time period of 10 s, and

(**P**) scatter plots showing cross-correlation coefficients (left) and time lag (right) of all trials.

(**Q, R**) Correction of pseudo-undershoot artifacts in GCaMP time-courses of **(Q)** short (1 s), and **(R)** long (10 s) stimulations, respectively ((***$p < 0.001$, paired *t*-test).

See also Figure S9-S10.

Figure 4. Hb-absorption effects on sustained GCaMP signal measurement using fiber-photometry

(A) Preparation for fiber-photometry measurement of GCaMP and tdTomato signals in the PrL region.

(B) Measured and corrected tdTomato time-courses before and after ethanol administration. The same volume of saline was administered in a separate session to generate within-subject vehicle control data.

(C) Measured and corrected tdTomato signals were sampled and displayed at 5 min. A significant effect was found between the three groups and *post-hoc* test showed a significant difference between the measured and corrected signals. ***$p < 0.001$, two-way ANOVA (n=3).

(D) Derived HbO, HbR, and HbT time-courses before and after the ethanol administration. Higher HbT z-scores were attributed to the lower baseline variation following the addition of HbO and HbR.

(E) Measured and corrected GCaMP time-courses before and after the ethanol administration. The same volume of saline was administered in a separate session to generate within-subject vehicle control data. Data were collected concurrently with those shown in (B).

(F) Measured and corrected GCaMP signals were sampled and displayed at 5 min intervals. A significant effect was found between the three groups and *post-hoc* test showed a significant difference between the measured and corrected signals. ***$p < 0.001$, two-way ANOVA (n=3).

Figure 5. Correction of Hb-absorption artifacts in other fiber-photometry settings

(A) Preparation for fiber-photometry measurement of GCaMP and tdTomato signals in the left M1, with the right M1 receiving local micro-electrical stimulation.

(B) Interleaved acquisition paradigm with 405 nm and 488 nm excitation lasers. Ca^{2+}-independent GCaMP signals ($GCaMP_{405}$) were excited by a 405 nm laser, whereas Ca^{2+}-dependent GCaMP signals ($GCaMP_{488}$) and tdTomato signals were excited by a 488 nm laser. This interleaved paradigm was used because $GCaMP_{405}$ and $GCaMP_{488}$ share nearly identical emission spectra and thus cannot be spectrally unmixed. Data were acquired at 50% duty cycle every 50 ms using a box-paradigm to avoid spectrometer frame loss during the trigger mode. The final sampling rate is 10 Hz for all signals.

(C) Measured $GCaMP_{488}$ and $GCaMP_{405}$ signals without any correction.

(D) Corrected $GCaMP_{488}$ using HbO and HbR dynamics derived from the full $GCaMP_{405}$ spectrum.

(E) Corrected $GCaMP_{488}$ using HbO and HbR dynamics from 3 datapoints in the $GCaMP_{405}$ spectrum (at 502, 523, and 544 nm).

(F) Corrected $GCaMP_{488}$ by regressing out the $GCaMP_{405}$ signal dynamics.

(G) Comparisons of the post-stimulus undershoot artifacts among uncorrected $GCaMP_{488}$ and corrected $GCaMP_{488}$ signals from three different settings as shown respectively in D-F. ***$p < 0.001$, paired *t*-test (n=31).

(H) Measured $GCaMP_{488}$ and tdTomato signals without any correction.

(I) Corrected $GCaMP_{488}$ using HbO and HbR dynamics derived from full the tdTomato spectrum.

(J) Corrected $GCaMP_{488}$ using HbO and HbR dynamics from 3 datapoints in the tdTomato spectrum (at 578, 594, and 610 nm).

(K) Corrected $GCaMP_{488}$ by regressing out the tdTomato signal dynamics.

(L) Comparisons of the post-stimulus undershoot artifacts among uncorrected $GCaMP_{488}$ and corrected $GCaMP_{488}$ signals from three different settings as shown respectively in I-K. ***$p < 0.001$, paired *t*-test (n=31).

(M) Sensitivity of the HbO, HbR, and HbT derived from full or 3-point in emission spectra. Comparison was made between these two conditions and also between the use of $GCaMP_{405}$ and tdTomato signals. *** $p < 0.001$, paired *t*-test (n=31); ### $p < 0.001$, two-way ANOVA (n=31).

Figure 6. Brain regional differences in hemodynamic response function

(A) Preparation for fiber-photometry measurement of GCaMP and tdTomato signals in the left M1 and right CPu, both have direct anatomical connection with the right M1 receiving local micro-electrical stimulation.

(B) Confocal images showing GCaMP and tdTomato expression in M1 and CPu.

(**C, D**) Peri-stimulus heatmaps and response time-courses of the changes in corrected GCaMP, derived HbO, derived HbR, and derived HbT, and the modeled HRFs in M1 and CPu, respectively. Inserted pie-charts indicate the ratio between positive (red) and negative (blue) HRF polarities. All per-stimulus heatmap color bars use the same unit as the time-course Y axis. Error bars represent standard deviation. See also Figure S11.

Supplementary Video 1 (Related to Figure 1). One representative simulation of paired excitation and emission photons traveling. Left: Initial ballistic photon flow of a 488 nm excitation beam incident from the optical fiber. Right: Diffuse propagation of the elicited 561 nm emissions captured by the same fiber.

Figure S1 (Related to Figure 1). Molar extinction coefficients of HbO and HbR as a function of wavelength. **(A)** Broad-band presentation. **(B)** The range commonly used to measure fluorescent sensor activity.

Figure S2 (Related to Figure 1). Power spectral distribution of several commonly used fluorescent sensors. CBV were measured by intravenously injecting a long-circulating red fluorescent dye, Rhodamine B (rhoCBV). Data were acquired continuously to generate time-courses and then converted to power spectra density using Fourier transform.

Figure S3 (Related to Figure 1). Light path simulation flow chart.

Figure S4 (Related to Figure 1). Monte Carlo simulation results.

(A) Illuminating distribution of the excitation 488 nm light. Left showing the spatial probability map, and middle and right showing normalized luminance-distance profiles in x and z directions.

(B) Receptive probability of the 515 nm emission light. Left showing the spatial probability map, and middle and right showing normalized luminance-distance profiles in x and z directions.

(C) Receptive probability of the 580 nm emission light. Left showing the spatial probability map, and middle and right showing normalized luminance-distance profiles in x and z directions.

Color bar indicates probability from 0 to 1.

Figure S5. Ex vivo quantification of Hb-absorption effects on photometry recordings

(**A**) $\Delta F/F$ changes before and after adding 1 mL of fresh mouse venous blood or 1 mL vehicle (0.9% saline) into 10 mL saline solution containing 10 µL Alexa 488 and 10 µL Alexa 568 fluorescent dyes. Adding saline decreased the concentrations of Alexa 488 and 568, which caused the slight but significant reduction in signal intensity. Error bars represent standard deviation. *** $p < 0.001$, *t*-test (n = 100 time points). ### $p < 0.001$, two-way ANOVA (n = 100).

(**B**) $\Delta F/F$ changes before and after 100% oxygen infusion into the solution containing blood or vehicle and fluorescent dye mixture. Error bars represent standard deviation. *** $p < 0.001$, *t*-test (n = 100 time points). ### $p < 0.001$, two-way ANOVA (n = 100).

(**C**) Normalized intensity spectra of the fluorescent solution mixture before and after adding blood or vehicle.

(**D**) Normalized intensity spectra of the blood-fluorescent solution mixture, or vehicle-fluorescent solution mixture, before and after oxygen infusion.

Figure S6 (Related to Figure 2). Number of continuous spectral datapoints needed to derive reliable hemoglobin concentration changes.

(**A**) Representative ΔC_{HbO} time-courses derived from activity-independent EYFP data using different number of spectral datapoints ranging from 3 to 45 (centered at 523 nm).

(**B**) Reduction of white noise was observed with increased number of datapoints. The derived ΔC_{HbO} exhibited minimized white noise when the number of datapoints reaching 35.

Figure S7 (Related to Figure 2). Comparison between corrected rhoCBV and HbT derived from EYFP signals.

(**A**) Power spectral distribution.

(**B**) Two-dimensional histogram summarizing rhoCBV and HbT power. Each datapoint in the frequency series is assigned to a two-dimensional matrix to make the histogram. Correlation is significant at the 0.001 level (Pearson correlation, $r = 0.98$). The color bar indicates counts on the log scale.

(**C**) Two-dimensional histogram summarizing z-scores of rhoCBV and HbT. Each datapoint in the time-courses is assigned to a two-dimensional matrix to make the histogram. Correlation is significant at the 0.001 level (Pearson correlation, $r = 0.66$). The color bar indicates counts on the log scale.

Figure S8 (Related to Figure 2). Fiber-photometry in the S1 with EYFP during hypercapnia (5% CO_2).

(**A-G**) Peri-event heatmaps showing repeated trials and average response time-courses of the changes in measured rhoCBV, measured EYFP, derived HbO, derived HbR, derived HbT, corrected rhoCBV, and

corrected EYFP, respectively. The gray-shaded segment indicates infusion of 5% CO_2. All color bars use the same unit as the time-course Y axis. Error bars represent standard deviation.

(**H, I**) Correction of the contaminated rhoCBV and EYFP signals, respectively, across all subjects and all trials (n=5, total trials =18; *** indicates $p < 0.001$, paired *t*-test).

(**J**) Power spectral distribution.

(**K**) Two-dimensional histogram summarizing rhoCBV and HbT power. Each datapoint in the frequency series is assigned to a two-dimensional matrix to make the histogram. Correlation is significant at the 0.001 level (Pearson correlation, $r = 0.98$). The color bars indicates counts on the log scale.

(**L**) rhoCBV exhibited higher sensitivity than derived HbT. Error bars represent standard deviation. *** indicates $p < 0.001$ (paired *t*-test).

(**M**) Two-dimensional histogram summarizing rhoCBV and HbT z-scores. Each datapoint in the time-courses is assigned to a two-dimensional matrix to make the histogram. Correlation is significant at the 0.001 level (Pearson correlation, $r = 0.50$). The color bars indicates counts on the log scale.

Figure S9 (Related to Figure 3). Simultaneous fMRI and fiber-photometry recording showing optogenetic-evoked CBV-fMRI, GCaMP and rhoCBV changes in the S1.

(**A**) GCaMP and channelrhodopsin-2 (ChR2) were virally expressed using AAV under the CaMKIIα promoter in the S1 and ventroposterior (VP) thalamus, respectively. Rhodamine B was intravenously injected to achieve CBV measurement.

(**B**) Confocal images showing GCaMP expression.

(**C**) MRI-CBV activation maps in response to optogenetic stimulation of VP.

(**D**) Uncorrected GCaMP, rhoCBV, and MRI-CBV time-courses (n=3, total trials =33 trials). After a short optogenetic stimulation of VP (60Hz, 10mW power, 0.5 ms pulse width for 1 s), uncorrected GCaMP signal exhibited a strong undershoot with signal pattern mirrored the rhoCBV and MRI-CBV data, indicative of significant Hb absorption *in vivo*.

Figure S10 (Related to Figure 3). Comparison of the peak GCaMP responses before and after Hb-absorption correction. The peak amplitude of GCaMP responses is significantly higher in the corrected GCaMP compared with uncorrected GCaMP. (*** indicates $p<0.001$, paired *t*-test, n=27)

Figure S11 (Related to Figure 4). Hb-absorption effects on GCaMP signal measurement during 5% isoflurane challenges.

(A) Preparation for fiber-photometry measurement of GCaMP and Rhodamine B signals in the left M1. Ca^{2+}-independent GCaMP signal ($GCaMP_{405}$) was excited by a 405 nm laser and used for hemodynamic correction. rhoCBV signals were measured as described in **Figure 2**.

(B) Measured and corrected $GCaMP_{405}$ time-courses before, during, and after 2-min 5% isoflurane challenges (baseline = 0.5% isoflurane). The gray-shaded segment indicates the isoflurane period. Error bars represent standard deviation.

(C) Scatter plots of measured and corrected $GCaMP_{405}$ signals at 1, 2, 3, 4, 5, 6, and 7 min after the onset of the isoflurane challenge (n = 5, $p < 0.001$, two-way ANOVA).

(D) Derived HbO, HbR, and HbT time-courses before, during, and after the isoflurane challenge.

(E) Measured and corrected rhoCBV time-courses before and after the isoflurane challenge. Read-out from the Rhodamine B could be misinterpreted without hemodynamic correction.

(F) Scatter plots of measured and corrected rhoCBV signals at 1, 2, 3, 4, 5, 6, and 7 min after the onset of the isoflurane challenge (n = 5, $p < 0.001$, two-way ANOVA).

Figure S12 (Related to Figure 4). Hb-absorption effects on GCaMP signal measurement during pharmacological studies

(A) Fiber-photometry measurement of GCaMP and tdTomato signals in the left M1.

(B) Measured and corrected tdTomato time-courses before and after administering an α_2 adrenergic antagonist Atipamezole (1 mg/kg, s.c., Zoetis, Parsipanny, NJ).

(C) Scatter plots of measured and corrected tdTomato signals at 2, 4, 6, 8, and 10 min after the atipamezole administration (n = 3, $p < 0.001$, two-way ANOVA).

(D) Derived HbO, HbR, and HbT time-courses before and after the atipamezole administration. Increased CBV might result from the redistribution of blood supply to active brain regions (Bekar et al., 2012).

(E) Measured and corrected GCaMP time-courses before and after the atipamezole administration. the increased GCaMP activity in the cortex would have been otherwise unchanged without hemodynamic correction.

(F) Scatter plots of measured and corrected GCaMP signals at 2, 4, 6, 8, and 10 min after the atipamezole administration (n = 3, $p < 0.05$, two-way ANOVA).

Figure S13 (Related to Figure 5). HRF calculation and validation.

(**A**) Pipeline for estimating HRF from tdTomato-derived HbT and GCaMP signals. Yellow arrows indicate post-stimulus undershoot caused by Hb absorption. Note that using uncorrected GCaMP caused an HRF amplitude shift at t=0.

(**B**) Strategy to deconvolve HRF form preprocessed HbT and GCaMP signals.

(**C**) Validation of the HRF using a separate dataset naïve to HRF calculation. HRF was convolved with GCaMP data to predict HbT changes (black trace). High correlation was observed between the predicted and tdTomato-derived HbT (purple trace).

Figure S14. Simulated detection volume and its projected probability.

Figure S15. Signal drop in measured EYFP and tdTomato signals were correlated to the CBV changes.

(**A**) Two-dimensional histogram summarizing % changes of corrected rhoCBV and measured EYFP signal. Each datapoint in the time-courses is assigned into a two-dimensional matrix to make the histogram. Correlation is significant at the 0.001 level (Pearson correlation, r = -0.62). Color bars indicate datapoint counts. Linear fit (red line) and 95% confidence interval (pink lines) are also shown.

(**B**) Two-dimensional histogram summarizing % changes of MRI-CBV and measured tdTomato signal. Each datapoint in the time-courses is assigned into a two-dimensional matrix to make the histogram. Correlation is significant at the 0.001 level (Pearson correlation, r = -0.33). Color bars indicate datapoint counts. Linear fit (red line) and 95% confidence interval (pink lines) are also shown.

Figure S16. Correcting GCaMP signals by regressing out the HbT.

(A) short (1 s) stimulation

(B) long (10 s) stimulation.

Figure S17. Quantification of Hb-absorption effects using residue signals of fiber-photometry

(**A**) Preparation for fiber-photometry measurement of GCaMP signal in the S1 of the forelimb region.

(**B**) Confocal images showing GCaMP expression.

(**C**) Simultaneous dual-spectral photometry recording of GCaMP and rhoCBV.

(**D-I**) Peri-stimulus heatmaps showing repeated trials and average response time-courses of the changes in uncorrected GCaMP, measured rhoCBV, derived HbO, derived HbR, corrected GCaMP, and derived HbT, respectively. The gray-shaded segment indicates forepaw-stimulation period. All color bars use the same unit as the time-course Y axis. Error bars represent standard deviation.

(**J**) Correction of the post-stimulus dip of GCaMP signals (n = 2, total trials = 6; ** indicates $p < 0.01$, paired t-test).

(**K**) Two-dimensional histogram summarizing rhoCBV and HbT z-scores. Each datapoint in the time-courses is assigned into a two-dimensional matrix to make the histogram. Correlation is significant at the

0.001 level (Pearson correlation, $r = 0.28$). Colorbar indicates the number of datapoints. Linear fit (red line) and 95% confidence interval (pink lines) are also shown.

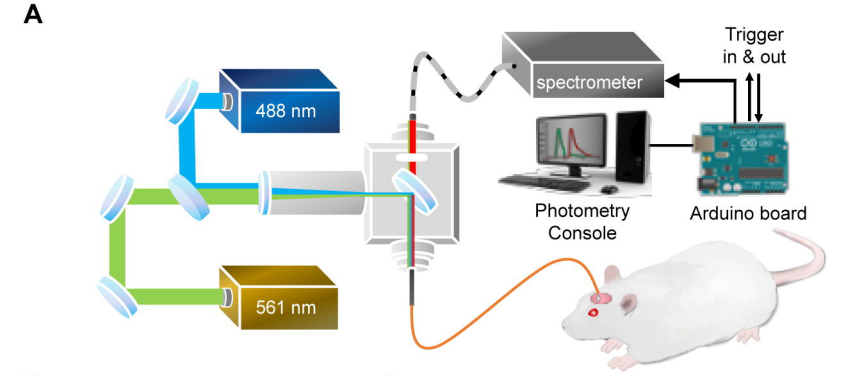
A
488 nm
561 nm
spectrometer
Trigger
in & out
Photometry
Console
Arduino board

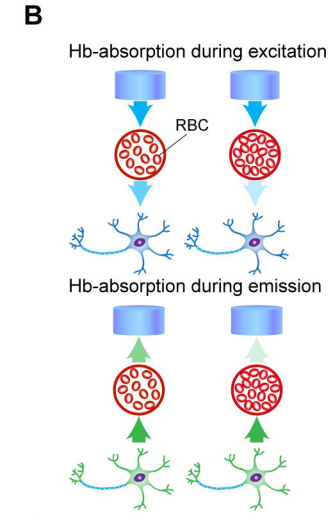
B
Hb-absorption during excitation
RBC
Hb-absorption during emission

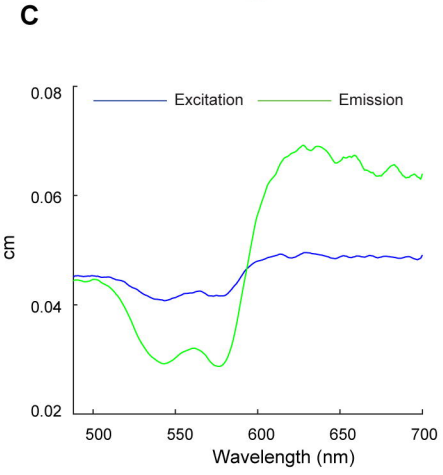
C
Excitation
Emission
0.08
0.06
0.04
0.02
cm
500
550
600
650
700
Wavelength (nm)

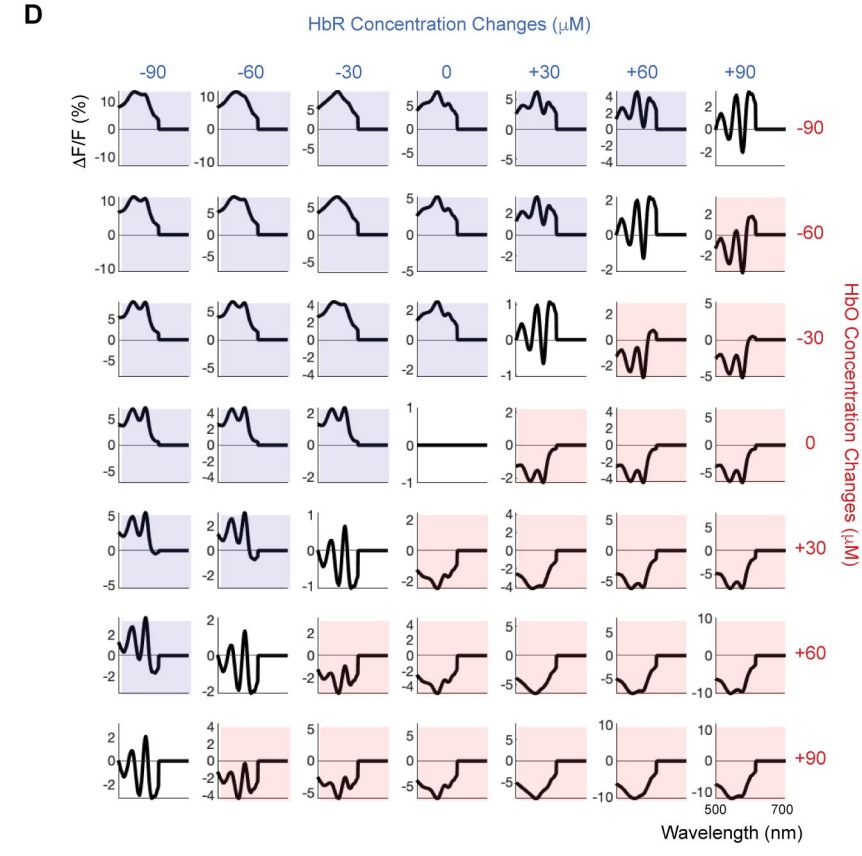
D
HbR Concentration Changes (μM)
-90
-60
-30
0
+30
+60
+90
ΔF/F (%)
HbO Concentration Changes (μM)
500
700
Wavelength (nm)

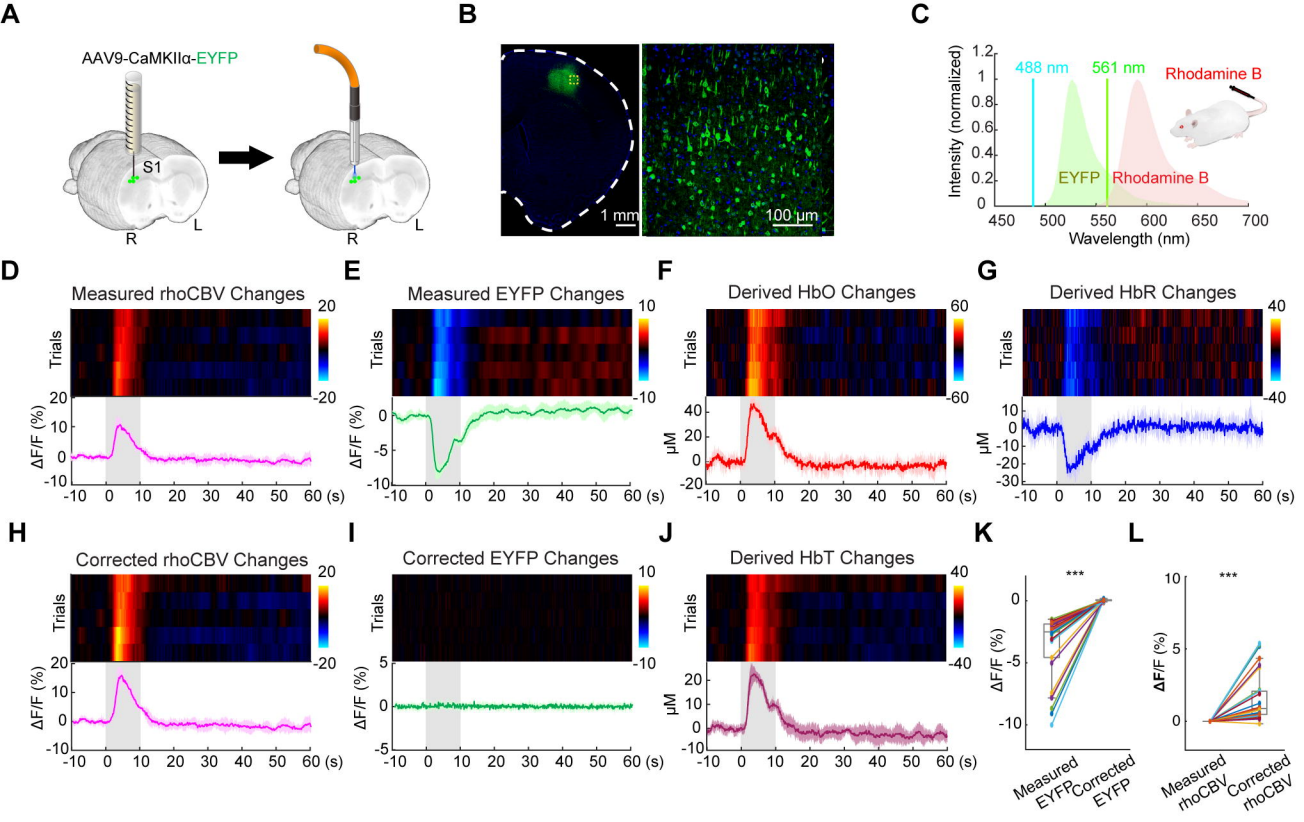
A
AAV9-CaMKIIα-EYFP
S1
R
L
R
L
B
1 mm
100 μm
C
488 nm
561 nm
Rhodamine B
EYFP
Rhodamine B
Intensity (normalized)
Wavelength (nm)
D
Measured rhoCBV Changes
Trials
ΔF/F (%)
E
Measured EYFP Changes
F
Derived HbO Changes
μM
G
Derived HbR Changes
H
Corrected rhoCBV Changes
I
Corrected EYFP Changes
J
Derived HbT Changes
K
***
Measured EYFP
Corrected EYFP
L
***
Measured rhoCBV
Corrected rhoCBV
(s)

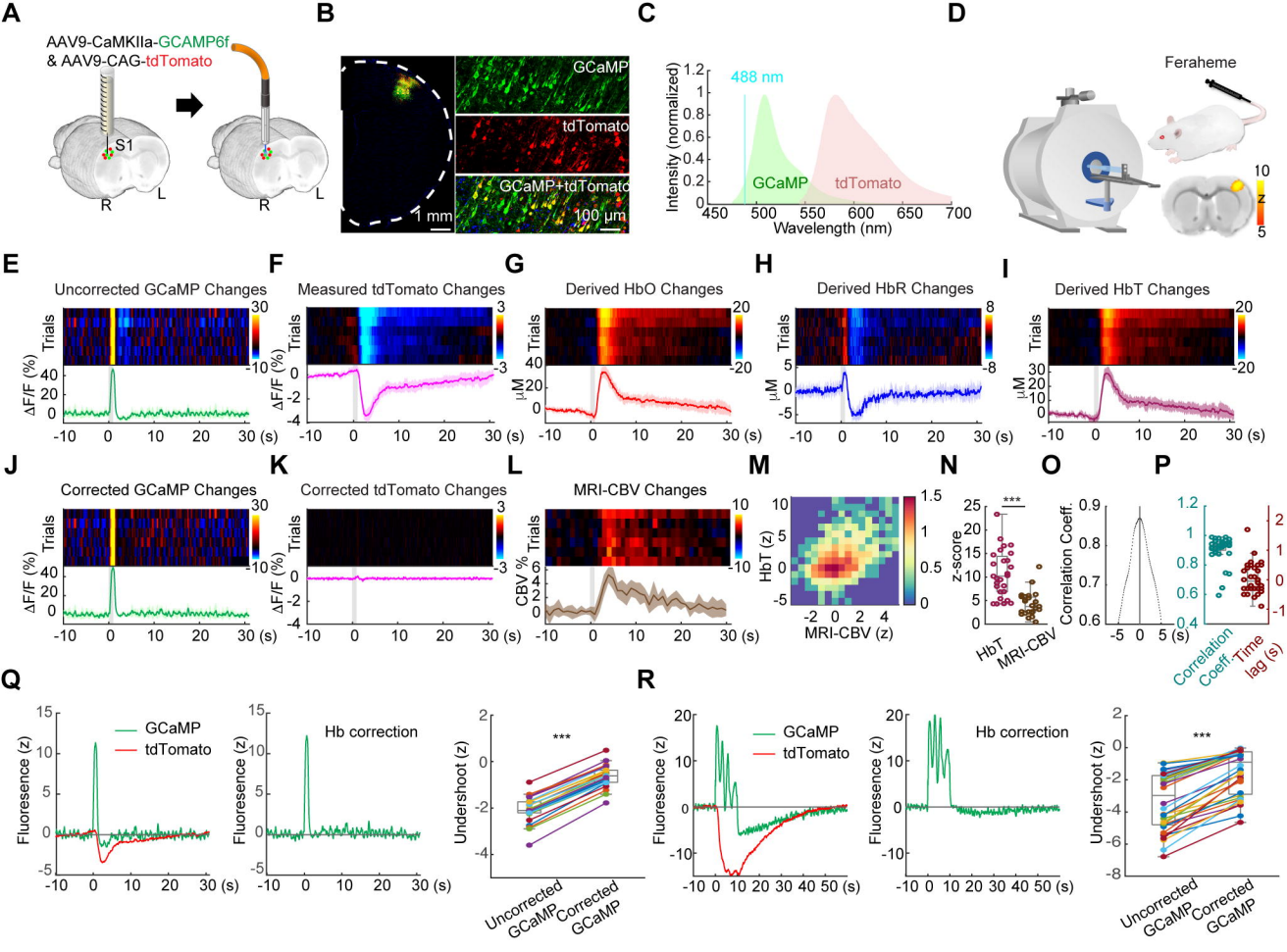
A
AAV9-CaMKIIa-GCAMP6f
& AAV9-CAG-tdTomato
S1
R
L
R
L
B
GCaMP
tdTomato
GCaMP+tdTomato
1 mm
100 μm
C
488 nm
GCaMP
tdTomato
Intensity (normalized)
Wavelength (nm)
D
Feraheme
10
z
5
E
Uncorrected GCaMP Changes
F
Measured tdTomato Changes
G
Derived HbO Changes
H
Derived HbR Changes
I
Derived HbT Changes
Trials
ΔF/F (%)
μM
(s)
J
Corrected GCaMP Changes
K
Corrected tdTomato Changes
L
MRI-CBV Changes
CBV %
M
HbT (z)
MRI-CBV (z)
N
z-score
***
HbT
MRI-CBV
O
Correlation Coeff.
(s)
P
Correlation Coeff.
Time lag (s)
Q
GCaMP
tdTomato
Fluorescence (z)
Hb correction
Undershoot (z)
***
Uncorrected GCaMP
Corrected GCaMP
R
GCaMP
tdTomato
Fluorescence (z)
Hb correction
Undershoot (z)
***
Uncorrected GCaMP
Corrected GCaMP

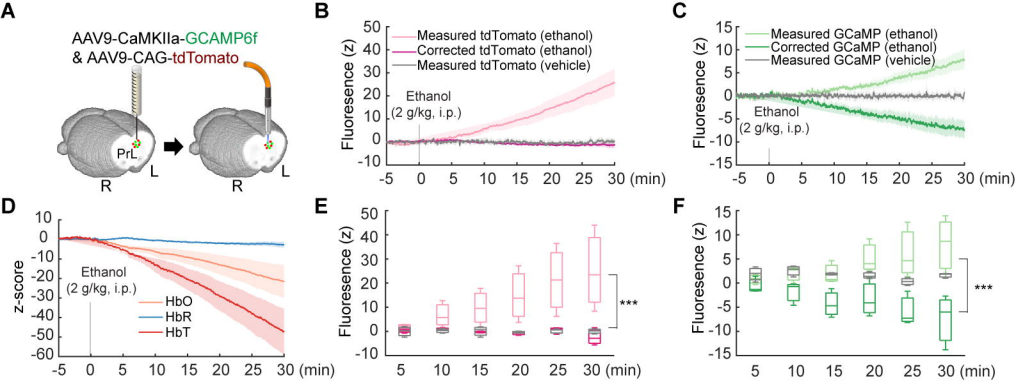
A
AAV9-CaMKIIa-GCAMP6f
& AAV9-CAG-tdTomato
PrL
R
L
R
L
B
Measured tdTomato (ethanol)
Corrected tdTomato (ethanol)
Measured tdTomato (vehicle)
Ethanol
(2 g/kg, i.p.)
Fluoresence (z)
(min)
C
Measured GCaMP (ethanol)
Corrected GCaMP (ethanol)
Measured GCaMP (vehicle)
Ethanol
(2 g/kg, i.p.)
Fluoresence (z)
(min)
D
Ethanol
(2 g/kg, i.p.)
HbO
HbR
HbT
z-score
(min)
E
Fluoresence (z)
***
(min)
F
Fluoresence (z)
***

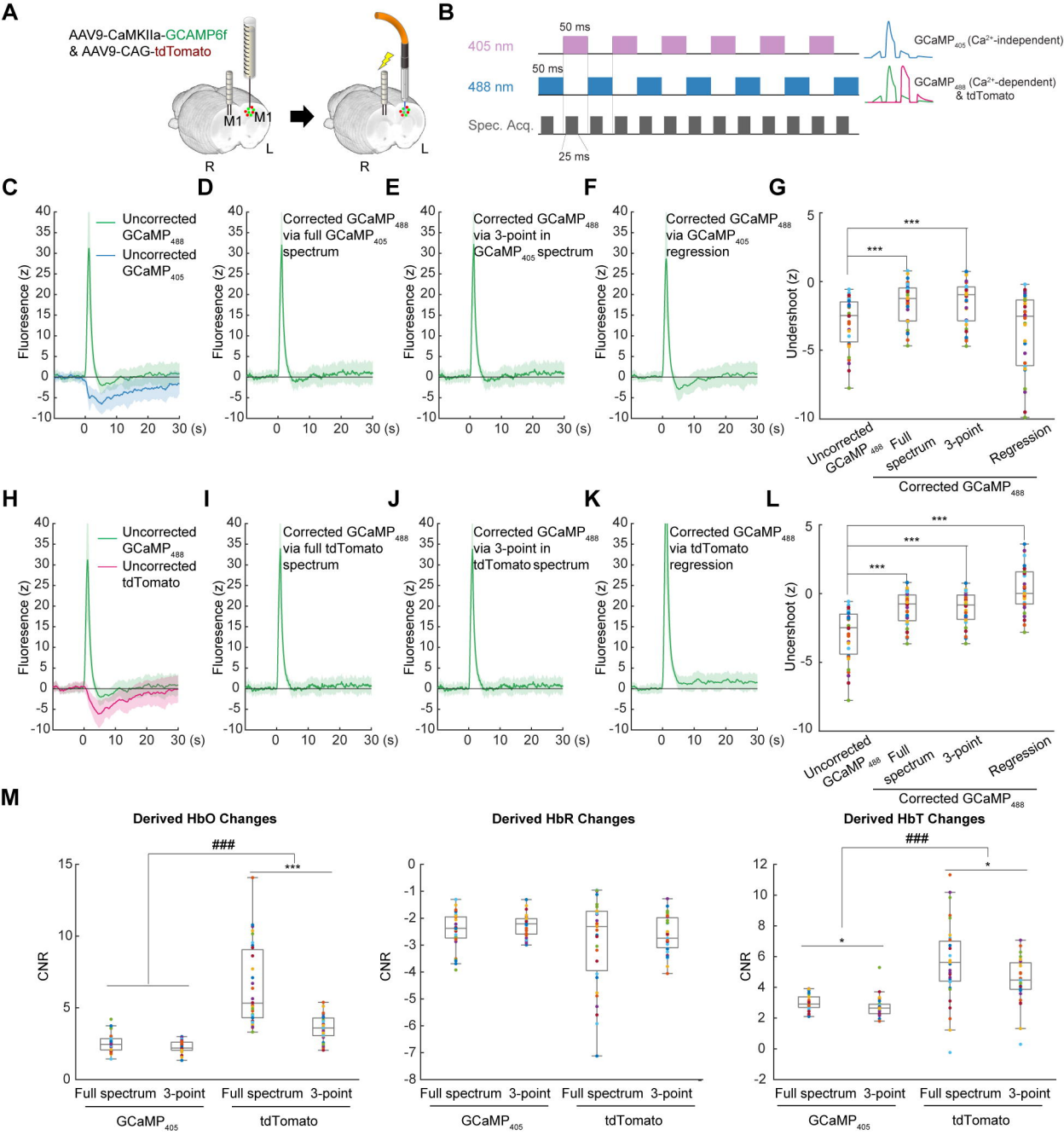
A
AAV9-CaMKIIa-GCAMP6f
& AAV9-CAG-tdTomato
M1
M1
R
L
R
L
B
50 ms
405 nm
50 ms
488 nm
Spec. Acq.
25 ms
GCaMP405 (Ca2+-independent)
GCaMP488 (Ca2+-dependent)
& tdTomato
C
Uncorrected GCaMP488
Uncorrected GCaMP405
Fluorescence (z)
D
Corrected GCaMP488 via full GCaMP405 spectrum
E
Corrected GCaMP488 via 3-point in GCaMP405 spectrum
F
Corrected GCaMP488 via GCaMP405 regression
G
Undershoot (z)
***
***
Uncorrected GCaMP488
Full spectrum
3-point
Regression
Corrected GCaMP488
H
Uncorrected GCaMP488
Uncorrected tdTomato
I
Corrected GCaMP488 via full tdTomato spectrum
J
Corrected GCaMP488 via 3-point in tdTomato spectrum
K
Corrected GCaMP488 via tdTomato regression
L
M
Derived HbO Changes
###
***
Derived HbR Changes
Derived HbT Changes
###
*
*
CNR
Full spectrum
3-point
GCaMP405
tdTomato

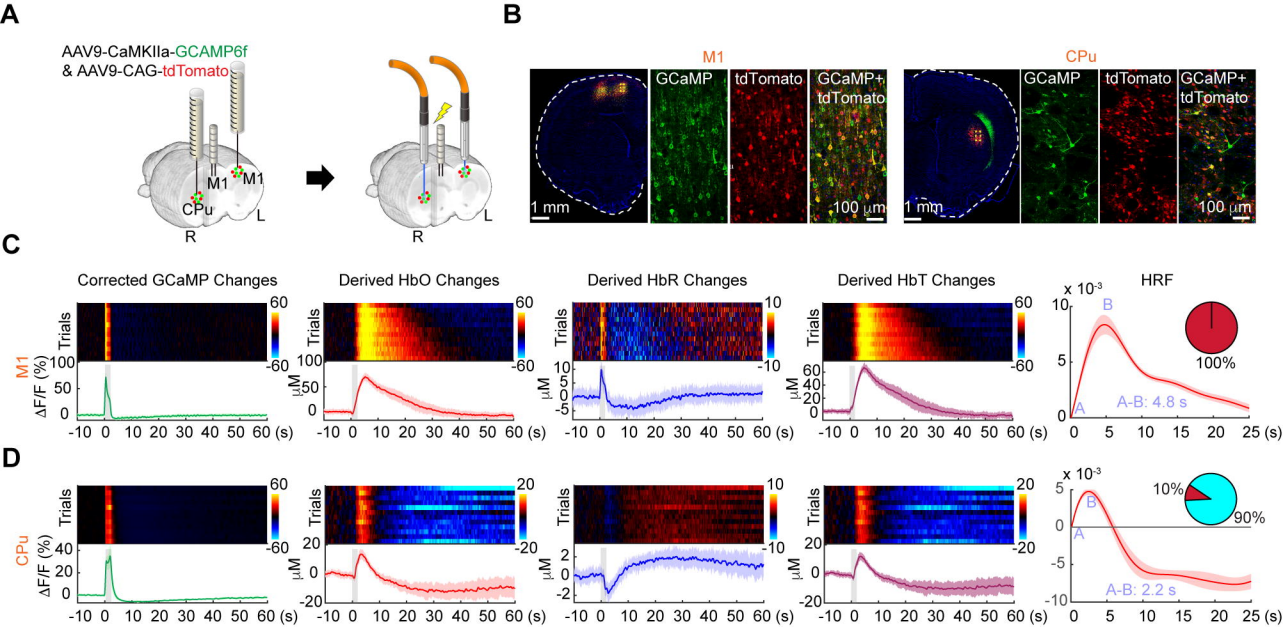
A
AAV9-CaMKIIa-GCAMP6f
& AAV9-CAG-tdTomato
M1
M1
CPu
R
L
R
L
B
M1
CPu
GCaMP
tdTomato
GCaMP+
tdTomato
1 mm
100 μm
C
Corrected GCaMP Changes
Derived HbO Changes
Derived HbR Changes
Derived HbT Changes
HRF
M1
Trials
ΔF/F (%)
μM
x 10-3
A
B
100%
A-B: 4.8 s
D
CPu
10%
90%
A-B: 2.2 s
(s)

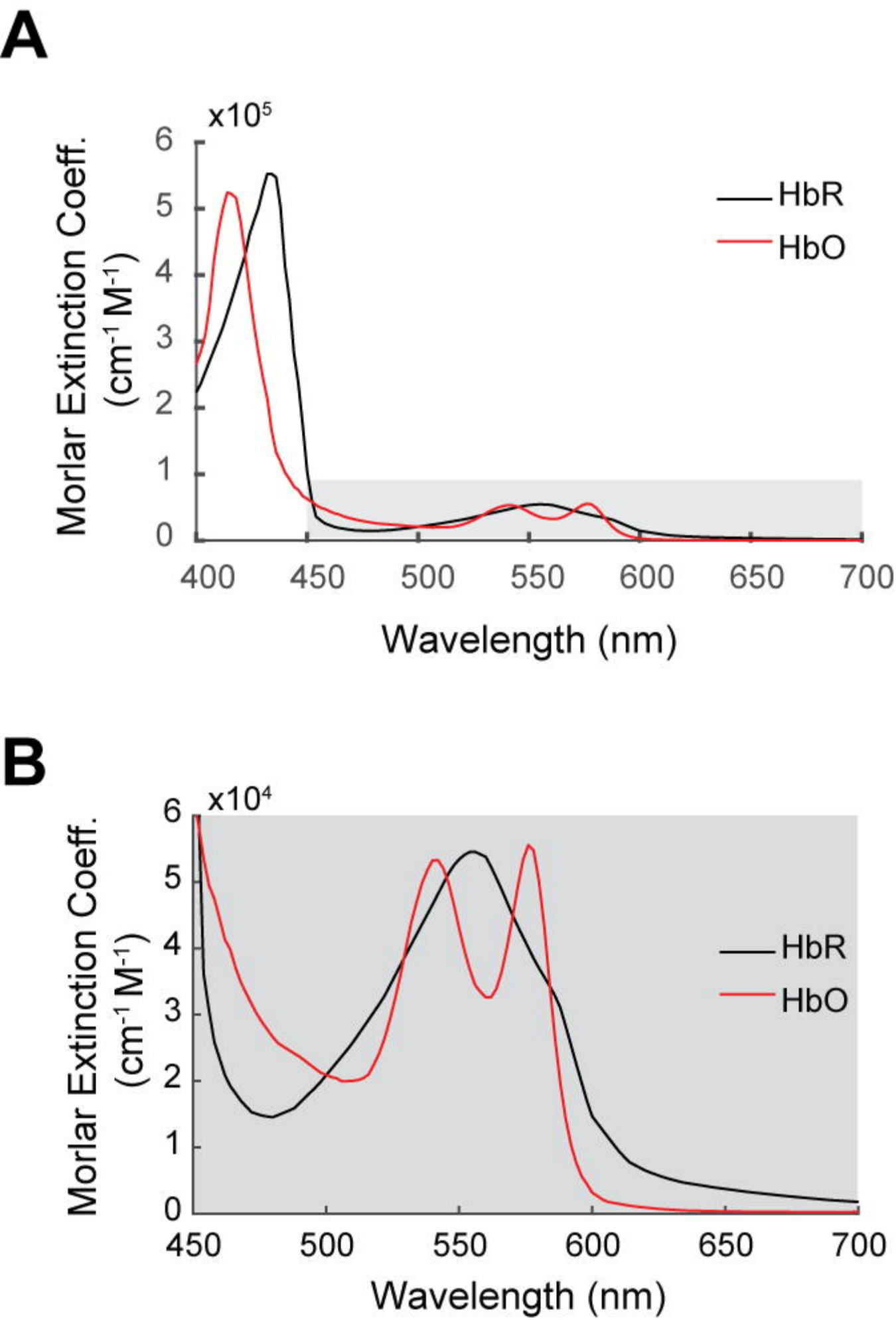
A
x10^5
6
5
4
3
2
1
0
Morlar Extinction Coeff.
(cm^-1 M^-1)
HbR
HbO
400
450
500
550
600
650
700
Wavelength (nm)
B
x10^4
6
5
4
3
2
1
0
Morlar Extinction Coeff.
(cm^-1 M^-1)
HbR
HbO
450
500
550
600
650
700
Wavelength (nm)

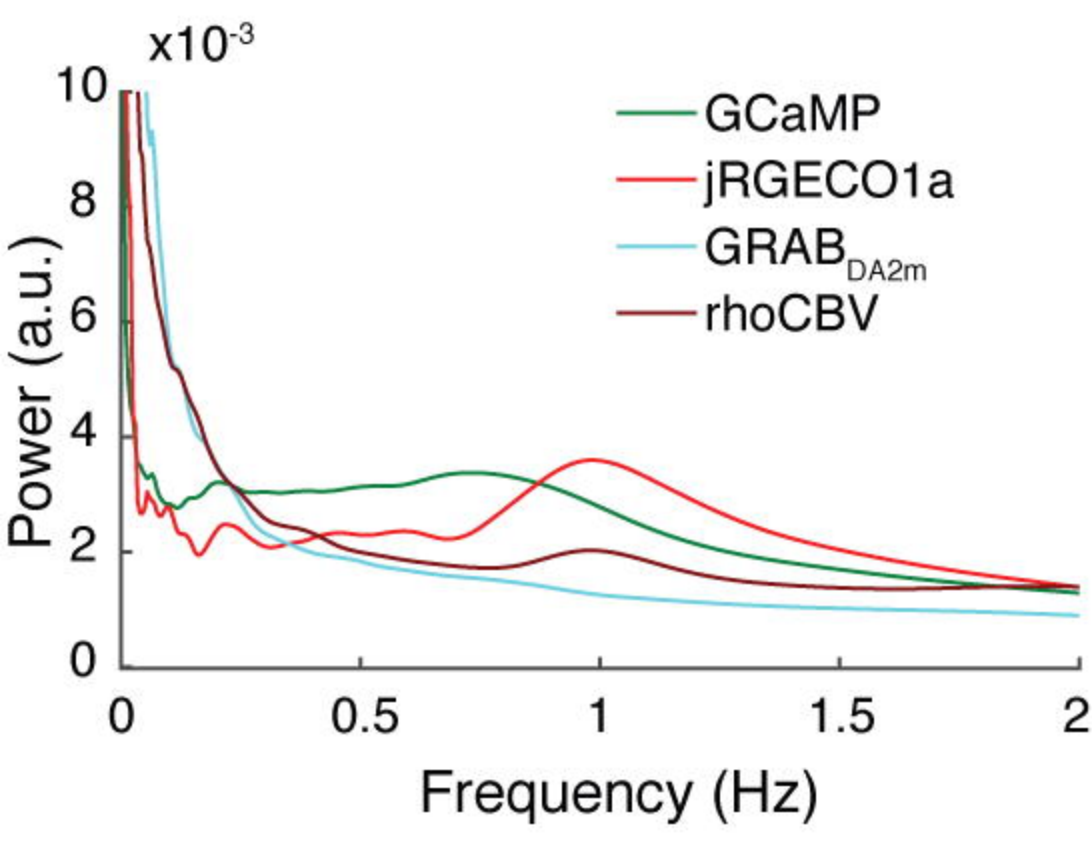
x10-3
10
8
6
4
2
0
Power (a.u.)
GCaMP
jRGECO1a
GRABDA2m
rhoCBV
0
0.5
1
1.5
2
Frequency (Hz)

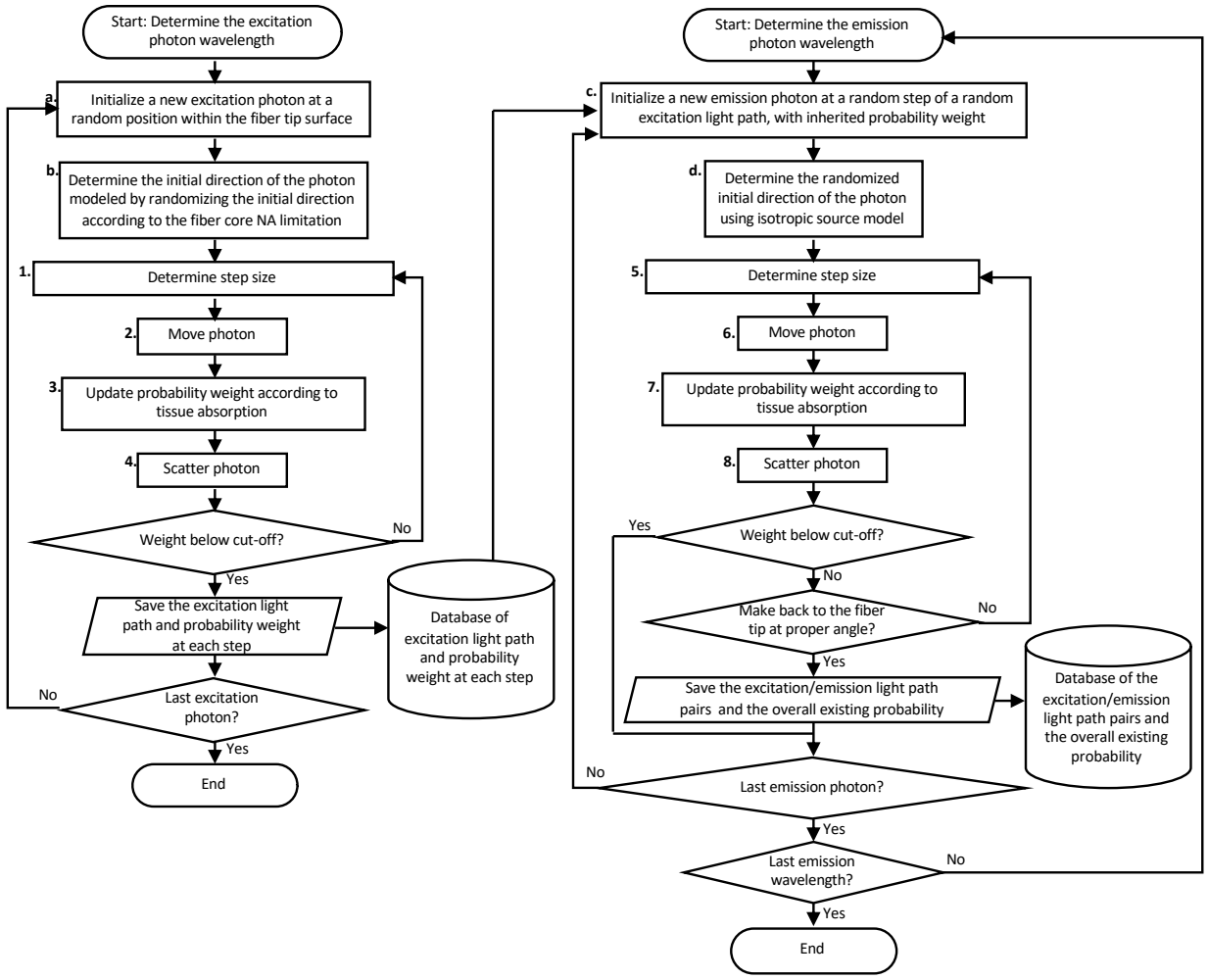

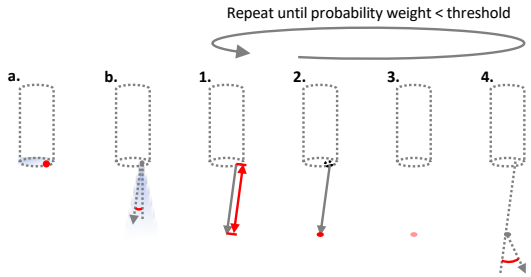

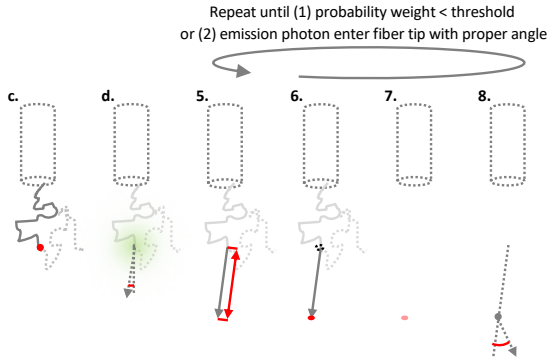

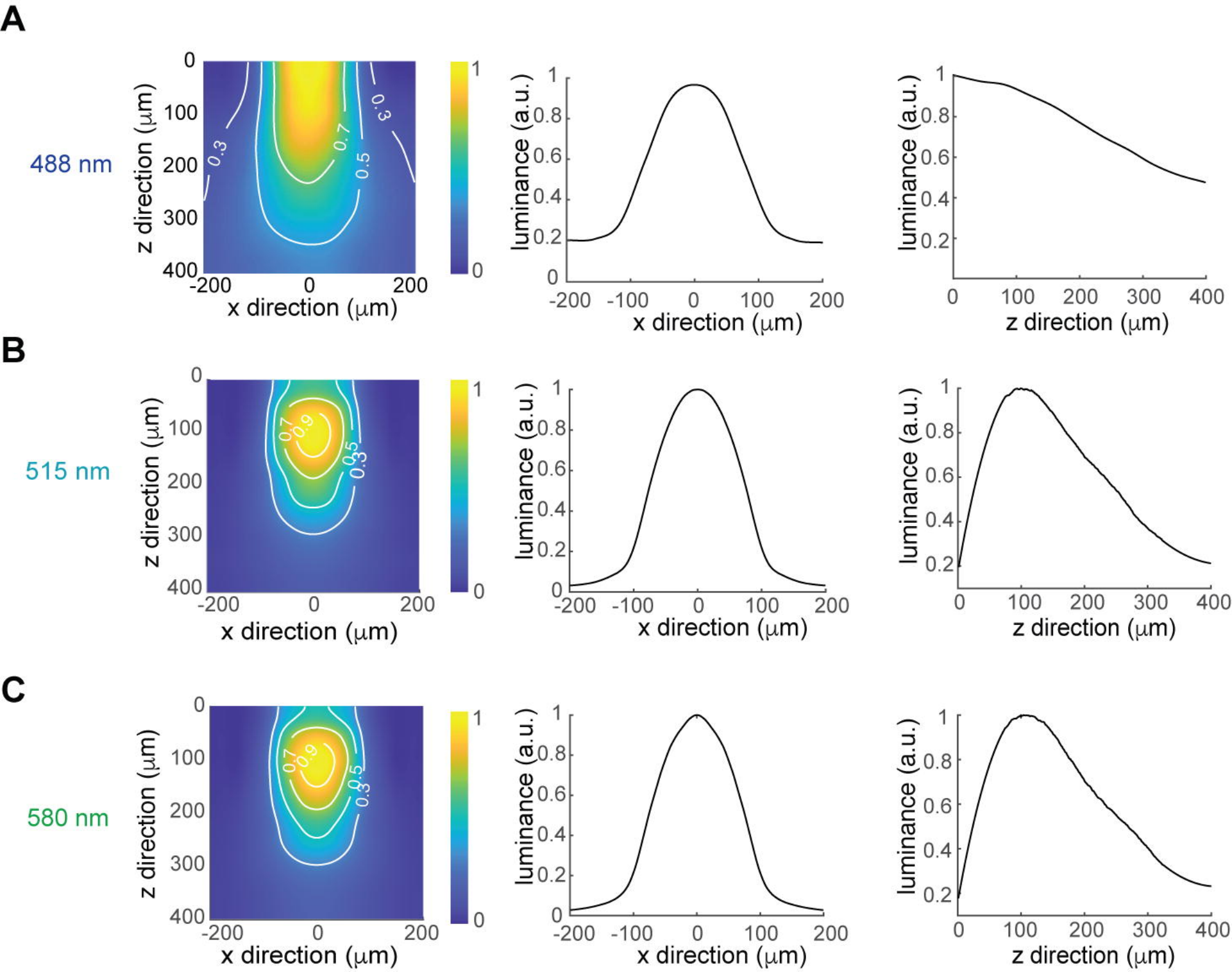
A
488 nm
z direction (μm)
x direction (μm)
luminance (a.u.)
B
515 nm
C
580 nm

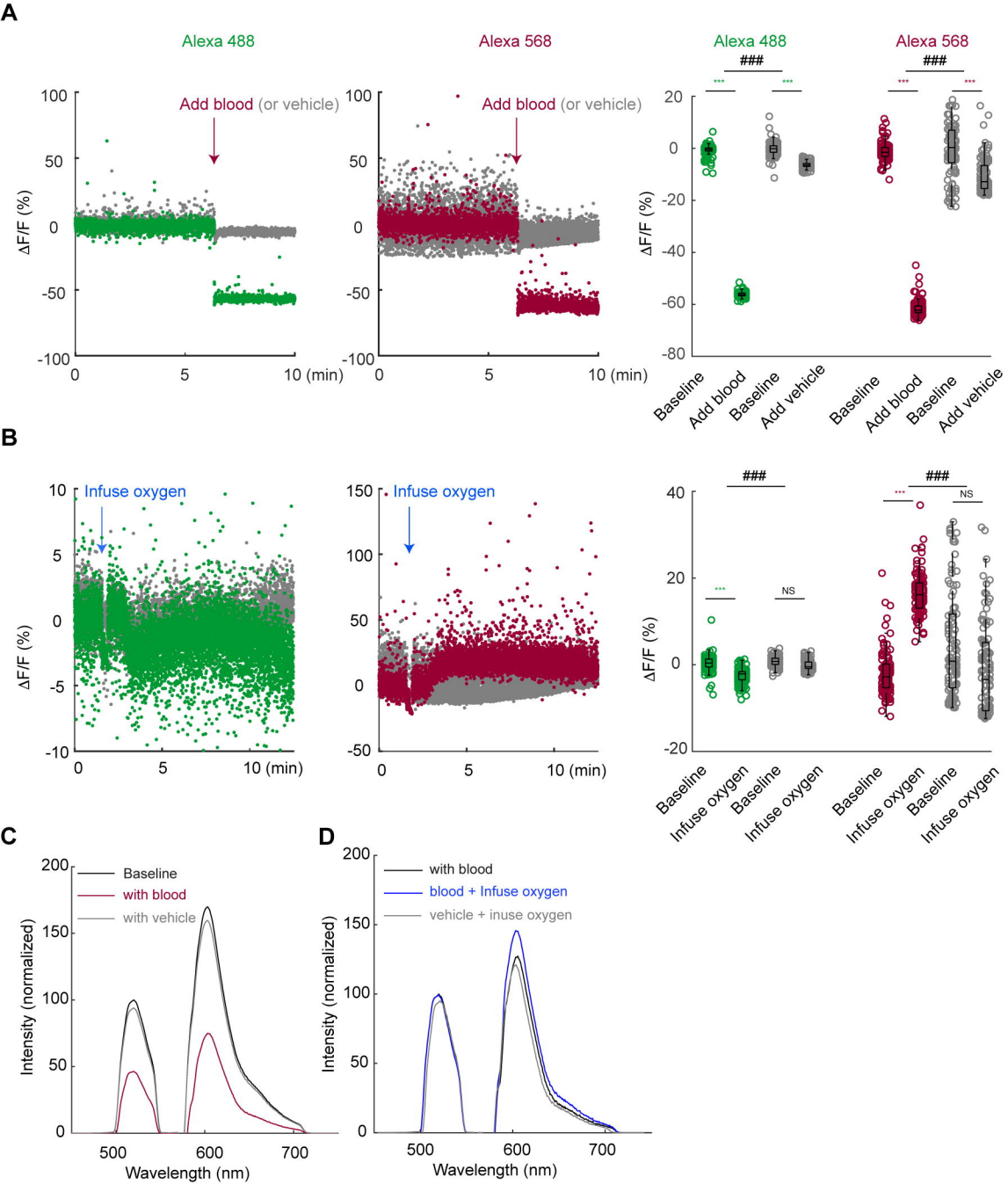
A
Alexa 488
Alexa 568
Add blood (or vehicle)
ΔF/F (%)
10 (min)
Alexa 488
Alexa 568
###
***
Baseline
Add blood
Add vehicle
B
Infuse oxygen
NS
C
Baseline
with blood
with vehicle
Intensity (normalized)
Wavelength (nm)
D
with blood
blood + Infuse oxygen
vehicle + inuse oxygen

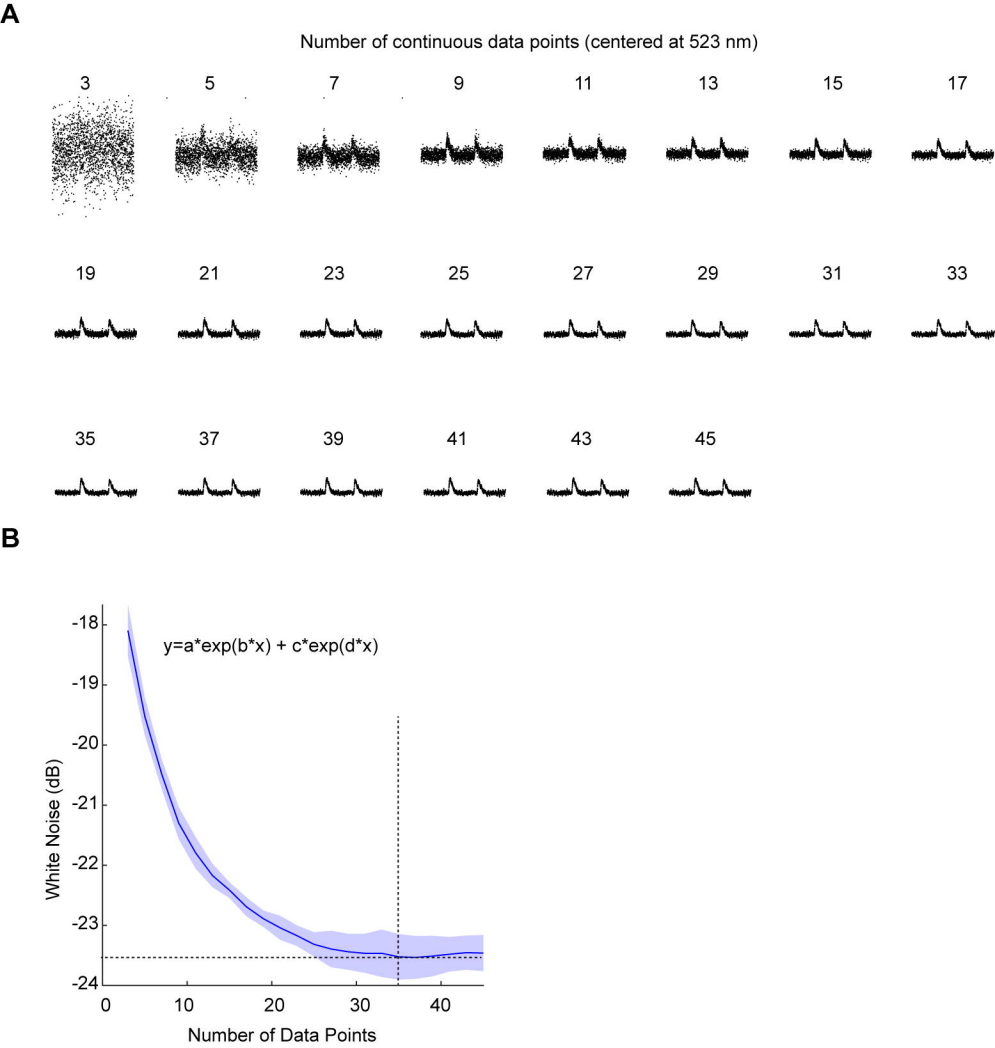
A
Number of continuous data points (centered at 523 nm)
3
5
7
9
11
13
15
17
19
21
23
25
27
29
31
33
35
37
39
41
43
45
B
y=a*exp(b*x) + c*exp(d*x)
White Noise (dB)
-18
-19
-20
-21
-22
-23
-24
0
10
20
30
40
Number of Data Points

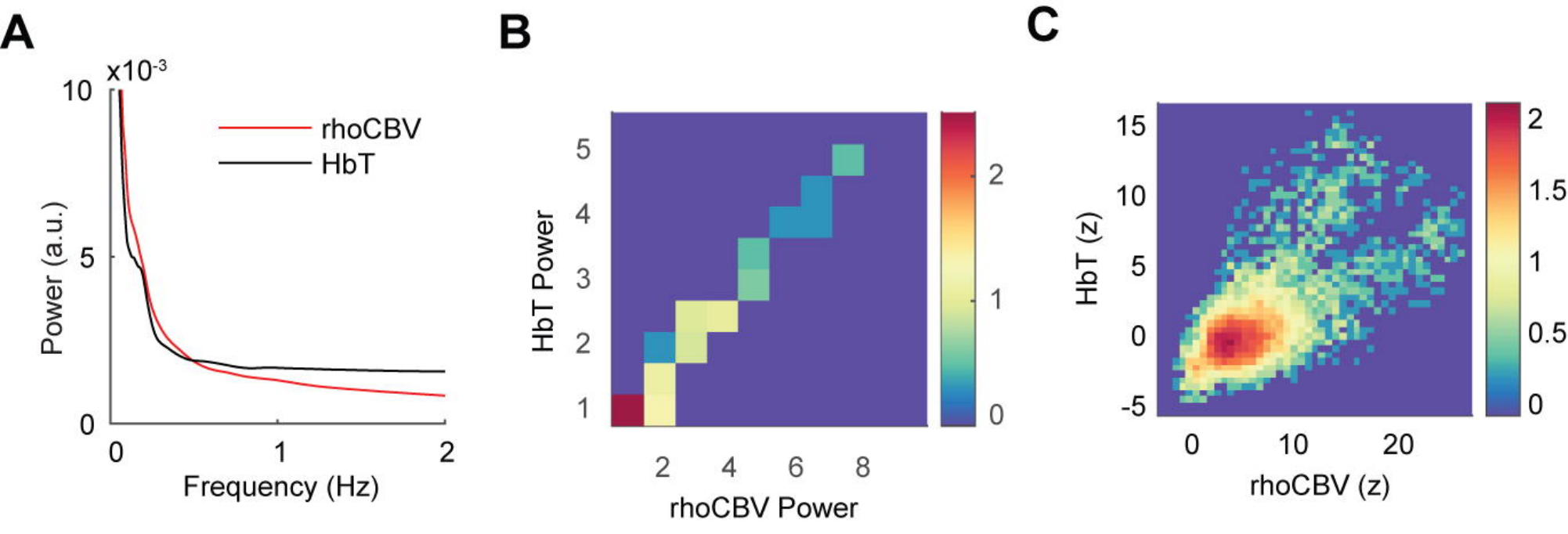
A
x10-3
10
5
0
Power (a.u.)
rhoCBV
HbT
0
1
2
Frequency (Hz)
B
HbT Power
5
4
3
2
1
2
4
6
8
rhoCBV Power
2
1
0
C
HbT (z)
15
10
5
0
-5
0
10
20
rhoCBV (z)
2
1.5
1
0.5
0

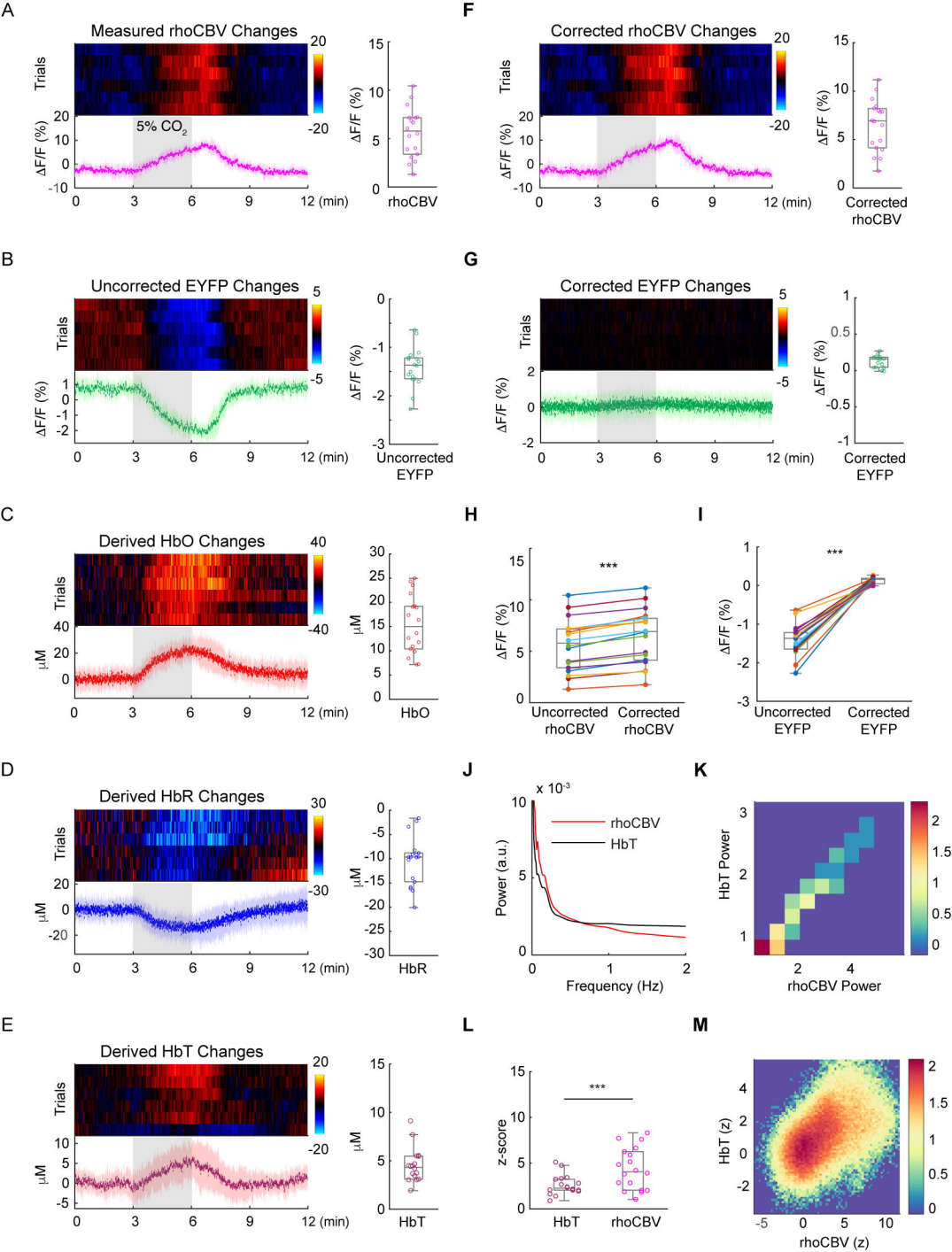
A
Measured rhoCBV Changes
Trials
5% CO2
ΔF/F (%)
12 (min)
rhoCBV
F
Corrected rhoCBV Changes
Corrected rhoCBV
B
Uncorrected EYFP Changes
Uncorrected EYFP
G
Corrected EYFP Changes
Corrected EYFP
C
Derived HbO Changes
μM
HbO
H
***
Uncorrected rhoCBV
Corrected rhoCBV
I
Uncorrected EYFP
Corrected EYFP
D
Derived HbR Changes
HbR
J
x 10-3
rhoCBV
HbT
Power (a.u.)
Frequency (Hz)
K
HbT Power
rhoCBV Power
E
Derived HbT Changes
HbT
L
z-score
M
HbT (z)
rhoCBV (z)

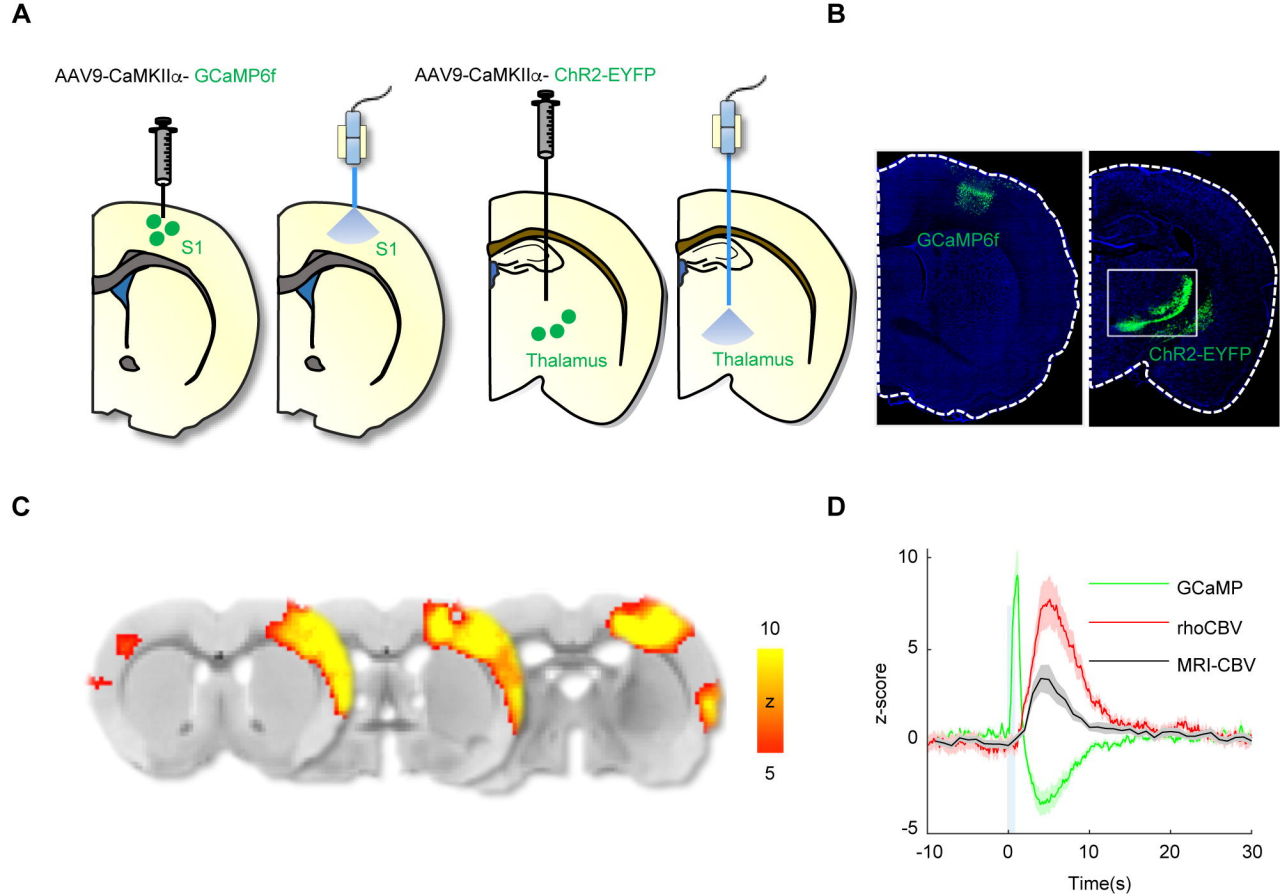
A
AAV9-CaMKIIα- GCaMP6f
AAV9-CaMKIIα- ChR2-EYFP
S1
S1
Thalamus
Thalamus
B
GCaMP6f
ChR2-EYFP
C
10
z
5
D
10
5
0
-5
z-score
-10
0
10
20
30
Time(s)
GCaMP
rhoCBV
MRI-CBV

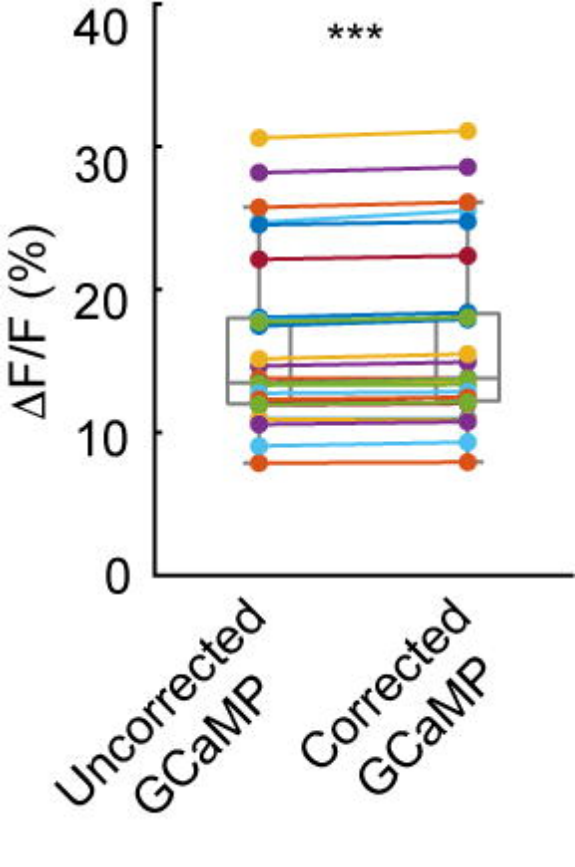
***
40
30
20
10
0
ΔF/F (%)
Uncorrected GCaMP
Corrected GCaMP

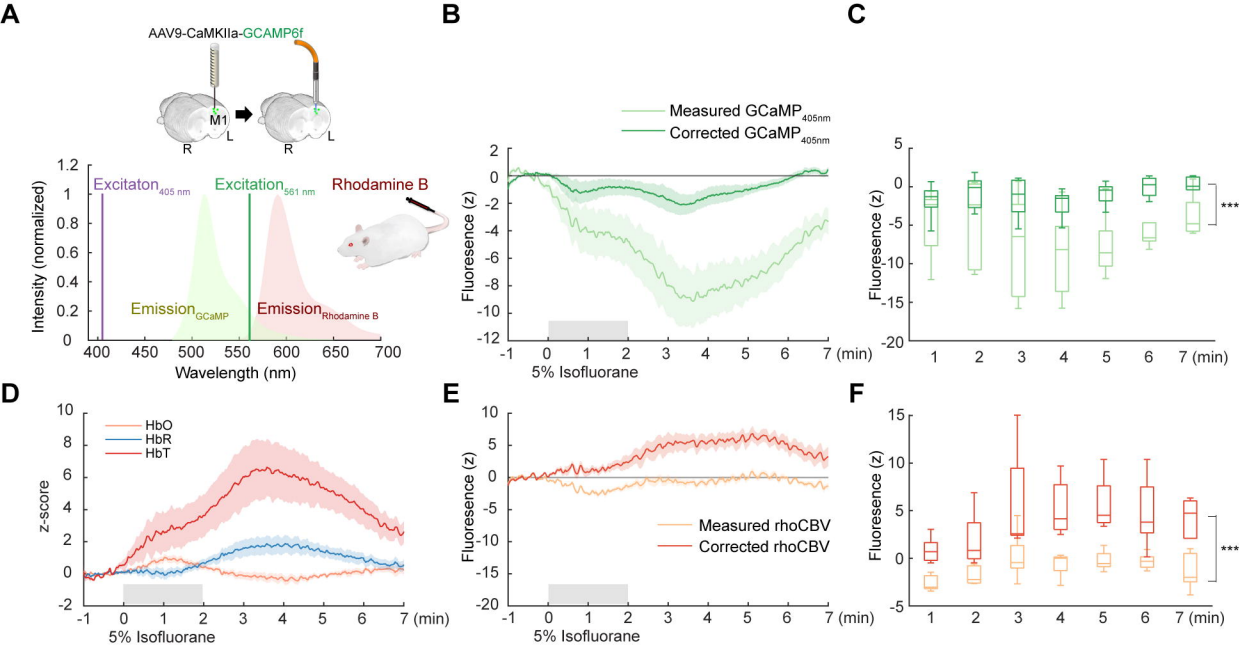
A
AAV9-CaMKIIa-GCAMP6f
M1
R
L
R
L
Excitaton405 nm
Excitation561 nm
Rhodamine B
Emission GCaMP
Emission Rhodamine B
Intensity (normalized)
Wavelength (nm)
B
Measured GCaMP405nm
Corrected GCaMP405nm
Fluorescence (z)
5% Isofluorane
(min)
C
Fluorescence (z)
***
(min)
D
HbO
HbR
HbT
z-score
5% Isofluorane
(min)
E
Measured rhoCBV
Corrected rhoCBV
Fluorescence (z)
5% Isofluorane
(min)
F
Fluorescence (z)
***
(min)

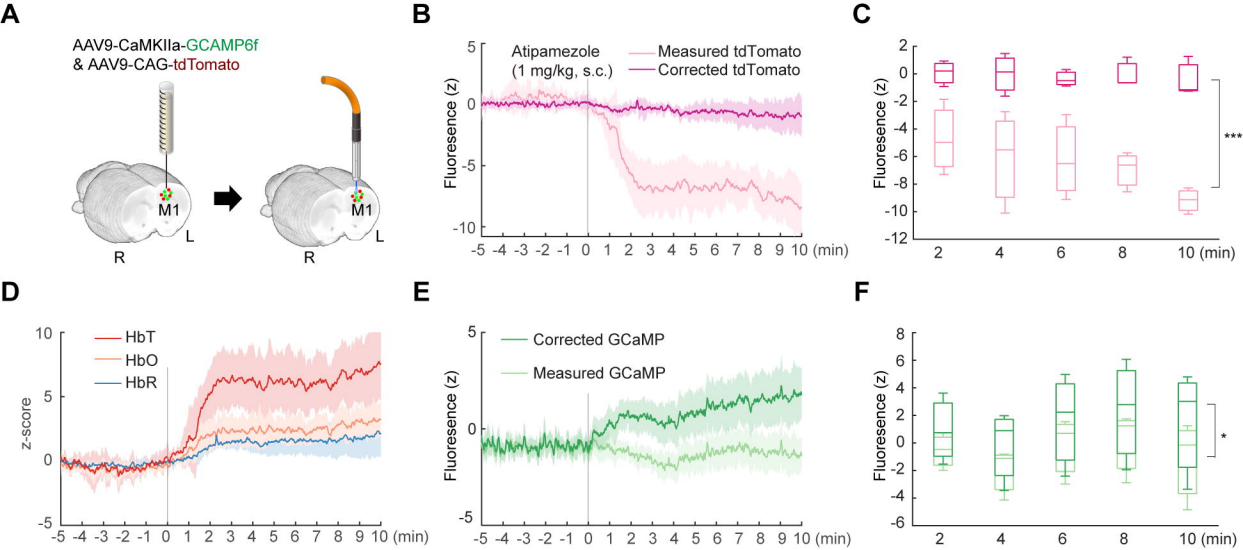
A
AAV9-CaMKIIa-GCAMP6f
& AAV9-CAG-tdTomato
M1
L
R
M1
L
R
B
Atipamezole
(1 mg/kg, s.c.)
Measured tdTomato
Corrected tdTomato
Fluorescence (z)
5
0
-5
-10
-5 -4 -3 -2 -1 0 1 2 3 4 5 6 7 8 9 10 (min)
C
Fluorescence (z)
2
0
-2
-4
-6
-8
-10
-12
***
2 4 6 8 10 (min)
D
HbT
HbO
HbR
z-score
10
5
0
-5
-5 -4 -3 -2 -1 0 1 2 3 4 5 6 7 8 9 10 (min)
E
Corrected GCaMP
Measured GCaMP
Fluorescence (z)
5
0
-5
-5 -4 -3 -2 -1 0 1 2 3 4 5 6 7 8 9 10 (min)
F
Fluorescence (z)
8
6
4
2
0
-2
-4
-6
*
2 4 6 8 10 (min)

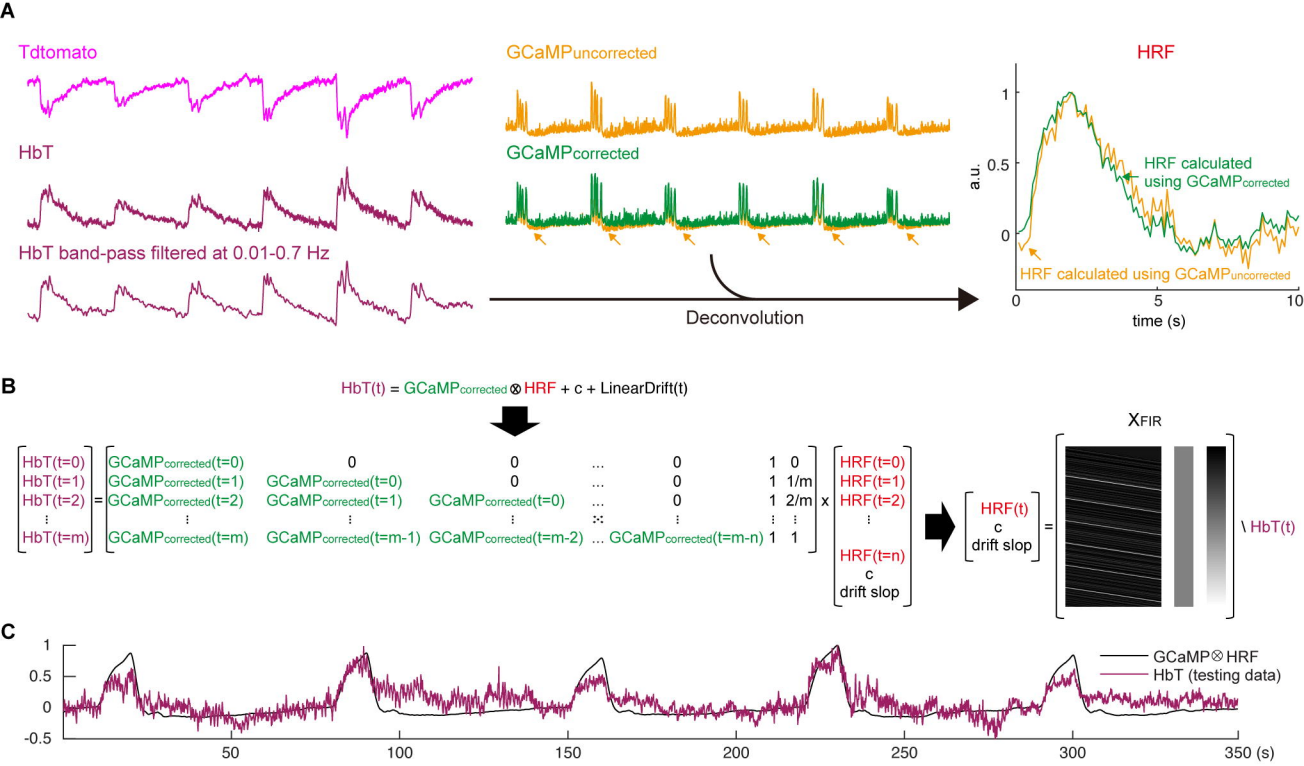
A
Tdtomato
HbT
HbT band-pass filtered at 0.01-0.7 Hz
GCaMPuncorrected
GCaMPcorrected
Deconvolution
HRF
HRF calculated using GCaMPcorrected
HRF calculated using GCaMPuncorrected
a.u.
time (s)
B
HbT(t) = GCaMPcorrected ⊗ HRF + c + LinearDrift(t)
XFIR
\ HbT(t)
HRF(t)
c
drift slop
C
GCaMP⊗HRF
HbT (testing data)
(s)

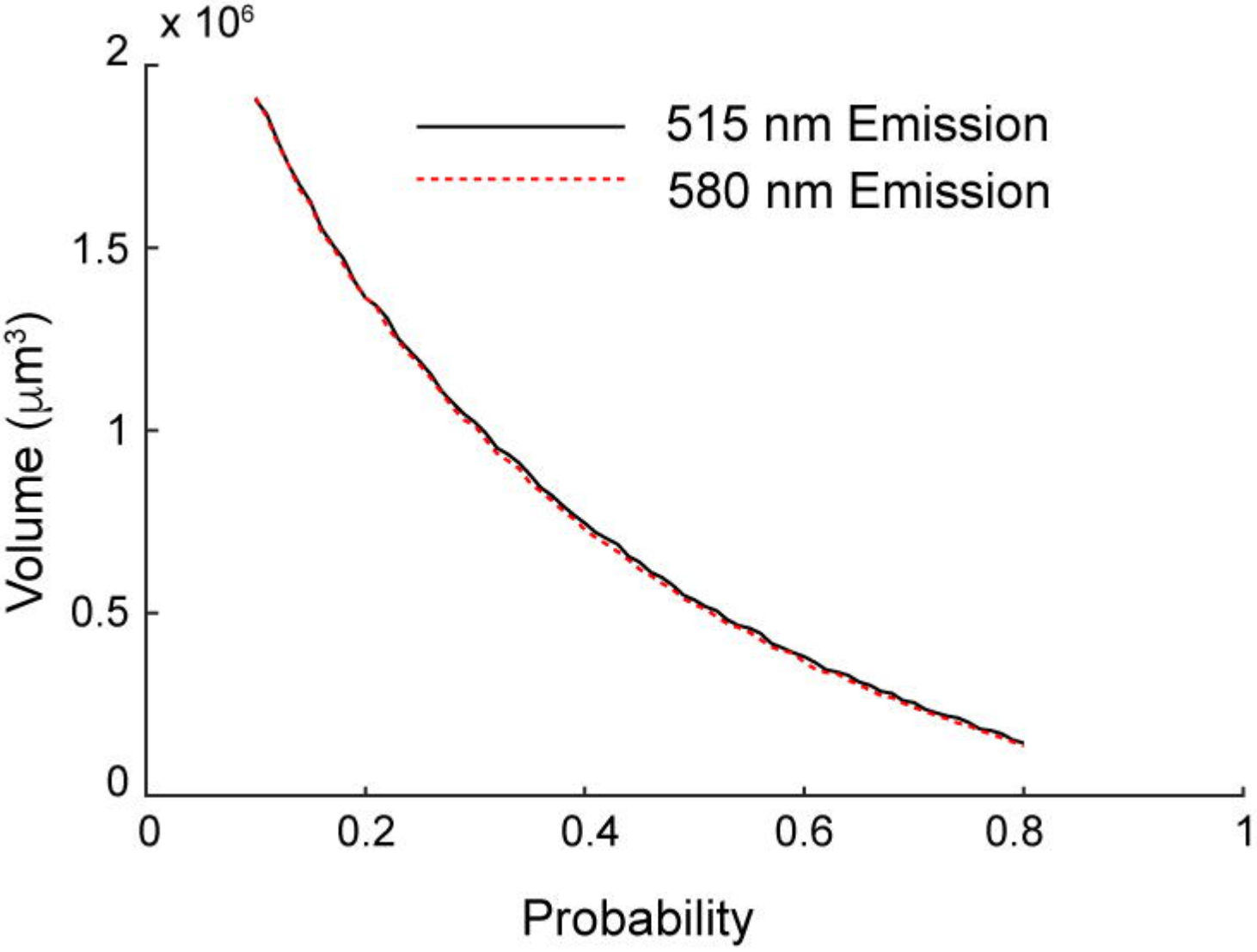
x 10^6
2
1.5
1
0.5
0
Volume (μm^3)
515 nm Emission
580 nm Emission
0
0.2
0.4
0.6
0.8
1
Probability

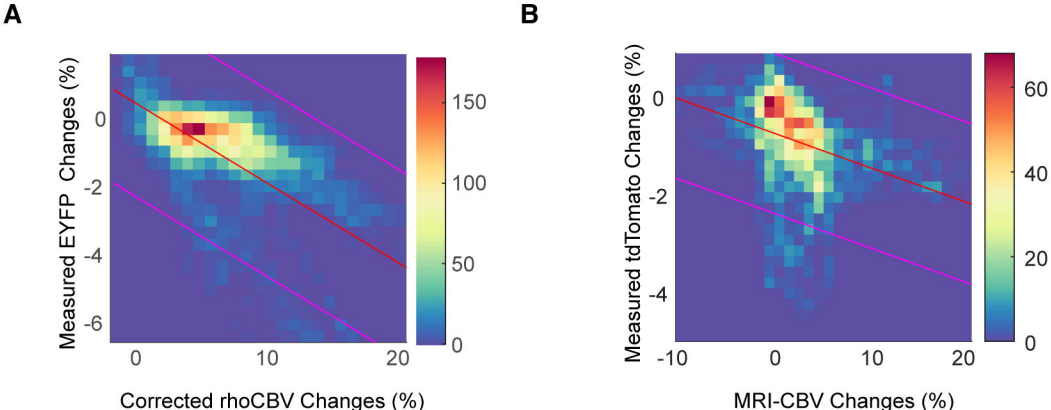
A
Measured EYFP Changes (%)
0
-2
-4
-6
0
10
20
Corrected rhoCBV Changes (%)
150
100
50
0
B
Measured tdTomato Changes (%)
0
-2
-4
-10
0
10
20
MRI-CBV Changes (%)
60
40
20
0

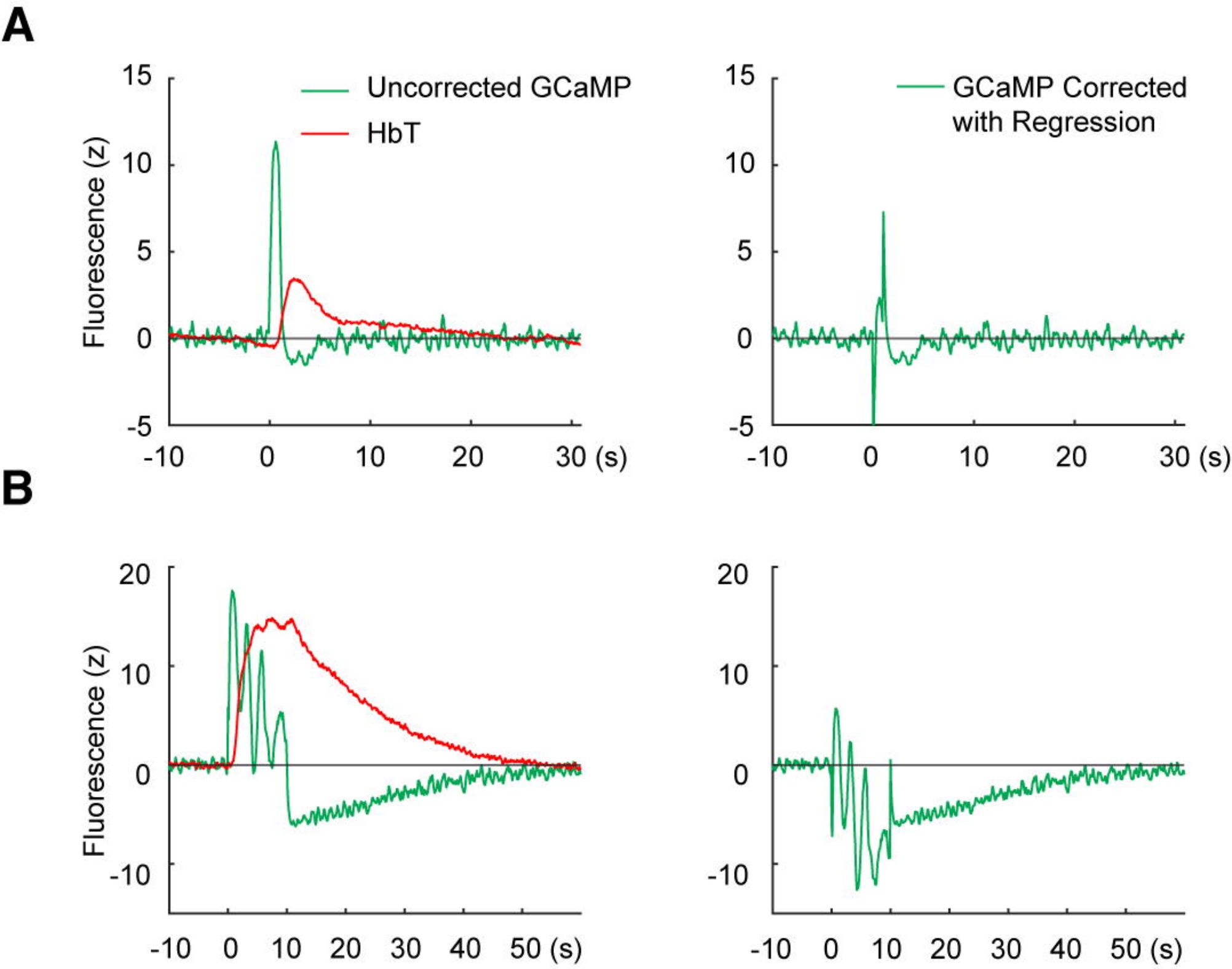
A
B
Uncorrected GCaMP
HbT
GCaMP Corrected
with Regression
Fluorescence (z)
15
10
5
0
-5
-10
20
-10
0
10
20
30
40
50 (s)

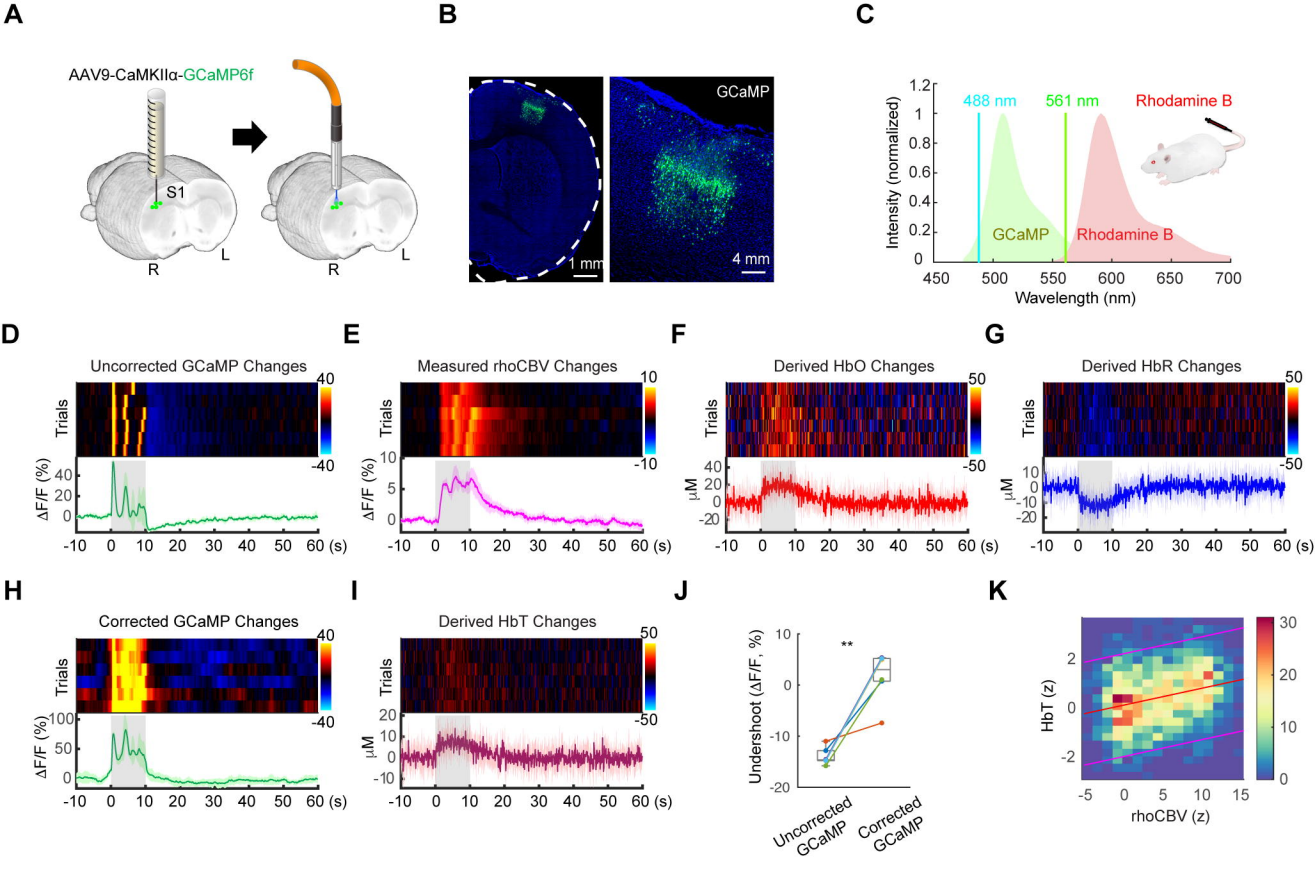
A
AAV9-CaMKIIα-GCaMP6f
S1
R
L
R
L
B
GCaMP
1 mm
4 mm
C
488 nm
561 nm
Rhodamine B
Intensity (normalized)
GCaMP
Rhodamine B
Wavelength (nm)
D
Uncorrected GCaMP Changes
Trials
ΔF/F (%)
E
Measured rhoCBV Changes
F
Derived HbO Changes
μM
G
Derived HbR Changes
H
Corrected GCaMP Changes
I
Derived HbT Changes
J
Undershoot (ΔF/F, %)
**
Uncorrected GCaMP
Corrected GCaMP
K
HbT (z)
rhoCBV (z)
(s)